STUDY OF VARYING BOUNDARY LAYER HEIGHT
ON TURRET FLOW STRUCTURES

THESIS

Renato Jelic,

AFIT/GAE/ENY/11-J01

DEPARTMENT OF THE AIR FORCE
AIR UNIVERSITY

AIR FORCE INSTITUTE OF TECHNOLOGY

Wright-Patterson Air Force Base, Ohio

AFIT/GAE/ENY/11-J01

Study of Varying Boundary Layer Height on Turret Flow Structures

THESIS

Presented to the Faculty

Department of Aeronautics and Astronautics

Graduate School of Engineering and Management

Air Force Institute of Technology

Air University

Air Education and Training Command

In Partial Fulfillment of the Requirements for the

Degree of Master of Science in Aeronautical Engineering

Renato Jelic, B.A.S.

June 2011

AFIT/GAE/ENY/11-J01

STUDY OF VARYING BOUNDARY LAYER HEIGHT ON TURRET FLOW STRUCTURES

Renato Jelic, B.A.S.

Approved:

_____   _____
Dr. R. Greendyke, PhD (Chairman)   date

_____   _____
Maj A. J. Lofthouse, PhD (Member)   date

_____   _____
Dr. S. Sherer, PhD (Member)   date

AFIT/GAE/ENY/11-J01

Abstract

The Air Force Institute of Technology and the Air Force Research Laboratory are investigating flows over turrets which are commonly encountered in directed energy weapons integrated on air vehicles. In this work, the computational study was performed using the NASA developed time-marching finite volume code OVERFLOW 2.2 to analyze the effect of boundary layer height on symmetrical and non-symmetrical turret geometries. The effects of aerodynamics reduce the beam quality by adding density fluctuations in the path of the beam, referred to as aero-optical jitter, and vibrations on the body through pressure fluctuations, referred to as aero-mechanical jitter. The analysis of the flow features, pressure fluctuations, density fluctuations, forces and moments was computed on two flat-window turret geometries to predict the impact on the beam quality at low subsonic and transonic speeds. The two geometries evaluated consisted of a twenty inch high turret geometry, referred to as the exposed turret, and a 50% submerged turret geometry, with a height of ten inches. The first flight condition was computed with Mach number of 0.45, Reynolds number of 157,697 per inch (1.892×10^6 per foot), and an altitude of 18,000 feet. The second flight condition was at Mach number of 0.85, Reynolds number of 238,376 per inch (2.86×10^6 per foot), and an altitude of 25,000 feet. The parametric study led to 24 cases for comparison of various boundary layer heights between the submerged and exposed turret geometries. The study of flow features indicated that an increase in boundary layer height delays the separation and leads to a reduction in the aero-mechanical and aero-optical jitter. For the study of aero-mechanical jitter the pressure fluctuations on the surface of the turret and the flat plate were analyzed to show that an increase in boundary layer reduces the pressure fluctuations in the wake of the geometry. Additionally, the forces and moments about the geometry were evaluated, which showed that the submerged turret geometry has a higher induced fluctuation

in the forces and moments than the hemispherical geometry. For the study of aero-optical jitter induced on the laser beam, density fluctuations along the centerline of the aperture were examined to show the effects of the boundary layer heights both quantitatively and qualitatively.

Acknowledgements

First and foremost I would like to thank my friends and family who have been supportive of me, without them I would have been unable to complete my research. I would also like to thank my advisor Dr. Greendyke who has taught me how to take what I have learned in the classroom and apply it to my work in this thesis. Next, I would like to thank Dr. Sherer for his guidance and patient mentoring throughout this project. Dr. Sherer taught me how to analyze problems and how to apply myself to solve them. Last, but certainly not least, I would like to thank the folks at AFRL who have been very patient and answered countless of my questions concerning the work in this thesis.

Renato Jelic

Table of Contents

List of Figures

x

Study of Varying Boundary Layer Height on Turret Flow Structures

I. Introduction

"Defense at the Speed of Light" became the Department of Defense (DOD) motto decades ago when the first laser was introduced. High-energy lasers have been in development for the past fifty years in order to provide real enhancement to military capabilities from tactical to strategic operations, yet there are no fully operational laser weapon systems in the inventory of the Department of Defense to date [2]. Currently, there are numerous programs investigating the laser capability for the purpose of Directed Energy Weapons (DEW). One of several airborne laser programs that has been extensively researched in the past was the Airborne Laser (ABL). The research of this program started during the 1970s and became more extensive during the 1980s. The laser turret was mounted on the front of a modified 747 and used a Chemical Oxygen Iodide Laser (COIL). The design of the turret geometry used for the first airborne laser turret was derived from land-based observatories for telescopes. The turret on an airborne platform is a bluff-body protrusion that consists of a hemispherical cap supported by a matching cylindrical base. This design provides convenient housing for pointing and tracking laser beams from airborne platforms [3].

The turret geometry creates complex aerodynamics that impact the optics by distorting a planar laser beam, even at low subsonic speeds [4]. Some of the predominant aerodynamic flow structures formed are: a horseshoe vortex, large separation region formed over the turret dome, and two inward rotating vortices in the wake of the turret. Consequently, these aerodynamic effects cause a reduction in the laser beam's quality. The unsteadiness of the fluid in the path of the laser beam leads to variations of density. The unsteady pressure forces on the surface of the turret create vibrations on the turret geometry [5]. When the first airborne laser projects

1

were introduced during the 1970s and 1980s, the experiments used COIL lasers and had a wavelength of approximately $10\mu m$. The impact of the aerodynamic flow on a laser with high wavelength is minimal, hence during the time of the COIL the research dealing with aerodynamics was neglected. Towards the late 1980s and early 1990s, advances in the technology led to a more powerful laser with wavelengths Near-Infrared (IR) of approximately 1μm. The distance a laser travels through a medium is described by the Optical Path Length (OPL); by having a medium with variations in index of refraction the laser is bent and the OPL changes significantly. The distance between direct line and the distance travelled by the distorted laser beam through the medium is referred to as Optical Path Difference (OPD). The OPD measures the interference and diffraction of the light as it propagates through the medium. So, while optical distortions are fairly small at low subsonic speeds ($\text{OPD}_{rms} \approx 0.1\mu$m), relative phase distortions, $2\pi\text{OPD}_{rms}/\lambda$, imposed on much shorter wavelength lasers, are increased by about an order of magnitude. As a result, decreasing the wavelength to Near-Infrared (IR) the unsteady optical distortions caused by a separated flow behind a turret are large enough to significantly reduce the far-field intensity [1]. During the late 1980s it was clear that as technology evolves and the lasers become more powerful with shorter wavelengths, the impact of aerodynamics on the laser beam will have a more dominant effect.

In order to reduce the aerodynamic effects caused by separated shear layers formed over the dome of the turret, various geometries [6] and flow controls [3, 7, 8] have been studied experimentally and computationally over the past two decades. The experiments conducted focused on low subsonic speeds with a Mach number range from 0.2 to 0.5, below the critical Mach number of a hemisphere. In recent years, the interest has shifted from low subsonic speeds to integrating the laser weapon on a transonic platform. Since the research of the past several decades has been mainly focused on the lower Mach numbers, no recent experiments have been conducted to investigate the aerodynamic effects on the geometry at near sonic speeds. The research reported in this thesis investigates the impact of aerodynamics on a flat window turret

with one foot diameter for two flight conditions. The first flight condition is referred to as "low-slow" which is at Mach number of 0.45, Reynolds number of 157,697, and an altitude of 15,000 feet. The second flight condition is referred to as the "high-fast" at Mach number of 0.85, Reynolds number of 238,376, and altitude of 25,000 feet. Note, both Reynolds numbers are computed with respect to a reference length in inches.

In order to investigate symmetrical vs. non-symmetrical flows over the turret geometry, simulations will be conducted with the flat window aperature facing into two directions. First orientation of the aperture will be facing forward at an azimuthal angle of 0 degrees and an elevation angle of 57 degrees. The second orientation is facing sideways of the incoming flow at an azimuthal angle of 45 degrees and an elevation angle of 57 degrees. In addition to varying the angle of the aperture, aerodynamics are evaluated with a submerged turret. For this study a hemispherical turret on a flat plate is submerged ten inches into the flat plate. The tactical platform envisioned for this project is most likely to have a length greater than 100 feet and the laser weapon will be placed on the bottom of the fuselage. Since the location has not been specified, depending on the position of the laser weapon, different boundary layer heights will be encountered; potentially changing the flow physics. For the non-submerged geometry, two boundary layer heights are evaluated: 5 and 10 inches (25% and 50%). For the submerged case, four boundary layer heights are evaluated: 2.5, 5, 7.5, and 10 inches (25%, 50%, 75%, and 100%). Because boundary layer heights of this magnitude are not easily obtained in wind tunnel experiments, this thesis will investigate the aerodynamics using a three-dimensional Computational Fluid Dynamics (CFD) flow solver called OVERFLOW 2.

II. Background

2.1 Background of the Airborne Laser

The application of directed energy has evolved tremendously over the past four decades and has been implemented into some useful military weapon systems. The development of the laser began when Albert Einstein laid the foundation for producing a stimulated emission of light in 1917. The use of lasers for military application was advanced in 1967 by Edward Teller, an expert in thermonuclear energy who once envisioned a fleet of aircraft with high-powered lasers as their weapon to defend against enemy aircraft or ground-to-air missiles.

The capability of striking a target at the speed of light from a far distance would produce a superior defense system. The mechanism for target destruction of continuous wave laser weapon systems is based on the absorption of the thermal energy by the target. Once the target starts to absorb thermal energy, some destructive effects start to occur, which can be anything from structural failure to explosions. The idea of having laser weapons has been envisioned for many decades, if not centuries, which has been the driving force behind the creation of the airborne laser systems.

The first lasers developed during the 1960s were ruby (solid state) lasers that had an output limit due to their heat capacity. By further investigating the laser performance, laboratory experiments determined that through chemical reactions and gas diffusion, certain high energy atoms could be produced that led to higher energy lasers. Shortly following the invention of the ruby laser, it was proposed by Basov and Oraevskii in 1962 that rapid cooling could produce population inversions in molecular systems which was successfully accomplished by expansion of a hot gas through a supersonic nozzle. Hence, in 1964 the carbon dioxide (CO_2) laser was developed emitting a wavelength of $10.6\mu m$, which lies in the near-infrared (IR) region of the spectrum.

Using the gas dynamic CO_2 laser, the United States Air Force (USAF) performed the first Airborne Laser Laboratory (ALL) project. A half-megawatt class laser was integrated into a modified Boeing 707 which was capable of delivering lethal

energy via beam control to a selected target. The project was successfully completed where USAF targeted towed diagnostic targets, engaged and defeated AIM-9B air-to-air missiles, and shot down sea-skimming target drones before the ALL project was retired in 1983 [9]. Even though the ALL project was a success, the laser capability was not mature enough to be implemented as a fielding weapon system. The problem with the gas dynamic CO_2 laser was the long wavelength ($10.6\mu m$) the laser produced in combination with limited optical component dimensions that led to weak and inaccurate laser propagations over a distance greater than 10 km. Just as importantly, the system was not developed to be operated or maintained on a war fighter system [2].

During the same time period, a parallel project was conducted in 1970 that researched an electrically driven Hydrogen Fluoride/Deuterium Fluoride (HF/DF) chemical laser by the Aerospace Corporation. The project name of the HF/DF program was named Baseline Demonstration Laser (BDL), which marked the first one hundred-kilowatt-class chemical laser. In the HF/DF system, the fluoride atoms are produced in a combustion chamber and are accelerated by going through supersonic nozzles into the laser cavity. The producing laser wavelength of the optical resonator is $2.7\mu m$.

The BDL program laid the foundation for the multi-hundred kilowatt class laser named Navy ARPA Chemical Laser (NACL). In combination with the Navy pointer tracker beam control and director system, the program successfully shot down TOW missiles in flight in 1978, and laid the foundation for the first Mid-IR Advanced Chemical Laser (MIRACL). In 1980, this became the world's first megawatt-class laser which shot down supersonic missiles and other targets [2]. Even though the above stated projects were able to produce more powerful lasers and the research was headed in the right direction, the problem of developing a laser with sufficiently short wavelength was not fulfilled. A shorter wavelength is needed to reduce the time it takes to transfer energy between the aircraft and the target. The invention of the Chemical Oxygen Iodine Laser (COIL) developed during the 1970s at the Air Force Weapons Laboratory finally led to a breakthrough from an optics perspective because

it produced a laser with a wavelength of 1.35 μm that has a smaller focus spot, higher intensity, greater range, and good atmospheric propagation. The use of a shorter wavelength laser was the right direction for the airborn laser to be headed. Currently, the COIL system has been integrated into a modified Boeing 747 aircraft that has several COIL laser modules on board in order to produce the megawatts of power necessary.

Overall, the technology of the laser is moving forward in the right direction and many innovations have been made in order to support an airborne laser system that is effective and proficient against enemy aircraft and ground-to-air missiles. However, a functional laser will have to successfully overcome the following areas: target hardness, atmospheric distortions, and system performance characteristics. Shorter wavelengths and higher beam qualities are required in order to precisely manage laser beam quality and propagation characteristics to strike a target at long range.

2.2   Aero-Optics Theory

In order to obtain a better understanding of the theories and concepts discussed in this thesis, some of the fundamentals of physics behind aero-optics are explained in this section. For the purpose of the research conducted in this thesis, a colliminated laser will be used for all simulated cases. A colliminated laser has rays that are nearly parallel and spread slowly as it propagates through space. Ideally, the collimated laser would not disperse with distance and project to infinity [10]. But when a colliminated laser propagates through a turbulent compressible flow, the waves become aberrated and the image becomes blurred, which defocuses the laser. The aberration exists as the local speed of light, u, is a function of the index-of-refraction, n, u/c = 1/n, where c is the speed of light in a vacuum [11]. The index-of-refraction is dependent upon the density, ρ of the gas via Gladstone-Dale relation [12] see Eqn. 2.1, where ρ' is the density fluctuation and K_{GD} is the Gladstone-Dale constant (in dimensions of $1/\rho$).

$$(n - 1) = n' = K_{GD}\rho' \tag{2.1}$$

6

The Gladstone-Dale constant depends on the properties of the gas and the frequency or wavelength of the light used. For a wavelength between 0.3562 and 0.9125 μm, the K_{GD} of air is between 0.2330 and 0.2239 (cm^3/g) [13].

Aberrations in the collimated laser caused by density fluctuations present in the atmospheric propagation [14] or in an aero-optics problem which has a relatively thin region of turbulent flow comprised of compressible shear layers, wakes and turbulent boundary layers around an airborne platform [5] can yield to a noticeably different laser than initially projected. The quality of the laser can be measured in various ways; however, the most common optical term to quantify the laser is the time-averaged Strehl ratio, S_t. The Strehl ratio is the simplest way to quantify the effect of wave front aberrations of the laser quality, by comparison of the peak diffraction intensities of an aberrated, $\bar{I}$ vs. perfect wave front, I_o.

$$S_T(t) = \frac{I(t)}{I_o} \tag{2.2}$$

However, when the length of the propagation is fairly short, physicist use Optical Path Length, OPL(x,y,t), to measure wave front aberrations. The optical length in a homogenous medium is the density (ρ) of the medium and the refractive index (n) of that medium, as shown in Eqn. 2.3.

$$OPL = n\rho \tag{2.3}$$

In a turbulent boundary layer, the medium is not homogenous and is comprised of compressible shear layers which have different densities and indices of refraction. The OPL is calculated as

$$OPL(x, y, t) = \int_{x_1}^{x_2} n'(x, y, z, t)\,\mathrm{d}z = K_{GD} \int_{x_1}^{x_2} \rho'(x, y, z, t)\,\mathrm{d}z \tag{2.4}$$

To compute the OPL integration is taken along the propagation axis, z, and the distribution is given by the normal planes, x and y. Another useful parameter in studying aberrations is the Optical Path Difference, OPD(x,y,t), which is a spatially-averaged mean subtracted from OPL(x,y,t), shown in Eq. 2.5.

$$OPD(x, y, t) = OPL(x, y, t) - \langle OPL(x, y, t) \rangle \tag{2.5}$$

Note the square brackets represent the spatially-averaged mean in the (x-y) plane.

Another formulation to compute the time-averaged Strehl ratio comes from the large-aperture approximation, which calculates the Strehl ratio for a given phase variance as

$$\bar{SR} = exp\left(-\sigma_\phi^2\right) \tag{2.6}$$

in which the phase variance is the normalized OPD variance as,

$$\sigma_\phi^2 \equiv \left(\frac{2\pi OPD_{r.m.s.}}{\lambda}\right)^2 \tag{2.7}$$

in which λ is the wavelength of the laser.

2.3 Aero-Optics Background

Next, the focus will turn to the background of aero-optics and how the field has evolved over the past few decades. This section will provide a better understanding of the fundamentals by examining some of the major contributions since the invention of the laser.

The performance of airborne laser systems can be drastically reduced by the effects of aerodynamic perturbations around the aircraft due to variations in the index of refraction. Phase distortion, amplitude wave variation, blurring of the image, and optical beam deflection, also referred to as beam-jitter, are all effects of index of refraction. In order to place lasers on airborne platforms the underlying physics of how the laser behaves when impacted by aerodynamic effects needs to be examined. The first work done in the field of aero-optics was by Liepmann [15] in 1952 studying the index-of-refraction through a compressible boundary layer in wind tunnels at high Reynolds numbers. Using Schlieren photographs, he came to the conclusion that the unsteady large turbulent structures in the outer boundary are the most dominant factors to the index-of-refraction in a turbulent medium. This was one of the first classifications of the density fluctuations present in turbulent boundary layers.

Liepmann recognized that there would be some issues in placing lasers on an airborne platform and that the performance would be limited. The first in depth analysis of the physics having an impact on the laser performance was published in 1956 by Stine and Winovich [16]. The research focused on the laser propagation through varying boundary layer heights and Mach numbers in the subsonic and supersonic regime on a flat plate. The conclusion drawn is that the aberration formed in the collimated laser relates to the integral scale and the intensity of the density fluctuations present in the turbulent flow. Stine and Winovich validated the theories formulated by Liepmann and brought together all of the work conducted up to that date in the field of aero-optics.

Until the 1960s, there had been no theoretical formulation to describe the physics that are taking place when propagating a laser in a medium with density fluctuations. In 1969 one of the most significant theoretical breakthroughs in aero-optics was accomplished by Sutton [17]. He formulated an equation to compute aberrations via phase variance using turbulent statistic measurements in the medium as shown in Eq. 2.8,

$$\sigma_\phi^2 = 2K_{GD}^2 k^2 \int_0^L \rho_{r.m.s.}(y)^2 \Lambda_\rho(y)\, dy \tag{2.8}$$

where σ_ϕ is the phase variance, $\rho_{r.m.s.}$ is the root mean square of the density, and $\Lambda_\rho(y)$ is the density correlation length in the wall normal direction. Some further analysis shows that the phase variance, σ_ϕ is related to the Optical Path Difference variance through the wave number, $k = 2\pi/\lambda$, by $\sigma_\phi = OPD_{r.m.s.}k$, where λ is the laser wavelength [18].

During the 1970s, the interest in having an airborne laser increased and the research in the field of aero-optics became more popular. In 1979 one of the most extensive researchs in the field of aero-optics was conducted by Rose, who studied the optical aberrations formed by turbulent boundary layers. The experiment was conducted in a wind tunnel using hotwires to capture the density fluctuations, ρ', and the associated wall normal length, Λ_ρ (y), while assuming that the pressure fluctuations are negligible. By using this set up, the root mean square of the Optical Path Difference, $OPD_{r.m.s.}$ was computed using the formulation made by Sutton a few years prior, see Eqn. 2.8. Rose formulated that the root mean square of the Optical Path Difference, $OPD_{r.m.s.}$ is proportional to the dynamic pressure, q, and the boundary layer thickness, δ, as shown in Eqn. 2.9.

$$OPD_{r.m.s.} \sim q\delta \tag{2.9}$$

Until the late 1980s, most of the research done in the field of aero-optics focused on the time averaged, spatial, near field optical phase variance, σ_ϕ^2, either through the direct optical measurements or via fluid-mechanical measurements. The instruments used to conduct the research were interferometers which gave time-averaged assessments of the optical variance but did not provide any information of the temporal frequencies [18].

During the 1980s, it was assumed that aero-optics was a fairly well understood field. In 1985 Sutton announced that the field of aero-optics was only missing turbulence statistics of a few flow conditions. Otherwise, it was a very mature and well understood field. Just when the scientists thought they had a firm grasp on the subject of aero-optics, things took a turn in the 1990s, when newer lasers were developed and proposed for the use on airborne platforms. The lasers of the 1990s had wavelengths shorter by an order of magnitude than the ones decades prior. The old system had a Carbon Dioxide (CO_2) laser with wavelengths of 10.6 μm and on average the aberration caused by a boundary layer $OPD_{r.m.s.} \sim 0.1\mu m$. The Strehl ratio was less than 1% which has minimal effects in comparison to shorter wavelength lasers. The correlation between wavelength (λ) and Optical Phase Distortion (OPD) was formulated by Smith [19] in 1966, shown in Eqn. 2.10.

$$\bar{S}_t = exp\left[-\left(\frac{2\pi OPD_{r.m.s.}}{\lambda}\right)^2\right] \tag{2.10}$$

The formulation between OPD and wavelength scales the exponent as $(1/\lambda)^2$. Eqn. 2.10 shows that modern day lasers with wavelength on the near IR spectrum ($\sim 0.1\mu m$) have a reduced Strehl ratio of approximately 30 % or even more in some cases. This issue forced scientists to reinvestigate the boundary layer problem [18] and the impact of aerodynamics on the airborne lasers.

Modern technology now allows more advanced data to be extracted from experiments than in the past. Not only are scientists capable of obtaining the $OPD_{r.m.s.}$, but also the spatial and temporal frequencies of the aberration that have not been

obtainable in the past. Modern instrumentation is capable of computing the instantaneous Strehl ratio which is of interest in communication applications. Once the instantaneous Strehl ratio is extracted, it can be averaged over time which is of interest in the field of aero-optics. Experiments are capable of providing more information to describe the physics occuring, this leads to more answered questions and fewer variables left unsolved.

With the newly developed lasers of reduced wavelength, the focus has been to understand the physics behind the aero-optics and to find ways to reduce the effects of aerodynamics causing jitter and density fluctuations. Over the past twenty years, numerous geometries and flow controls have been studied in order to reduce the wave front aberrations.

2.4 Aerodynamics in Aero-Optics

The main focus of this thesis is to understand the interaction between aerodynamics and optics over various turret geometries and boundary layer heights. A better understanding of the flow physics will provide an insight of the causes of the density fluctuations and pressure variations on the surface that cause jitter. Depending on the velocity of the inflow, the flow characteristics can be categorized. Numerous wind tunnel experiments and computational simulations have been conducted in order to better understand the aerodynamics present depending on the inflow velocity. The two common geometries used to study the aerodynamics are the conformal window turret, also referred to as the baseline turret, and the flat window turret; both are shown in Fig 2.1.

Both geometries are defined by the diameter of the hemisphere, D, and the height of the cylinder, H. In the case of $H = 0$, the geometry is just a hemisphere on a flat plate. For the flat window geometry, the size of the aperture is denoted by the diameter A_p, the orientation is described by the azimuthal angle , β, and the elevation angle, γ. For simplification purposes, it is beneficial to introduce a third angle between the outward beam vector and the freestream vector as the window

((a)) Side View   ((b)) Isometric View

((c)) Side View   ((d)) Isometric View
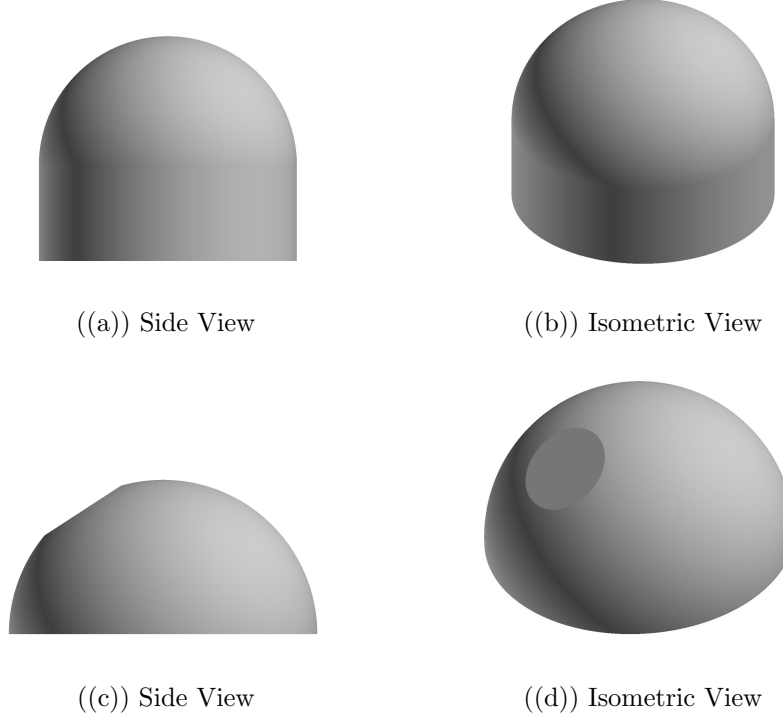
Figure 2.1:   Top - Baseline Turret, Bottom - Flat Window Turret

angle, α. The geometric relationship between the angle of the window and the other two angles is

$$cos(\alpha) = cos(\beta)cos(\gamma) \tag{2.11}$$

Hence, when the azimuthal angle is set to zero, the window and elevation angle are coincident, $\alpha = \gamma$ and if $\beta = \pi$, then $\alpha = \pi - \gamma$ [20]. The angles are used to describe the orientation of the aperture for all cases throughout the thesis, see Fig. 2.2.

Aerodynamics over hemispheres has been studied in numerous applications ranging from aero-optics to buildings such as mosques. An accurate flow prediction over such a simple geometry is still a demanding task in fluid dynamics. The difficulties of the problem arise in modeling several complex flow features including separation, reattachment, three-dimensional curved free shear layers, effects of surface roughness, and interaction with the oncoming turbulent boundary layer [21].
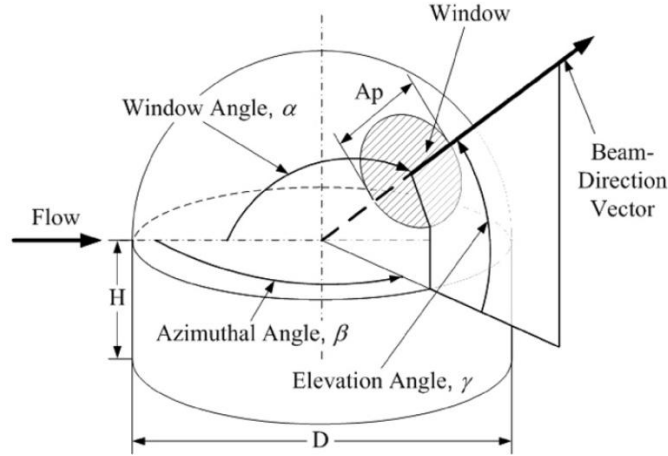
Figure 2.2:   Schematic of definitions and angles for the turret geometry [1]

The geometry of a turret is a combination of a hemisphere and a cylinder and the fluid physics formed around the geometry are a combination between the two. At lower subsonic speeds the shape of the turret creates a complex flow, as shown in Fig. 2.3. Upstream of the turret, a horseshoe vortex is formed which wraps around the sides of the turret and propagates downstream into the wake of the flow. The flow over the surface of the turret geometry is attached on the front half of the dome, while the adverse pressure gradients in the aft half cause the flow to separate. The separation region in the aft part of the turret interacts with the horseshoe vortex in the wake of the turret which form a complex flow topology in the wake of the turret. The complex region consists of reversed flow in the back of the turret and secondary vortices on the sides of the turret [1].

Over the years many experiments have investigated the flow around bluff geometries and many concepts have been formulated of what causes each of the flow features. Two dominant factors that influence the flow physics are the boundary layer height and the turbulent intensity within the boundary layer. Toy [22] performed a set of wind tunnel experiments on a hemisphere with two different boundary layer heights and different turbulent intensity and velocity profiles. The conclusion drawn from this experiment was that an increase of turbulent intensity in the boundary

14
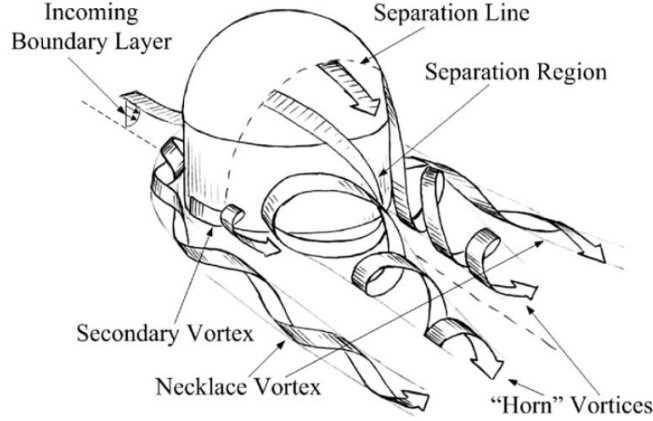
Figure 2.3:   Schematic of subsonic flow around turret [1].

layer moved the separation and reattachments points downstream of the hemisphere. The same author investigated three boundary layer heights imposed on a hemisphere. Their focus was on the near wake separation and reattachment region of the flow. The conclusion drawn from this experiment was that the maximum pressure gradient occurs in the case of the thin boundary layer [23]. Manhart [21] performed a numerical study using large eddy simulation (LES) on a hemisphere with a turbulent boundary layer imposed. The investigation identified two mechanisms that form the separation over the hemisphere. The first mechanism is the separation and roll-up of the curved shear layer over the dome of the hemisphere which are symmetric arc-type vortices. The second mechanism is the alternating separation from the side regions which are connected with large-scale Von Karman vortices. To this date, literature review shows that there are no detailed combined experiment and numerical studies of turbulent flow over a hemisphere for varying boundary layer flows [24].

The next area of interest is the complex flow formed over the dome of the turret which is a separation and reattachment region in the near wake. It has been shown that the incoming boundary layer has a dominant effect on the separation and recirculation region in the wake of a hemisphere. Savory and Toy [23,25,26] demonstrated during the 1980s that the shape of the boundary layer and the momentum at the

15

obstacle affects the pressure coefficient and the back-flow velocity in the recirculation region in the near wake of the hemisphere. The length of the recirculation region and the shape of the pressure coefficient is mainly driven by the intensity of the turbulence in the boundary layer [26].

The discussions mentioned above of the flow topology and optical distortions is valid only for the fully subsonic regime, where the flow around the turret is subsonic everywhere. Because the flow accelerates over the turret, the local Mach number will reach sonic value at some critical incoming Mach number. For some inflow Mach number that is above the critical Mach number the flow will become locally supersonic. The computed critical Mach number for the turret geometry is Mach 0.55. If the inflow is equal to the critical Mach number, a local supersonic region will form on top of the turret with an ending normal shock. The local supersonic region causes a boundary-layer-shock interaction which causes the flow to prematurely separate on top of the turret and form a larger separation region than observed in the fully subsonic case, as shown in Fig. 2.4. When further increasing the Mach number, the supersonic region on the turret will grow in size and extend to the base of the turret, and at Mach number 0.77 the wake becomes fully supersonic. This analysis has not taken into account the turbulent wake behind the turret, which would make the flow even more complex due to unsteady pockets of supersonic flows and weak shocks forming in the wake, as shown in Figure 2.4. The shock formed on the dome of the turret oscillates rapidly due to the shock-boundary-layer interaction [27], which adds more unsteadiness to an already complex flow on the turret and further aberrations to the optics.

The formation of an oblique shock in the wake of the turret leads to premature separation, large wake for transonic regime, and increased density variations which causes higher optical aberrations on the outgoing laser beam at transonic speeds. Experimentally this was shown on a hemisphere [28] which concluded that aberrations up to Mach number of 0.5 follow the 'ρM^2'-law which is a correlation between aberration to the density and Mach number squared. At Mach number of 0.64 the
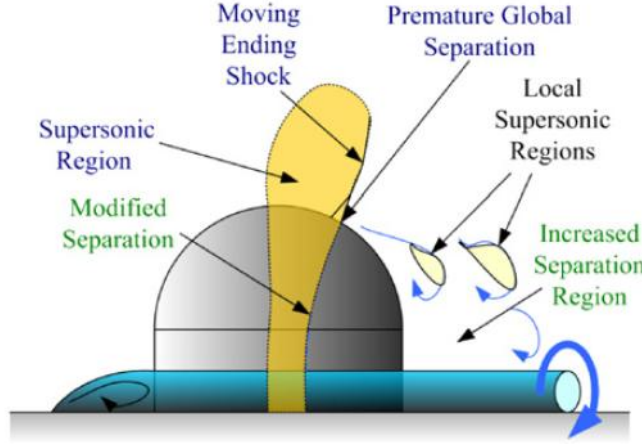
Figure 2.4:   Schematic of the flow around the turret at transonic $(1 > M > M_{cr})$ speed [1].

aberrations were found to be almost twice that of the subsonic law prediction 'ρM^2'. The higher aberrations formed are due to the unsteady normal shock formed on top of the hemisphere, which forces premature separation and a large turbulent wake downstream [1].

2.5   CFD Solver OVERFLOW 2.2

In computational fluid dynamics (CFD), for turbulent flow, the range of length scales and complexity of the phenomena make the computations nearly impossible. In this case, the approach is to create a model to calculate the properties of interest. The main issue with resolving turbulent flows comes from the large range of length and time scales that need to be resolved. To achieve a higher accuracy, smaller scales need to be resolves which leads to a higher computational cost. For the direct numerical simulation (DNS) the entire range of turbulent scales is resolved, the result is a solution of high accuracy but at a very high computational expense. In large eddy simulations (LES), the smallest scales are removed through a filtering operation and their effect is modeled through subgrid scale models. As a result, the the most important turbulent scales are resolved and the computational expense is significantly

reduced in comparison to DNS solutions. In the case of Reynolds-averaged Navier-Stokes (RANS) turbulence modelling, the ensemble version of the governing equations is solved. In this case the modelling introduces new apparent stresses referred to as Reynolds stresses. Different variations of the RANS model can provide closure to the second order of tensor presented in the Reynolds stresses. A modified RANS model in which the model switches to a subgrid scale formulation in regions fine enough for LES calculations is the detached eddy simulation (DES). For this turbulence model the regions near the wall where the turbulent length scales are less than the maximum grid dimensions are solved by the RANS modelling. For the turbulent length scales that exceed the grid dimension, the solution is solved through the LES model.

Over the years, direct numerical simulation (DNS) and large eddy simulation (LES) have developed into vital tools for the investigation of the fundamental turbulent fluid flows. Because DNS and LES are not always feasible at realistic flight Reynolds numbers due to their computational expense, detached eddy simulation (DES) and delayed detached eddy simulation (DDES) are often employed to obtain computational results. This work will examine the DDES capability of NASA's widely-used structured overset code OVERFLOW 2. The OVERFLOW 2 code is a production code that has been widely used in the computational fluid dynamics (CFD) industry.

In order for the overset grids to properly communicate among each other, OVERFLOW requires the grid connectivity to be set up using a pre-processor; for the research conducted in this thesis the grid connectivity is set up using PEGASUS5. OVERFLOW 2 was selected because higher order codes currently available in the research field are not applicable to full aircraft type geometries because of the difficulties in the grid generation and solver numerical stability. The benefit of speedy grid generation for complex models, the implementation of many schemes and turbulence models, the robustness, and the validation of OVERFLOW 2 make it an appealing choice for CFD.

2.5.1 OVERFLOW 2.2 Capabilities. OVERFLOW 2 has many inviscid flux algorithms, implicit solvers, turbulence models, boundary conditions, and other functions implemented within the code [29]. The following is a list of the main implementations:

- Numerical Methods - Inviscid Flux Algorithms:

    1. 2nd, 4th, 6th order central differencing with smooting

    2. Yee symmetric TVD scheme

    3. Liou ASUM+ upwind

    4. Roe upwind

    5. HLLC upwind

    6. 5th order WENO and WENOM upwind

- Numerical Methods - Implicit Solvers:

    1. ARC3D Beam-Warming block tridiagonal scheme

    2. F3D Steger-Warming 2-factor scheme

    3. ARC3D diagonalized Beam-Warming scalar pentadiagonal scheme

    4. LU-SGS algorithm

    5. D3ADI algorithm with Huang subiterations

    6. ARC3D Beam-Warming with Steger-Warming flux split jacobians

    7. SSOR algorithm with subiterations

- Global Turbulence Models:

    1. Baldwin-Lomax algebraic model

    2. Baldwin-Barth model (1-eqn.)

    3. Spalart-Allmaras model (1-eqn.)*

4. k-ω model with DDADI or SSOR implicit solver (2-eqn.)*

5. SST model with DDADI or SSOR implicit solver(2-eqn.)*

*Note, S-A, k-ω, and SST models can be used in conjunction with Delayed Eddy Simulation (DES) or Detached Delayed Eddy Simulation (DDES)

- Additional Capabilities:

   1. 1st and 2nd order time advance for Newton/dual subiterations

   2. SARC or approximate rotational/curvature correction term

   3. Sarkar compressibility correction

   4. Abdol-Hamid temperature correction

   5. 1st, 2nd, or 3rd order differencing for turbulence convection terms

2.6   Overset Grid Implementation

Overset grid generation was developed in order to model complex geometries and moving bodies. The main function of overset grid is that neighboring structured blocks overlap and are not set point-to-point in order to interpolate data, as seen in most structured grid solvers. The points in the overlap region between two neighboring blocks are referred to as fringe points. Using a NASA developed code called PEGASUS5 as a pre-processor for an overset flow solver, 2nd order interpolation can be established between grids and each point is declared as either field, boundary, receiver, hole, or donor point. The use of overset grids provides the user with the capability of controlling the resolution of each grid independently, where clustering points at near body grids in order to resolve the finer flow structures and coarsen the grid in other areas can provide a significant reduction in computational expense. The weakness of overset grid generation lies in the use interpolating data between overlapping blocks. Significant differences in grid spacing between blocks can create to interpolation error which can be reduced in most cases by using grid quality assess-

ment tools. The main areas of concern are smooth hole region boundaries, sufficient amount of overlap between blocks, and resolution in the overlapping regions [30].

III. Methodology

Using OVERFLOW 2.2, a hemispherical and a submerged flat window turret geometry were setup in order to analyze the jitter encountered by the geometry and density fluctuations by the laser. The geometries were examined at two flight conditions, the first is referred to as "low-slow" at Mach number of 0.45, Reynolds number of 157,697, and an altitude of 15,000 feet; this is the subsonic case. The second case is referred to as the "high-fast" at Mach number of 0.85, Reynolds number of 238,376, and altitude of 25,000 feet; this is the transonic case due to local supersonic "pockets" formed in the wake of the turret. With a turret diameter of 20 inches, note both Reynolds numbers are computed with respect to a reference length of inches. In order to investigate symmetrical vs. non-symmetrical flows over the turret geometry, simulations will be conducted with the flat window aperture facing in two directions. The symmetrical geometry is with the aperture facing forward at an azimuthal angle of 0 degrees and an elevation of 57 degrees. The non-symmetrical geometry has the aperture facing at an azimuthal angle of 45 degrees and an elevation angle of 57 degrees.

The boundary layer height is different depending on the location on the fuselage of the aircraft on which it is integrated. The possibility of the turret being integrated on a long aircraft will create a different boundary layer height depending on the placement of the turret. To study the varying boundary layer heights on the fully exposed turret geometry (twenty inch height), a 25% and 50% of the total height boundary layers were imposed and for the submerged geometries (ten inch height) four boundary layer heights of 25%, 50%, 75%, and 100% were imposed.

To date there is no experimental or computational data for the geometries studied. However, to accurately capture the flow physics over the flat-window turret two cases with similar flow physics were examined to determine which spatial schemes and turbulence models to select from OVERFLOW 2.2 to best capture the aerodynamics over the flat window turret. The cases selected for the investigation of spatial scheme and turbulence model were a theoretically infinite cylinder and conformal window tur-

ret; both cases have been studied computationally and experimentally which makes them a great selection for comparison.

In order to accurately create the computational domains of varying aperture direction and submergence levels, a grid generation script was created that allows for repeatable cases to be executed with same parameters but varying geometry inputs, which reduces the user error and keeps any discrepancies constant for all grid generations if any arose.

The length of flat plate required to generate a boundary layer height of ten inches can be several feet long which creates a significant computational penalty for high boundary layers. To minimize the computational expense, a two-dimensional flat plate simulation was performed from which a plane of data was extracted and extruded into the spanwise direction. The extruded variables would then be imposed on the three-dimensional simulations. The two-dimensional flat plate was computed for each of the flight conditions and all of the boundary layers heights of interest were extracted from those simulations. The ability to impose a boundary layer reduced the computational expense and the number of computational domains that would arise if each had a different length flat plate upstream of the turret.

3.1 Validation

In order to accurately model the flow of the "low-slow" and "high-fast" flight conditions, two additional cases of similar geometries and flow physics were performed to determine which spatial scheme, physical time step, and turbulence model to select. The first case to be examined is the transitional flow over a theoretically spanwise infinite cylinder at $Re_D = 3,900$ and $M_\infty = 0.1$. Due to the low Reynolds number, no turbulence model is used, making it an ideal case to evaluate various spatial schemes. This benchmark case has a complex flow in the wake of the cylinder because it transitions from laminar to turbulent flow. The location of the transition between laminar to turbulent flow is a crucial to properly capture in order to obtain the proper quantitative values of pressure coefficients (c_p), fluctuating velocity components (u',v',w'),

and Reynolds stresses $(u'v')$. Over the past few decades this case was studied computationally using a wide variety of solvers [31–35]. Research conducted on this problem in the past showed that the difficulty arose due to the transitional nature of the flow at such low Reynolds number and the flow features emerging were a three-dimensional wake, unstable shear layers, and shedding vortices. Experiments have revealed that ill-resolved shear layers undergo early transition and more fluctuations pass through the region immediately behind the cylinder, which suggests the cause of disagreement between experiment and large eddy simulations (LES) [35].

The computation was set up with four overlapping grids: body-fitted grid around the surface of the cylinder $(199 \times 61 \times 45)$, near-field polar grid $(201 \times 71 \times 45)$, fine wake grid downstream of the cylinder $(248 \times 101 \times 45)$, and a background grid $(91 \times 91 \times 45)$ as shown in Figure 3.1. The grid system employed in this problem is identical to the computational mesh used by the FDL3DI solver [32] with a total of 2.92 million grids points. The FDL3DI solver is an Air Force Research Lab (AFRL) created solver that is a hybrid between Reynolds averaged Navier-Stokes and implicit large eddy simulations (RANS/ILES) code with up to sixth-order compact spatial discretization in conjunction with an eighth-order low-pass spatial filter.

Periodic boundary conditions were imposed in the spanwise direction to simulate a theoretically infinite cylinder, while free-stream characteristic boundary conditions were applied on the remaining outer boundaries. The computation was advanced from a uniform-flow state for 20,000 time steps to remove any start-up transients, and statistics of mean flow and fluctuating quantities were collected for an additional 60,000 time steps. The non-dimensional time step (Δt) used for this computation was 0.002. For validation purposes the results were compared to experimental data compiled by Kravchenko and Moin [31] and computational data obtained from Sherer and Visbal [32]. To investigate the spatial schemes, the following three schemes were selected: the third-order HLLC inviscid flux scheme, fifth-order WENO scheme, and fifth-order WENOM scheme. The spatial schemes were used in conjunction with an implicit unfactored Successive Symmetric Over Relaxation (SSOR) algorithm.
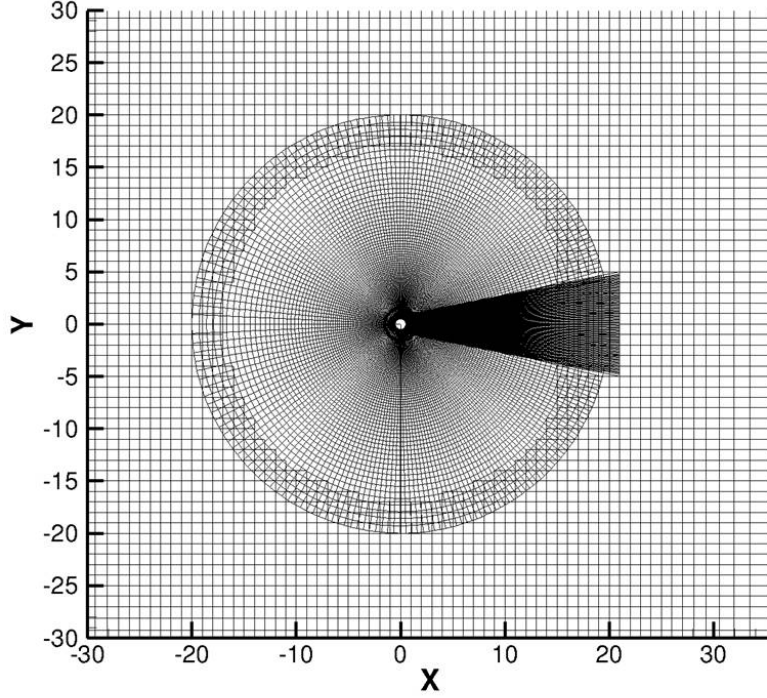
Figure 3.1:   Overset grid to capture flow over cylinder, includes body-fitted, near-field polar, fine wake, and farfield grids.

Quantitative comparison between the results of OVERFLOW, the experimental data, and FDL3DI was performed by computing the spanwise-averaged mean pressure coefficient (c_p), spanwise-averaged mean streamwise velocity along the wake centerline of the cylinder, and Reynolds stresses as illustrated in Fig. 3.2 - 3.4.

The results of the WENOM scheme quantitatively agree with the FDL3DI solution the best; the WENO scheme deviates in the magnitude at certain locations but still captures the trends of the experiment and computation of FDL3DI. Overall, mean pressure coefficient (c_p), spanwise-averaged mean streamwise velocity component along the wake centerline of the cylinder, and Reynolds stresses show that the higher-order results of the WENO and WENOM quantitatively agree with the FDL3DI computations and the experiment. As the Reynolds stress profiles are measured further downstream of the cylinder, the accuracy of the computations to the experimental values deviates for both OVERFLOW and FDL3DI. The reason is due to insufficient domain size in the spanwise direction, which is constraining the de-
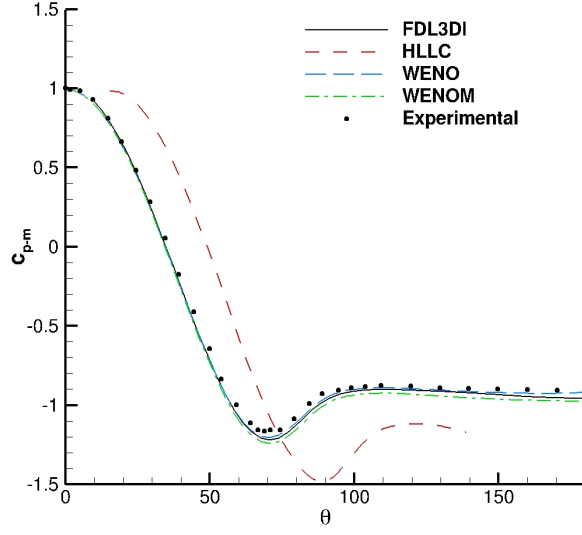
Figure 3.2:   Mean pressure coefficient (c_p) as a function of angle (θ) on the surface of the cylinder.
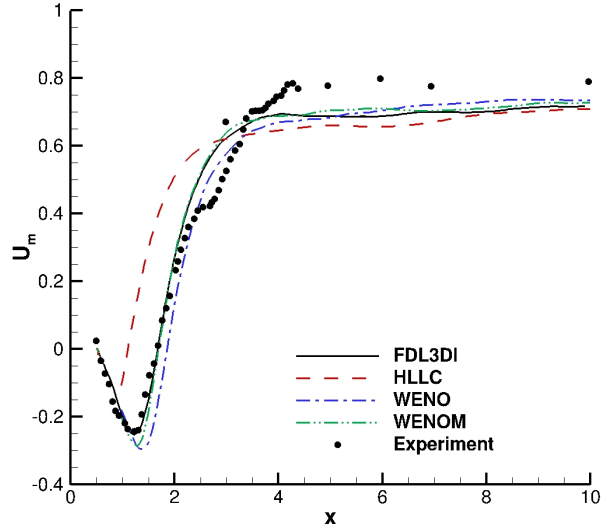
Figure 3.3:   Spanwise-averaged mean streamwise velocity component along the wake centerline of the cylinder.

velopment of the larger spanwise structures that are formed downstream [31]. The results reveal that the WENOM scheme performs the best and was selected for the
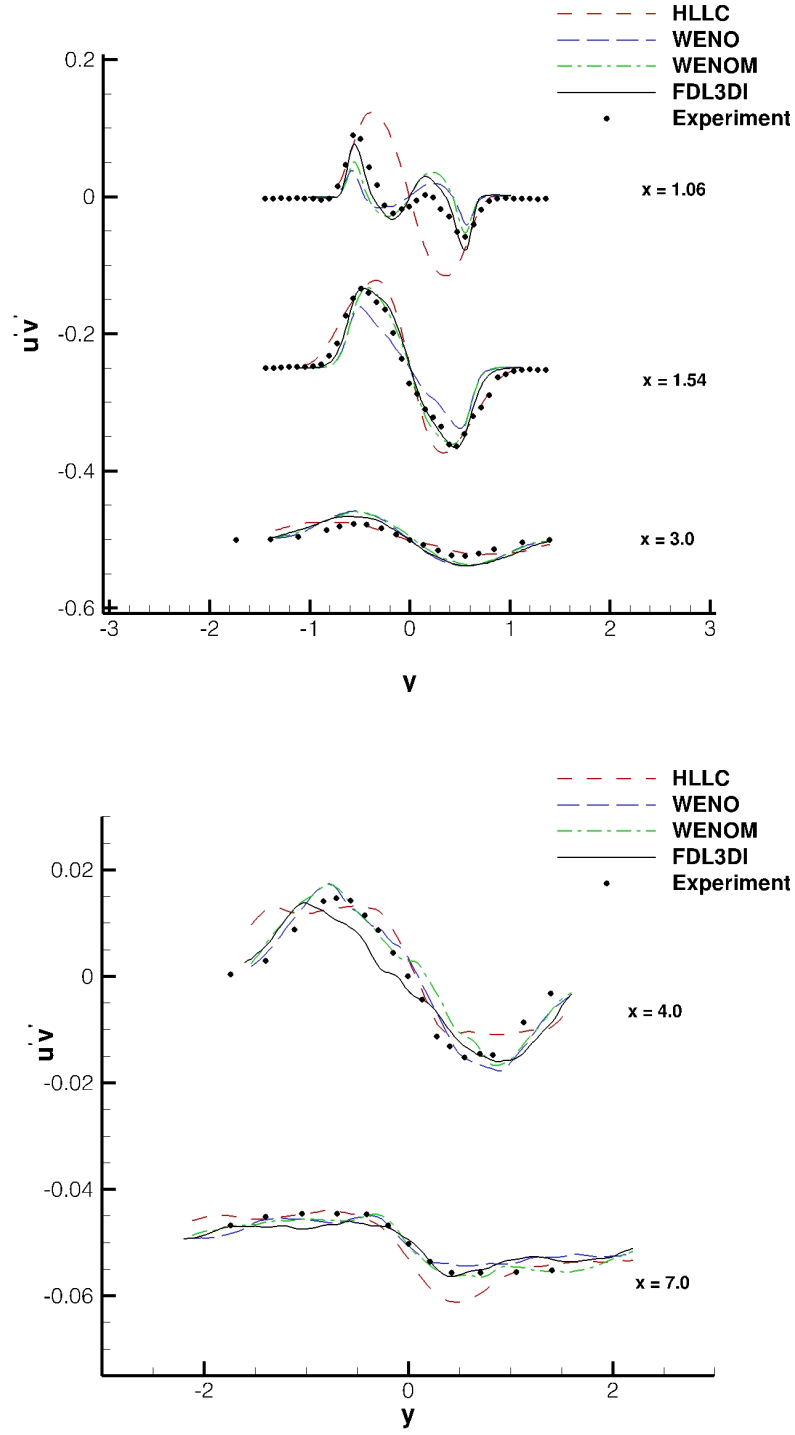
Figure 3.4: Spanwise-averaged Reynolds stress profiles in wake of cylinder, $Re_D = 3900$.

computations of the flat-window turret; for further analysis see Ref. [36]. Note, Fig. 3.2 - 3.4 have been offset for the purpose of better visualization.

The second validation case selected is a one-foot conformal window turret at flow conditions of $M_\infty = 0.4$ and $Re_D = 2.4 \times 10^6$. Recent work was done to study this case using FDL3DI with a fourth-order compact spatial discretization in conjunction with a sixth-order low-pass spatial filter [37]. The experimental results were collected at the Air Force Academy by Gordyev [20] in a subsonic wind tunnel with a test section of $3 \times 3 \times 8$ ft. The turret was mounted asymmetrically and the results were obtained at a Mach number of 0.4. The experiment was computationally recreated for the wind tunnel as shown in Figure 3.5. All wind tunnel lengths have been non-dimensionalized by the turret diameter when constructing computational domains, which extends over $-3.75 \le x \le 10.0$ in the streamwise direction, $0 \le y \le 3.0$ in the normal direction, and $-1.7083 \le z \le 1.29167$ in the spanwise direction. A total of nine computational blocks have been used to recreate the wind tunnel including the turret. An O-C grid topology was employed around the turret itself which consists of $201 \times 301 \times 275$ points in the body normal, tangential, and circumferential directions, respectively. Since the turret was meshed via a revolution, a cap grid had to be implemented along the revolving line in order to avoid a singularity. The wall spacing of the turret in the radial direction was set to $\Delta r = 1.0 \times 10^{-5}$. A total of five blocks with square cross-sectional domains were implemented to model the center of the wind tunnel, an additional two blocks were employed to model the sides of the tunnel, creating a total of nine computational blocks. The grid spacing applied was uniform from the inflow boundary until about $x = 4.0$, which is 48 inches downstream of the turret, past that point the grid was stretched downstream. The same wall normal spacing was applied for all grids to reduce interpolation error. The final grid system was composed of approximately 24 million cells and is identical to the computational domain used by the FDL3DI simulation [37]. In order to properly initialize the flow-field, an empty wind tunnel was simulated and a steady state solution was obtained. From the steady state solution, the experimentally measured boundary layer was imposed. The inflow

plane for the wind tunnel/turret grid system was then initialized from an extracted plane of the empty wind tunnel. The computation was advanced for a total of 30,000 time steps in order to remove any start-up transients, and statistics were collected for an additional 15,000 time steps.

Boundary Conditions

Inviscid	■ (red)
Viscous	■ (blue)
Prescribed Inflow	■ (magenta)
Outflow	■ (green)

Computational Dimensions

Streamwise	=	$-3.75 \leq x \leq 10.0$
Normal	=	$0.00 \leq y \leq 3.00$
Spanwise	=	$-1.71 \leq z \leq 1.29$

Note: Non-dimensionalized by turret diameter
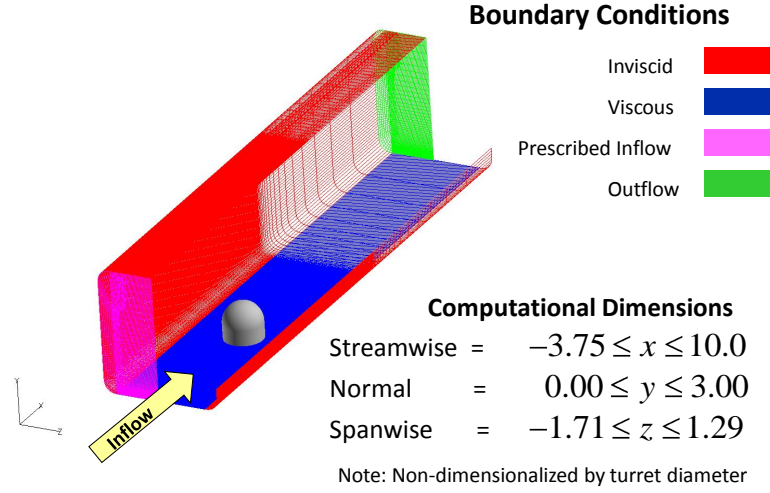
Figure 3.5:   Nine block computational mesh of the windtunnel with the asymmetrically placed turret.

The spatial scheme selected for this case is the fifth-order WENO scheme, with an implicit SSOR algorithm. For the time accurate cases, the time step was set to a constant time-step with five second-order Newton sub-iterations to reduce the time marching error and boundary condition instabilities. To determine which turbulence model most accurately captures the flow physics, the following six cases were examined:

1. Spalart-Allmaras (S-A) with Detached Eddy Simulation (DES)

2. Spalart-Allmaras (S-A) with Delayed Detached Eddy Simulation (DDES)

3. Shear Stress Transport (SST) with Detached Eddy Simulation (DES) using Diagonally Dominant ADI (DDADI) method

4. Shear Stress Transport (SST) with Delayed Detached Eddy Simulation (DDES) using Diagonally Dominant ADI (DDADI) method

5. Shear Stress Transport (SST) with Detached Eddy Simulation (DES) using Successive Symmetric Over Relaxation (SSOR) algorithm.

6. Shear Stress Transport (SST) with Delayed Detached Eddy Simulation (DDES) using Successive Symmetric Over Relaxation (SSOR) algorithm.

Quantitative comparison between the results of OVERFLOW, experimental data, and FDL3DI was performed by computing the pressure coefficients (c_p) along the centerline of the dome of the turret as shown in Fig. 3.6. The conformal window geometry causes a separation region in the wake of the dome at 87 degrees as seen by experiment. The OVERFLOW results using the SST turbulence models capture the location of the separation but deviate in magnitude by a couple of percent. A qualitative comparison is performed to validate that reverse flow is captured in the same region by FDL3DI as shown in Figure 3.7.

From Fig. 3.6, the results show that the Delayed Detached Eddy (DDES) simulation is preferred over the Detached Eddy Simulation limiter. Menter and Kuntz [38] initially formulated this correction for the SST turbulence model which computes the distance from the wall and disables the LES mode if it indicates that the point is inside the boundary layer. Once the distance computed to the wall has indicated that there is separation occurring it will turn on the Large Eddy Simulation (LES) mode. The switch between RANS to LES takes place more abruptly following separation than in the DES model. In other words, the grey area between RANS and LES is smaller; the model does not in itself create LES content, but it accelerates its growth following natural instabilities, closer to the region where modeled Reynolds stresses are still at full strength.
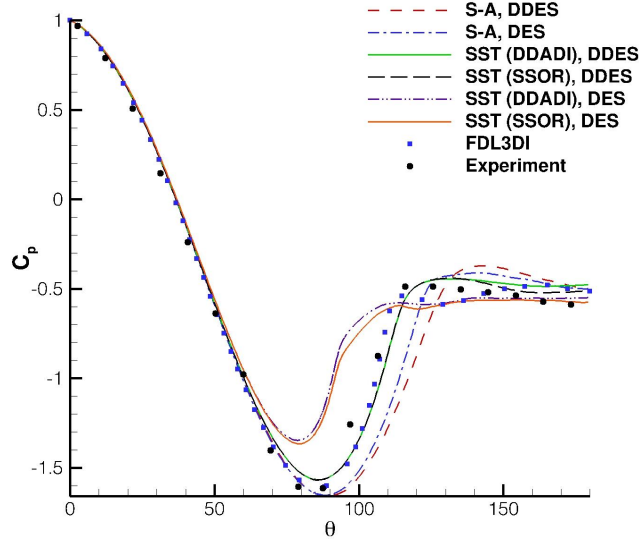
Figure 3.6:   OVERFLOW 2.2 simulations with six different turbulence models for comparison to experimental and computational data.

((a)) OVERFLOW (SST Turbulence Model (SSOR, DDES))

((b)) FDL3DI
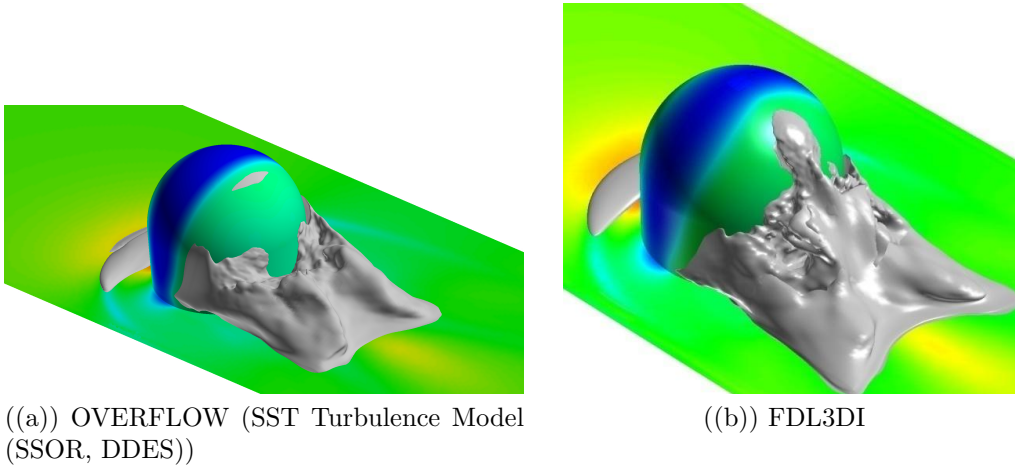
Figure 3.7:   Iso-Surfaces of the reversed flow for qualitative comparison

The simulations performed in the validation section were conducted in order to simulate flows over bluff bodies and compare the results between experimental data and two computational codes, FDL3DI and OVERFLOW. The different spatial schemes and turbulence models were tested determine which solver would most accurately model the flat window turret for the "low-slow" and "fast-high" flight conditions. For the infinite cylinder case, it was concluded that the OVERFLOW results

31

quantitatively agree with the experimental and computational data of the FDL3DI solution. The results show that the third-order scheme keeps the flow attached for too long causing a late transition to turbulence. The validation case confirms that the fifth-order solution significantly improves the accuracy compared to a third order spatial scheme. The wind tunnel validation was used to determine which turbulence model to select. The results show that the Shear Stress Transport (SST) turbulence model using the Delayed Detached Eddy Simulation (DDES) agrees both quantitatively and qualitatively the best with the experimental and computational data. The separation angle modeled via OVERFLOW is identical to that of the experiment at 87 degrees, but the magnitude is not accurately captured. Some computations were conducted using the Spalart-Allmaras (S-A) turbulence model for both the DES and DDES capability which keeps the flow attached further than shown in the experiment or the FDL3DI solution. The results modeled using the SST turbulence model in conjunction with the DES capability show that the flow separates and transitions to turbulence too soon, creating an inaccurate solution.

3.2 Grid Topology

Examining the impact of boundary layer heights on symmetric vs. non-symmetric flat-window turrets at two submergence levels creates a total of four geometries with varying azimuthal angle of the aperture and two submergence heights. For one of the topologies the aperture is facing in the forward direction into the incoming flow at an azimuthal angle of 0 degrees and an elevation of 57 degrees. The second direction is with the aperture facing sideways of the incoming flow at an azimuthal angle of 45 degrees and an elevation angle of 57 degrees. The two submergence levels examined will be a fully exposed turret with a radius of 20 inches and a 50% submerged geometry with hemisphere of ten inches above the flat plate. The resulting four geometries to be simulated are shown in Fig. 3.8.

The final grid topology was constructed using five computational blocks to model the flat plate and turret. The turret itself employed an O-C grid topology which con-

((a)) Exposed turret ($\alpha = 0$, $\beta = 10$)   ((b)) Exposed turret ($\alpha = 45$, $\beta = 10$)

((c)) Submerged turret ($\alpha = 0$, $\beta = 10$)   ((d)) Submerged turret ($\alpha = 45$, $\beta = 10$)
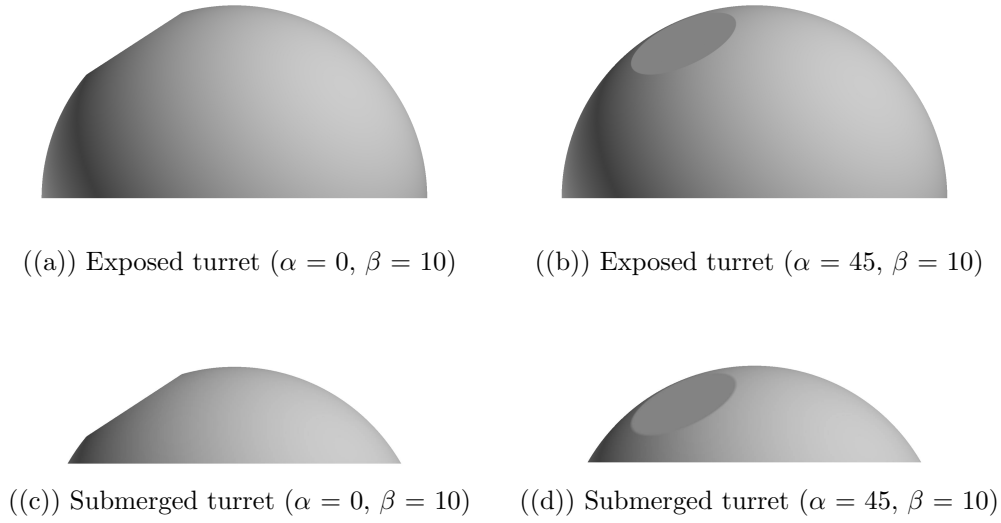
Figure 3.8:   Turret geometries examined at two flight conditions

sists of $201 \times 281 \times 281$ points in the body normal, tangential, and circumferential directions, respectively. To reduce the interpolation error between the turret and background grids, the script was setup to employ matching grid spacing for the background grid depending on the outer domain of the turret. The background grid was scripted in order to match the spacing of the outer boundary of the turret mesh to reduce the interpolation error. The background grid is uniform from the inflow plane until three turret diameters aft the turret before it starts to stretch at a 5% rate. Since the turret and aperture were meshed via a revolution, a cap grid had to be implemented to compensate for the singularity formed at the center of the O-grids. The volume of the two cap grids were splayed in order to match the grid stretching at the turret outer domain. The computed Y+ values of the "low-slow" and "high-fast" simulations for viscous wall spacing (compressible) are 1×10^{-4} in. and 7.64×10^{-5} in., respectively. In order to avoid the creation of additional grids, the Y+ value for the "high-fast" case was employed for all simulations.

The creation of the submerged geometry utilized the same topology as for the fully exposed turret geometry except that the flat plate was raised into the grid by ten inches. The definition of the turret surface was created via the scripting function

33

of $r \times cos(\theta)$ for the x-coordinate and $r \times sin(\theta)$ for the y-coordinate from 0 to $\pi/2$. The curve was then revolved for 360 degrees and aperture and cap grids were added to create the final computational domain. For the submerged case the limits of the x- and y-coordinates changed from 0 to $\pi/3$, the remainder of the process was conducted the same way for the fully exposed grids.

Since the examination of the flat-window turret is done via a parametric study, the test matrix compiled for the study of the flat-window turret consists of 24 cases, shown in Fig. 3.9. The variables are azimuthal angle (α), two flight conditions ("low-slow" and "high-fast"), two submergence levels with four boundary layer heights for the ten inch submerged grid and two boundary layer heights for the non-submerged case.

Case #	azimuthal	elevation	Mach No.	B. L. Height	Submergence	Grid No.
1	0	10	0.85	25%	0	Grid #1
2	0	10	0.85	50%	0	
3	45	10	0.85	25%	0	Grid #2
4	45	10	0.85	50%	0	
5	0	10	0.45	25%	0	Grid #1
6	0	10	0.45	50%	0	
7	45	10	0.45	25%	0	Grid #2
8	45	10	0.45	50%	0	
9	0	10	0.85	25%	50%	Grid #3
10	0	10	0.85	50%	50%	
11	0	10	0.85	75%	50%	
12	0	10	0.85	100%	50%	
13	45	10	0.85	25%	50%	Grid #4
14	45	10	0.85	50%	50%	
15	45	10	0.85	75%	50%	
16	45	10	0.85	100%	50%	
17	0	10	0.45	25%	50%	Grid #3
18	0	10	0.45	50%	50%	
19	0	10	0.45	75%	50%	
20	0	10	0.45	100%	50%	
21	45	10	0.45	25%	50%	Grid #4
22	45	10	0.45	50%	50%	
23	45	10	0.45	75%	50%	
24	45	10	0.45	100%	50%	

Figure 3.9:   Parametric study of the flat-window turret

3.3   Solver Setting

The two flight conditions modeled have different velocities and Reynolds numbers. Consequently the two-dimensional flat plate simulations were conducted for each case. An example of the imposing boundary layer is shown in Fig. 3.10.

<div align="center">

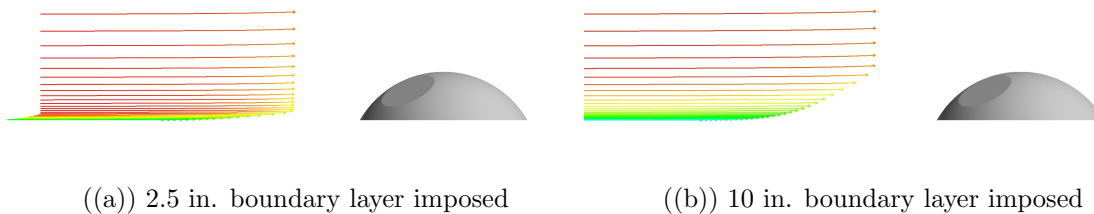((a)) 2.5 in. boundary layer imposed   ((b)) 10 in. boundary layer imposed

</div>

Figure 3.10:   Varying boundary layer heights imposed on the 50% submerged turret geometry

Once the plane to be imposed was obtained the next step was to select the solver setting. The fifth-order spatial WENOM scheme with the SSOR implicit algorithm was employed for all the computational blocks. The SSOR implicit algorithm is set up by default to perform ten sub-iterations on the relaxation parameters to help stabilize the solution. The turbulence model chosen for all of the simulations was the Shear Stress Transport (SST) turbulence model with an integrated SSOR implicit solver for the left hand-side. The Delayed Detached Eddy Simulation (DDES) was selected for all of the computational blocks around the turret with an approximate rotational/curvature correction (IRC) term. The DDES parameter was not applied to the background grid because it would introduce an adverse pressure gradient and transition the boundary layer to turbulent upstream of the turret. The time step was set to a constant with five second-order Newton sub-iterations to reduce the time marching error and boundary condition instabilities.

The specified boundary conditions are illustrated in Fig. 3.11, with a prescribed inflow plane which depends on the boundary layer height and flight conditions. The

<div align="center">

35

</div>

sides, top, and rear boundaries of the background grid were set to supersonic/subsonic inflow/outflow boundary conditions. The surfaces such as the flat plate and the turret were computed as viscous adiabatic walls.
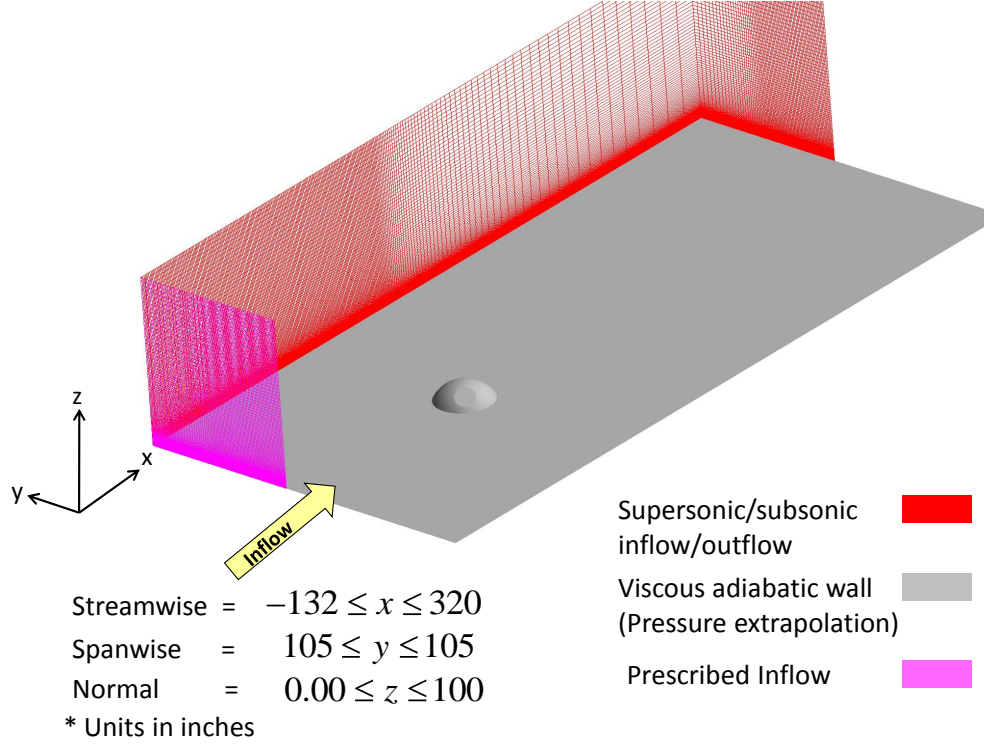
Figure 3.11:   Example of the computational setup including boundary conditions and domain size

3.4   Post-Processing

The procedure of examining boundary layer heights at two flight conditions for all 24 cases was the same in order to avoid any additional variables. The first step was to run the simulation up to 25,000 iterations, and the steady-state solutions were examined to provide an insight of the flow structures formed. By creating surface streamlines and iso-surfaces of the negative u-velocity, the flow structures reveal where the stagnation point occurs, horn vortices are formed, and lines of separation start to form in the aft part of the dome. This gives a fundamental understanding for the

basis of the flow structure creation and what to anticipate when the unsteady results are obtained.

There are two ways that the aerodynamics impact the laser. First, density fluctuations in the sight of the laser beam cause variations in index of refraction which aberrates the laser. To examine the density fluctuations in the area of laser propagations, a root mean square of the density fluctuation is computed in each cell of the solution using the OVERFLOW 'q.avg' function. The root mean square of the density fluctuation is then plotted vs. distance away from the aperture along the centerline of the laser as illustrated in Fig. 3.12. To further examine the density variations along the centerline of the laser, several points from the surface to approximately 24 inches normal to the aperture were selected for which the density values at each iteration were saved. Examining the density values at those locations vs. time can be used to compute the frequencies. The second form of aerodynamic induced aberrations on the laser comes from jitter which are vibrations of the turret due to pressure variations on the surface. To examine the pressure fluctuations on the aperture, two lines of the pressure root mean square along the horizontal and vertical centerlines were extracted, as shown in Fig. 3.12. By comparing the pressure fluctuations among all the cases it can be determined which flow parameters induce the most jitter. Additionally, several points along the turret surface, shown in Fig. 3.12 are selected to extract pressure in order to plot the frequencies.

The flow creates complex flows over various turret geometries at high-speed and low-speed flight conditions that exhibit significantly different flow features. To qualitatively examine the unsteadiness of the flow structures, solution files at 200 iteration increments were saved and used to create movies of the unsteady data. The visualization of pressure, temperature, density gradients, velocity magnitude, and iso-surfaces of vorticity magnitude were analyzed to examine the unsteadiness.
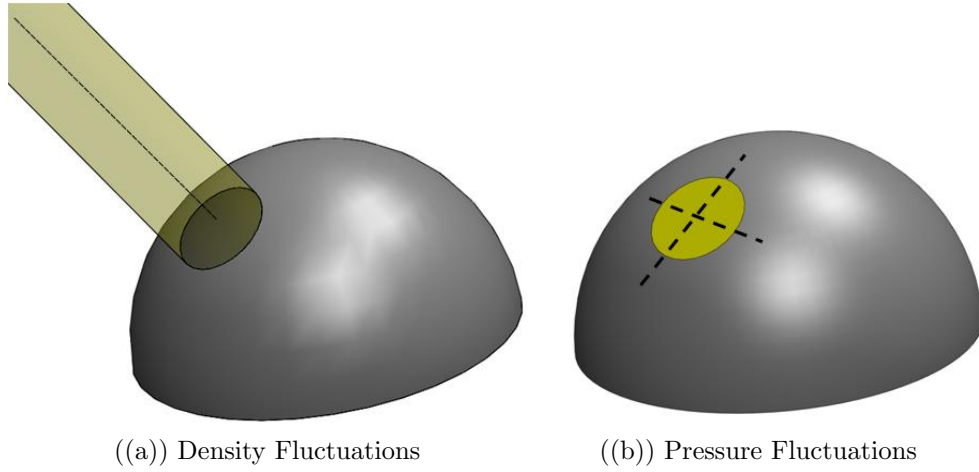
((a)) Density Fluctuations   ((b)) Pressure Fluctuations

Figure 3.12:   Reference lines used to plot density and pressure fluctuations

3.5   Grid Convergence

As a self-validation method of conducting a grid gonvergence was implemented to ensure that the computational results obtained converge for both flight conditions. The grids created for the convergence study were all scripted, the number of points for each grid can be modified with ease to create a coarse, medium, and fine mesh. Because the sizes of the computational volumes are driven by the grid spacing around the turret, the grid convergence study was dependent mainly to the number of points specified for the turret grid. For the coarse mesh, the turret grid employed $181 \times 241 \times 151$ points in the tangential, circumferential, and body normal directions, respectively. The medium size mesh consisted of a total 36 million cells in which the turret employed $281 \times 281 \times 201$ points in the tangential, circumferential, and body normal directions, respectively. The fine mesh had a total of 83 million cells with a grid spacing on the turret mesh of $381 \times 381 \times 301$ points in the tangential, circumferential, and body normal directions, respectively. To quantitatively determine that the grid had reached convergence, the pressure coefficients are plotted along the centerline of the turret to show that the separation point is accurately captured. Quantitatively, the solutions were compared to visualize the similarities between the flows and any differences that arise. The results show that the solution has converged in the front half of the

38

turret but continues to resolve and capture the separation region in the wake of the turret. Due to the significant increase in computational expense, the medium grid was chosen for the simulations presented in this thesis. The results of grid convergence are dicussed in-depth in Chapter 4.

IV. Results

This chapter presents the results of a hemispherical and a submerged flat window turret that was simulated using a time-marching finite volume code OVERFLOW 2.2, developed by NASA. All simulations were performed on the Raptor cluster at the AFRL DSRC Supercomputing Center using approximately 2.5 million computational hours. The solver settings selected for the study depended on the studies described in Chapter III. It was determined that the fifth-order WENOM spatial scheme in conjunction with the SSOR implicit algorithm would best capture the flow characteristics for the numerical simulations conducted. Using the conformal window computation as a basis to study various turbulence models, the Shear Stress Transport (SST) turbulence model with a Delayed Detached Eddy Simulation (DDES) was chosen for the geometries evaluated in this work.

The cases were all initialized independent of each other and computations were performed for 50,000 iterations to flush out any start up transients. At the 25,000 iteration mark, the solutions were examined to ensure that all proper parameters were selected and no files were corrupted. For the time dependant computations, a non-dimensional time step of 0.06 was selected. The evaluation of the time step was performed during the infinite cylinder simulations which was described in Chapter III.

Once the transitioning period was complete and the solution reached the 50,000 iteration mark, the input file was set up to collect time averaged and fluctuation data of the flow quantities to analyze the aero-optical and aero-mechanical jitter on the turret geometries. Additionally, from 50,000 to 100,000 iterations, several points on the geometry were selected to extract the conserved variables of all the flow quantities at each iteration in order to calculate the frequency of pressure and density at those points, see Section 4.5. At the end of the simulation (100,000 iterations) OVERFLOW was set to generate a 'q.avg' file (50,000 - 100,000 iterations) which creates an average of the unsteady flowfield solution file in addition to the velocity, pressure, and density fluctuations at each computational point. Using the capability

of the 'q.avg' file, the pressure fluctuations were studied along the aperture centerline to determine how the variation in boundary layer affects the mechanical jitter. To study the aero-optical jitter, the density fluctuation along the centerline normal to the aperture was examined at various boundary layer heights for all turret geometries, see Section 4.6. The "low-slow" and "high-fast" flight conditions imposed on the exposed and submerged turret geometries at varying boundary layer heights create complex flow features that were analyzed to provide an insight into how they relate to the aero-optical and aero-mechanical jitter. The unsteady flow features are qualitatively analyzed by saving a solution file in increments of 200 iterations (from 50,000 to 100,000 iterations). The solution files were then played as transient data in FieldView to display the magnitude of density gradients, Mach number, iso-surfaces of vorticity magnitude, and surface pressure. The quality of the solutions was analyzed through the study of residuals presented in Section 4.9 and grid convergence conducted by refining and coarsening the computational domain, see Section 4.8.

Due to the large number of cases to be analyzed by the parametric study, the solutions are presented in groups by type of geometry. For example, group 1 consists of cases 1 and 2 which have the same geometry and flight condition ("high-fast") but vary in boundary layer height imposed; a summary of all the cases divided up into groups is presented in Table 4.1.

4.1   Boundary Layer Validation

A total of six boundary layer heights were extracted for each flight condition and imposed on the computational domain in order to reduce the computational expense of having to grow a boundary layer over a flat plate upstream of the turret. Because the study is concerned mainly with how the boundary layer height affects optical and mechanical jitter, a section has been created to theoretically validate that proper boundary layers have been simulated. The boundary layer encountered in the simulation is a fully turbulent boundary layer with a zero pressure gradient and an increase in thickness to the power of $x^{4/5}$, whereas in laminar flow the boundary

Case #	azimuthal	elevation	Mach No.	B. L. Height	Submergence	Group No.
1	0	10	0.85	25%	0	Group 1
2	0	10	0.85	50%	0	
3	45	10	0.85	25%	0	Group 2
4	45	10	0.85	50%	0	
5	0	10	0.45	25%	0	Group 3
6	0	10	0.45	50%	0	
7	45	10	0.45	25%	0	Group 4
8	45	10	0.45	50%	0	
9	0	10	0.85	25%	50%	Group 5
10	0	10	0.85	50%	50%	
11	0	10	0.85	75%	50%	
12	0	10	0.85	100%	50%	
13	45	10	0.85	25%	50%	Group 6
14	45	10	0.85	50%	50%	
15	45	10	0.85	75%	50%	
16	45	10	0.85	100%	50%	
17	0	10	0.45	25%	50%	Group 7
18	0	10	0.45	50%	50%	
19	0	10	0.45	75%	50%	
20	0	10	0.45	100%	50%	
21	45	10	0.45	25%	50%	Group 8
22	45	10	0.45	50%	50%	
23	45	10	0.45	75%	50%	
24	45	10	0.45	100%	50%	

Figure 4.1:   List of simulations grouped together by type of geometry

layer thickness would increases $\delta \approx x^{1/2}$. The first analysis of the boundary layer was conducted through the law of the wall. For better visual comparison, the boundary layers are plotted on a logarithmic scale computing the inner law variables y^+ and u^+. The law of the wall can be broken down into several sections; the region of $y^+ \leq 5$ is where the turbulence is damped out and the boundary layer is dominated by viscous shear. The next region of $5 \leq y^+ \leq 30$, is called the sublayer and the velocity profile is neither linear nor logarithmic but provides a smooth merge between the viscous sublayer and log layer. For $35 \leq y^+ \leq 350$ the log layer is displays linear behavior. After the overlap layer, the outer law commences which can have some pressure gradients for pipe flows but none on a flat plate. The equations used to model the sub layer and log layer are shown in Equations 4.1 and 4.2, respectively [39].

$$u+ = \frac{1}{0.41} ln(y+) + 5.0 \qquad (4.1)$$

$$u+ = \frac{1}{0.40}ln(y+) + 5.4 \qquad (4.2)$$

The results of the law of the wall comparison between the theoretical values for the sublayer and loglayer vs. computational values obtained from OVERFLOW are presented in Figure 4.2(a) for the "high-fast" flight condition and in Figure 4.2(b) for the "low-slow" flight condition. The results quantitatively match the theoretical results postulated by White [39] for both the sublayer and the log layer.

((a)) "High-Fast" flight condition.   ((b)) "Low-Slow" flight condition.
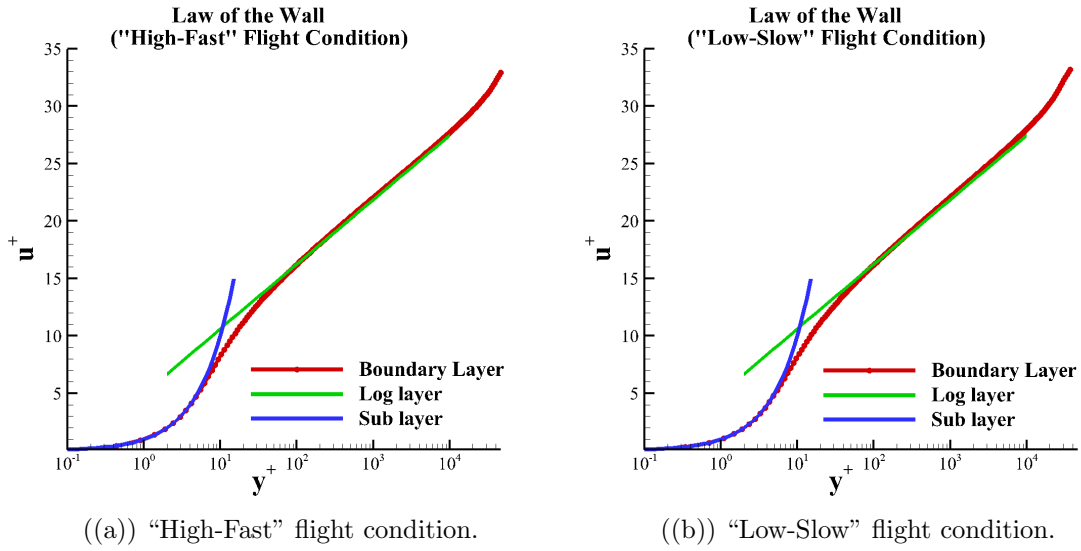
Figure 4.2:   Law of the Wall for both flight conditions

To further examine the theory behind the boundary layer the skin friction coefficient vs. Reynolds number (Re_x) is compared for each boundary layer using the Blasius and White solutions. The theory suggests that the skin friction for laminar flow is significantly less and transitions to turbulent flow at $Re_x \approx 5.5 \times 10^5$. To compute the laminar skin friction coefficient the Blasius solution is used, see Equation 4.3. For the turbulent portion of the skin friction results, the approximation formulated by White [39] was applied, see Eqn. 4.4.

$$C_f \approx \frac{0.455}{ln^2(0.06Re_x)} \qquad (4.3)$$

$$1.15C_f(L) \approx \frac{0.523}{ln^2(0.06Re_L)} \tag{4.4}$$

The results of the skin friction coefficients quantitatively agree with the estimation formulated by White for turbulent boundary layers on a flat plate. The transition between the Blasius solution and White solution was minimal and for visualization purposes was excluded from the plots, see Figure 4.3(a) for the "high-fast" flight condition and Figure 4.3(b) for the "low-slow" flight condition.

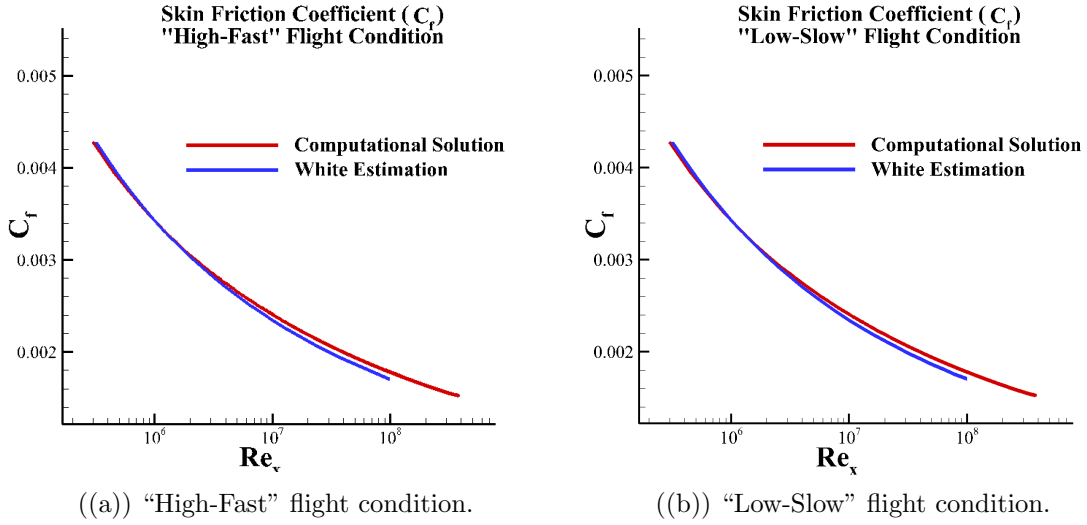((a)) "High-Fast" flight condition.   ((b)) "Low-Slow" flight condition.

Figure 4.3:   Comparison of skin friction coefficient vs. Re_x

Once the boundary layers were compared to theory for both flight conditions, the next step was to extract all desired heights of the boundary layers at 99% of the freestream velocity. For the fully exposed hemisphere, two heights were acquired with heights of 2.5 and 5.0 inches (25% and 50% of the geometry height). For the ten inch submerged geometry, four boundary layer heights were extracted with heights of 2.5, 5.0, 7.5, and 10 inches (25%, 50%, 75%, and 100% of the geometry height). The boundary layer was imposed at the inflow boundary condition at such height that the boundary layer would grow and at the base of the turret reach the desired height.

4.2 Flow Features

The study of aerodynamics on the various turret geometries is crucial in obtaining a better understanding of the parameters that induce higher aero-optical and aero-mechanical jitter for the two flight conditions examined. The flow features created around the geometry are complex and are broken down into components of horseshoe vortex, stagnation region, separation line, shear layer, reverse flow region, horn vortices, lambda shock, and fluctuations of pressure and density to provide an insight into what affects the beam quality. The analysis was conducted by splitting the "high-fast" and "low-slow" simulations into two groups. The comparison of boundary layer heights imposed on symmetrical and non-symmetrical turret geometries was performed to visualize the flow feature trends. Due to the large number of cases and numerous comparisons performed, only the highlights are presented in this section.

4.2.1 Horseshoe Vortex.   The horseshoe vortex, also referred to as a "necklace vortex" is a characteristic flow feature formed around round obstacles like the turret geometry. The horseshoe vortex occurs in numerous applications such as wing-body junctures and has been studied over the last few decades [40–42] in a wide range of applications such as aerodynamics, turbomachinery, submarines, and architectural aerodynamics. The horseshoe vortex is created due to adverse gradients present on the wall upstream of the flow which leads to the flow separation and the creation of a bubble that wraps itself around the geometry in a u-shaped form, ultimately creating the horseshoe vortex [39]. As the Reynolds number increases, the computed flow topology evolves from a singular horseshoe vortex to multiple horseshoe vortices formed around the geometry. At higher Reynolds numbers, the vortex becomes unsteady and cyclic with a frequency that continues to increase with an increase Reynolds number [42]. The horseshoe vortex created upstream of the turret geometry was studied to evaluate the effect it has on the beam. The study is then further expanded to examine the flow features downstream of the turret where the vortex could act as a flow stabilizer by

45

drawing turbulence out of the wake or potentially add to the turbulence in the wake, thus adding to the unsteadiness and generating aero-mechanical jitter.

All figures presented in this subsection are of the iso-surfaces of the vorticity magnitude with surface contours of pressure. Results presented in Figure 4.4 and 4.5 are of the "high-fast" flight condition for the exposed turret geometry symmetric and non-symmetric aperture orientation. The results show that the 25% boundary layer height numerical simulation has one strong horseshoe vortex closest to the turret geometry and a second vortex of significantly smaller size forming further upstream. The formation of the second horseshoe vortex is due to the first vortex acting like a solid wall, causing it to roll up on itself. In addition, the vorticity plots show that there is a third horseshoe vortex starting to form even further upstream of the second vortex. It was also observed that the lower boundary layer simulation has a smaller standoff distance between the turret and the horseshoe vortex than compared to the 50% boundary layer height solution. Further analysis, presented in the 50% boundary layer simulation shows that an increase in boundary layer height reduces the length of the horseshoe vortex traveling downstream. An interesting observation between the 25% and 50% imposed boundary layer heights is that the secondary horseshoe vortex is identical between the two. The trend is also observed for the non-symmetrical aperture orientation (see Figure 4.5) which shows that the horseshoe vortex is identical in size and spreading angle as for the symmetrical geometry.

The solution of the "low-slow" flight condition for the fully exposed symmetric vs. non-symmetric aperture orientations are presented in Figures 4.6 and 4.7, respectively. From the figures, it is observed that an increase in boundary layer height decreases the length of the horseshoe vortex travelling downstream. For this simulation, the Reynolds number was 157,697 per inch compared to the 238,376 per inch Reynolds number of the "high-fast" simulations presented in the figures above. A major difference for this flight condition is the formation of only a secondary vortex of significantly smaller size than observed for the high subsonic simulations. Additionally, no third horseshoe vortex appears to be forming. Further examination of the
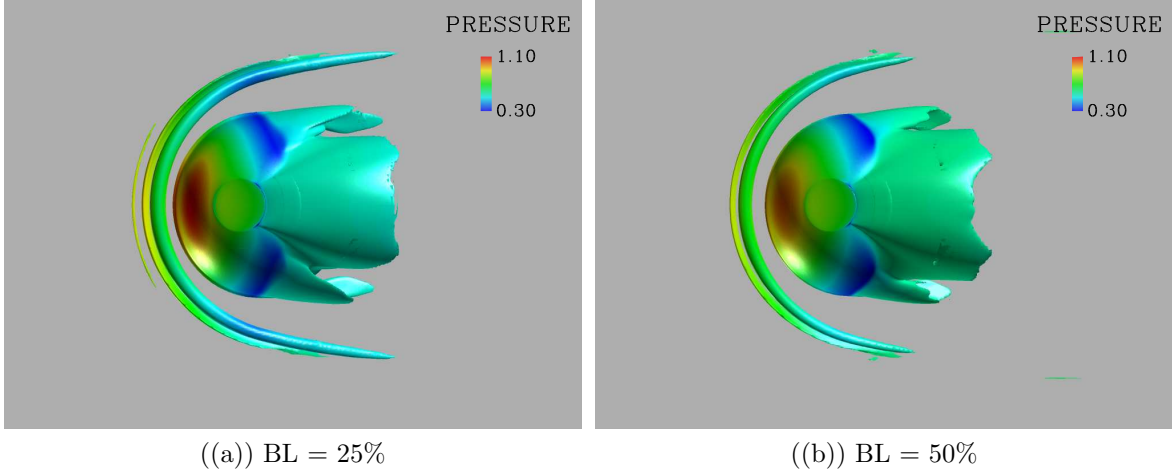
46

((a)) BL = 25%   ((b)) BL = 50%

Figure 4.4:   Vorticity magnitude with contours of pressure for the "high-fast" flight condition of the fully exposed turret geometry (symmetric)
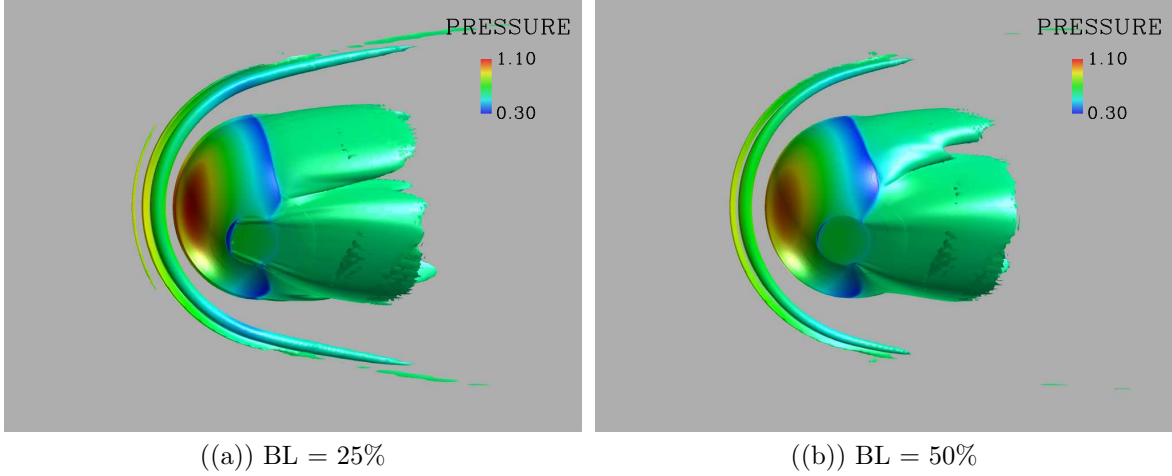

((a)) BL = 25%   ((b)) BL = 50%

Figure 4.5:   Vorticity magnitude with contours of pressure for the "high-fast" flight condition of the fully exposed turret geometry (non-symmetric)

figures showed that the higher boundary layer has a continuously spreading horseshoe vortex as it propagates downstream. The cause of the spreading angle to continue to move outwards, away from the turret geometry for the higher boundary layer simulation is due to the separation region of the turret which reattaches to the flat plate creating a two part wake in the rear of the turret. As observed for the high speed case, the difference between the symmetric vs. non-symmetric geometry does not affect the formation of the horseshoe vortex; the reason is due to the aperture location being too far downstream to make an impact.
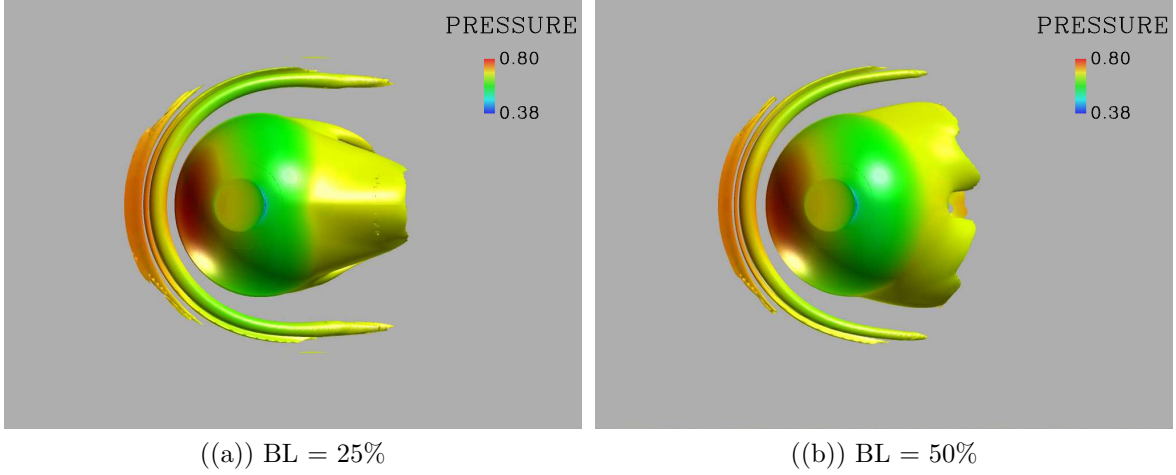
47

((a)) BL = 25%	((b)) BL = 50%

Figure 4.6:   Vorticity magnitude with contours of pressure for the "low-slow" flight condition of the fully exposed turret geometry (symmetric)
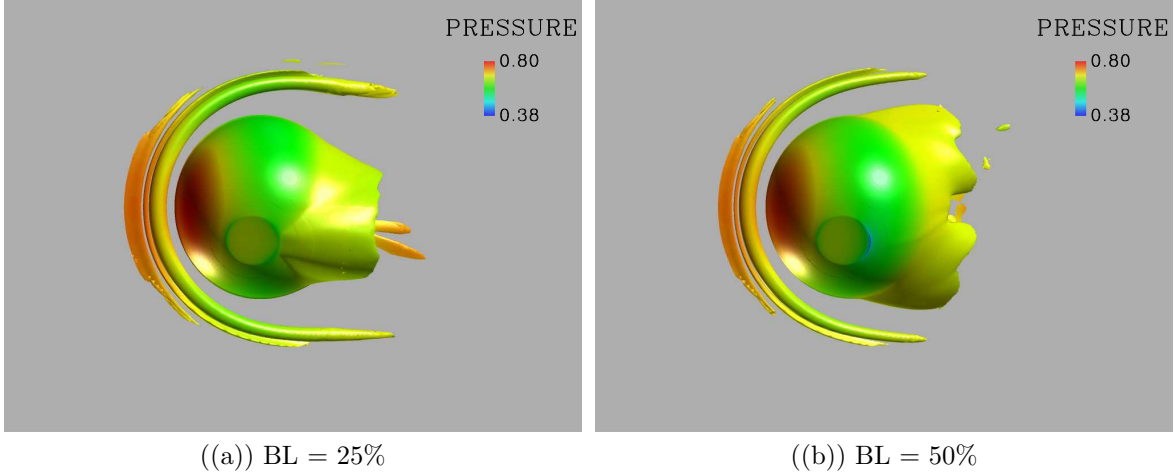

((a)) BL = 25%	((b)) BL = 50%

Figure 4.7:   Vorticity magnitude with contours of pressure for the "low-slow" flight condition of the fully exposed turret geometry (non-symmetric)

The results of the submerged turret geometries for the "high-fast and "low-slow" flight conditions are presented in Figures 4.8 and 4.9. Similar trends are observed as for the fully exposed geometries discussed above; the length of the horseshoe vortex diminishes as the boundary layer is increased and the spreading angle is qualitatively observed to be unaffected which is the result of a wake region not splitting in half, as observed for the fully exposed geometry. The main difference between the exposed and submerged geometries is the vortex standoff distance where the submerged simulations presents a smaller distance between the turret and horseshoe vortex. The difference

between the exposed and submerged geometries is that the aperture is closer to the flat plate creating a small expansion region; this reduces the standoff distance between the vortex and the geometry due to the delay in pressure gradients. Further analysis of the cases not presented in this section show that the trends observed occur for all simulations conducted.
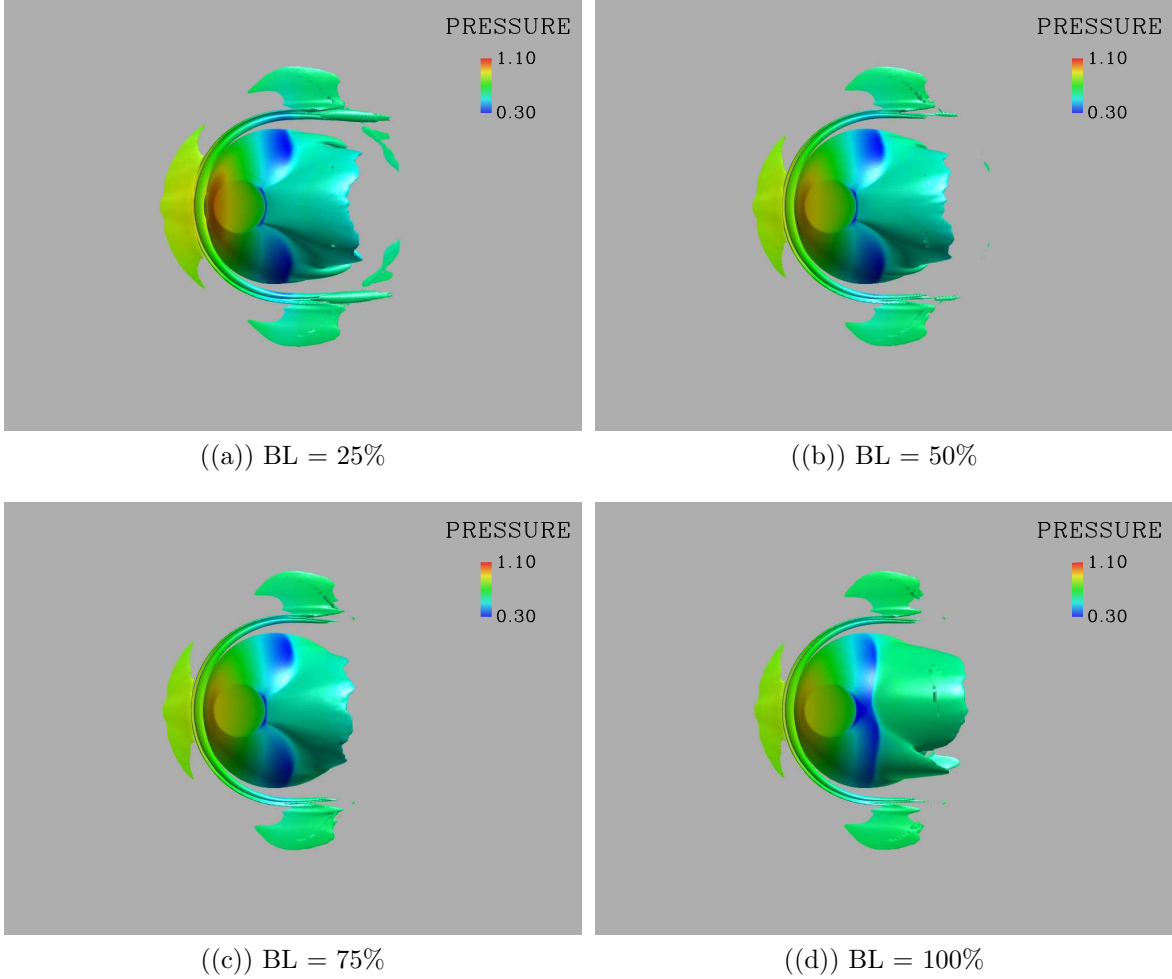

((a)) BL = 25%

((b)) BL = 50%

((c)) BL = 75%

((d)) BL = 100%

Figure 4.8:   Vorticity magnitude with contours of pressure for the "high-fast" flight condition of the submerged turret geometry (symmetric)

The analysis focusing on the horseshoe vortex shows that an increase in boundary layer height will reduce the distance of the horseshoe vortex propagating downstream, for both the exposed and submerged turret geometries. For the submerged case, the horseshoe vortex occurs closer to the geometry, the location of the horseshoe
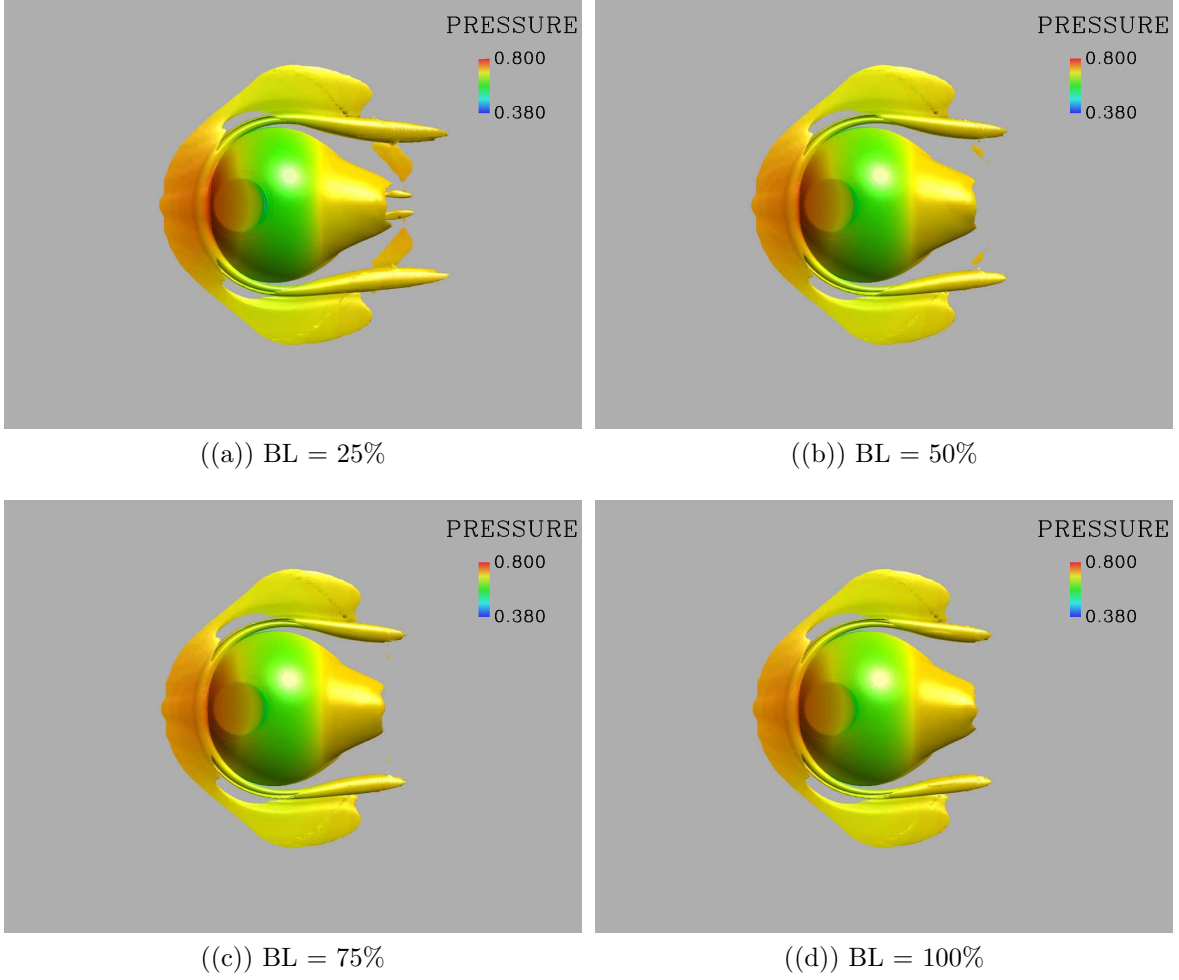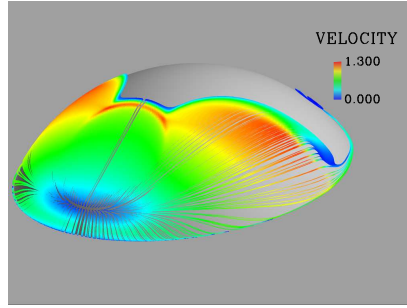
((a)) BL = 25%   ((b)) BL = 50%

((c)) BL = 75%   ((d)) BL = 100%

Figure 4.9:   Vorticity magnitude with contours of pressure for the "low-slow" flight condition of the submerged turret geometry (symmetric)

vortex closer to the path of the beam could potentially create additional density fluctuations. When analyzing the difference between symmetrical vs. non-symmetrical simulations, it was concluded that the structure of the horseshoe vortex was not affected by aperture orientation. Consequently, just from the analysis of the horseshoe vortex, the results exhibit a "best-case" scenario for the fully exposed turret geometry with 50% boundary layer height because the horseshoe vortex has the largest standoff distance and the magnitude of the vortex is smallest. The "worst-case" occurs for the submerged turret geometry because the standoff distance between the geometry and vortex is the smallest. The horseshoe vortex near the aperture window could add

50

velocity gradients that lead to a higher density fluctuation and possibly reduce the beam quality. The impact of the horseshoe vortex will be analyzed in further detail through the use of density fluctuations.

4.2.2 Stagnation Region. The stagnation point is located at the center of the front half turret of the geometry and is the point at which velocity is zero and cannot disperse in any direction, making the flow stagnant. Due to the velocity being equal to zero, the total pressure reaches its maximum magnitude at that location, except in shock regions. Although it may appear that the stagnation region is not nearly as dominant in the impact of aero-mechanical and aero-optical jitter, it is the building block from which all flow structures evolve. The analysis of the stagnation region is conducted by plotting surface streamlines of the velocity magnitude. Due to the velocity directly on the surface equaling to zero, the streamlines are obtained a few points away from the wall, at approximately 1/16 of an inch. By constraining the surface streamlines to a standoff distance of 1/16 of an inch, the streamlines that separate away from the wall disappear and the result is the visualization of the surface flow structures.

The results presented in Figure 4.10 are of the "high-fast" flight condition for the submerged turret geometry with an isometric view (left) and frontal view (right). The average of the unsteady solutions was used in this scenario to get the best representation of the mean flow. The results presented show that the stagnation region is fairly unchanged for all boundary layer heights imposed on the geometry. Although hardly noticeable in small scale pictures, the whole stagnation region does spread into a larger high pressure area and decreases in magnitude as the boundary layer height increases. The result of having a larger region of high pressure with a slightly lower magnitude reduces the change in velocity as the fluid moves over the surface. The result is a delay in the separation region and a reduction in fluctuations is expected as the boundary layer increases.
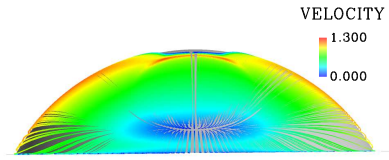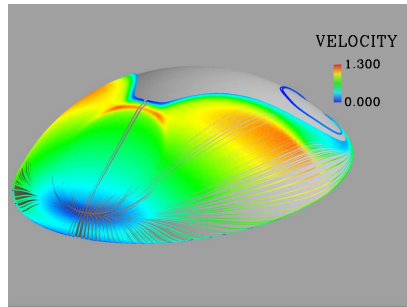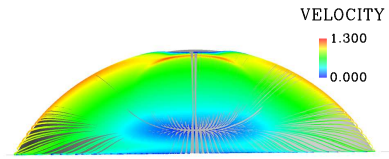
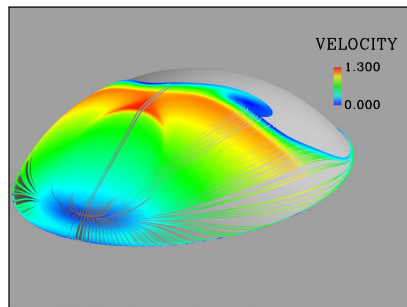((a)) BL = 25%
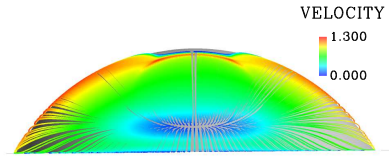
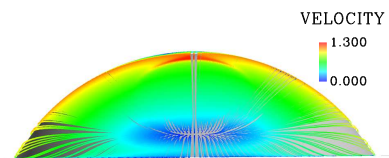((b)) BL = 25%
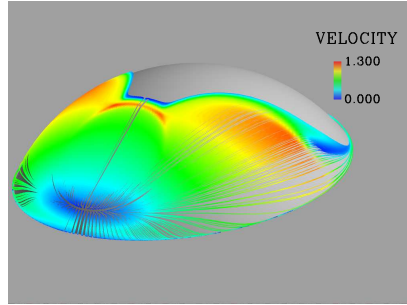
((c)) BL = 50%

((d)) BL = 50%

((e)) BL = 75%

((f)) BL = 75%

((g)) BL = 100%

((h)) BL = 100%

Figure 4.10:   Surface streamlines for the "high-fast" flight condition of the submerged turret (symmetric)

The analysis of the stagnation region for all numerical simulations conducted shows that the variations in boundary layer heights have minimal effects on the stagnation region. The location of the stagnation point is below the aperture for all cases and does not interfere with the aperture for the fully exposed turret geometries and has a minimal effect in the submerged simulations. Because the flow in the front half of the turret is mainly laminar, the stagnation region is stationary, which was observed in the transient data simulations.

4.2.3   Separation Line, Horn Vortices, and Shear Layer.   This section discusses the flow features as the fluid flows over the geometry into the wake. The focus is to understand how variations in boundary layer height change the location of the separation line, shear layer, and the formation of horn vortices which all influence the wake of the turret region. A more turbulent wake region induces a higher aero-mechanical jitter on the turret geometry, making it crucial to understand the fundamental flow features that result in the creation of the complex wake. To visualize the flow features, surface streamlines were used to determine the location of the horn vortices and separation line. For the qualitative analysis of the shear layer, iso-surfaces of the vorticity magnitude with contours of pressure, planar cuts of Mach number, and magnitude of the density gradient were examined. The separation line is formed due to an adverse pressure gradient at which the flow transitions from laminar to turbulent flow, creating a complex and unsteady flow structure in the wake. The results presented in Figure 4.11 are for the fully exposed turret geometry of the "high-fast" flight condition for the symmetrical and non-symmetrical case using surface streamlines with contours of velocity magnitude. The comparison between the 25% and 50% boundary layer shows that an increase in boundary layer height slightly delays the separation. By delaying the separation, the pressure gradients occur further downstream of the aperture, potentially reducing the aero-mechanical jitter.

The results presented in Figure 4.12 are of the fully exposed turret geometry for the "low-slow" flight condition for both symmetrical and non-symmetrical aperture

orientation. The surface streamlines show that for the 50% boundary layer height the flow stays attached longer. The result should exhibit lower aero-mechanical jitter because the turret wake contains less turbulence, ultimately creating lower pressure drag on the geometry. Further analysis shows that the separation is delayed on the top part of the turret but transitions on the sides, near the plate further upstream to turbulent flow. The cause of the separation on the sides is due to the interaction between the flat plate and the turret creating an unfavorable pressure gradient that forms a separation approximately 20% further upstream than for the lower boundary layer heights.

Further examination of the boundary layer height performed on the submerged cases for both "high-fast" and "low-slow" flight conditions showed that the same trends occur; an increase in boundary layer height delays the separation. The difference between the submerged and exposed turret geometries is the delay in separation of the flow on the side of the turret for the submerged geometries, but transitions earlier for the exposed geometries. The angle of the aperture on the turret housing creates a Prandtl-Meyer expansion at the upper and lower lip of the turret aperture. Using the surface streamlines with contours of velocity magnitude, a comparison between the various boundary layer heights shows that an increase in boundary layer reduces the magnitude of velocity as the flow expands over the edges of the aperture. Of all 24 simulations performed, the "high-fast" submerged turret with 100% boundary layer height presented in Figure 4.13 has a significantly reduced separation but a much larger expansion region that is uniform along the centerline of the turret. The high boundary layer creates a smaller variation in velocity allowing the flow to smoothly pass over the turret with minimal effects of the expansions. Towards the top of the turret, the flow eventually accelerates, creating a shock following the expansion. Comparing the "low-slow" and "high-fast" flight conditions side by side, it is determined that the trend of delay in separation occurs for all increases in boundary layer. The discontinous changes in the geometry formed by the flat window, leads to a non-uniform separation line. Around the aperture edges the expansions form the
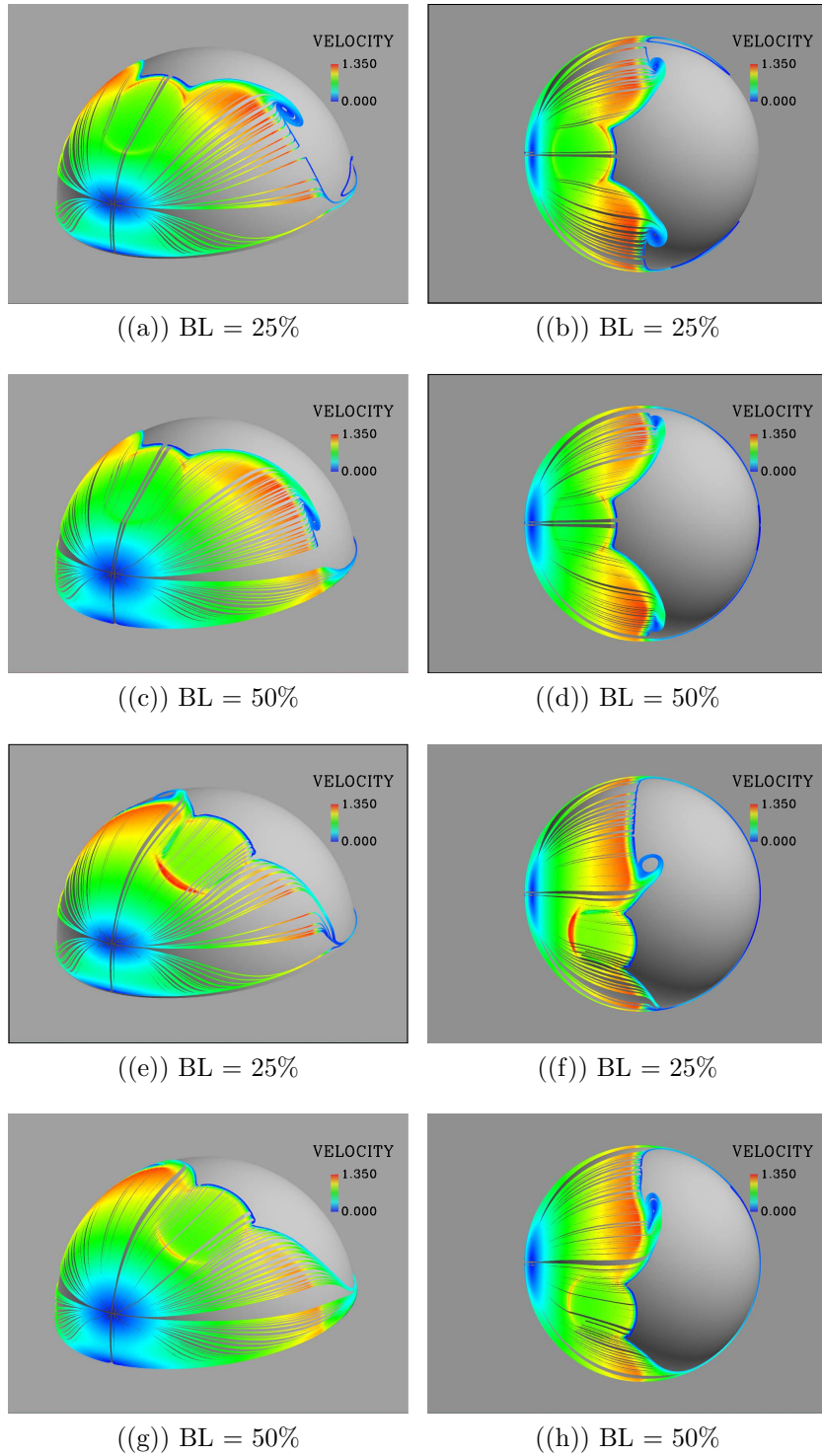
((a)) BL = 25%   ((b)) BL = 25%

((c)) BL = 50%   ((d)) BL = 50%

((e)) BL = 25%   ((f)) BL = 25%

((g)) BL = 50%   ((h)) BL = 50%

Figure 4.11:   Surface streamlines for the "high-fast" flight condition of the fully exposed turret

((a)) BL = 25%   ((b)) BL = 25%

((c)) BL = 50%   ((d)) BL = 50%

((e)) BL = 25%   ((f)) BL = 25%

((g)) BL = 50%   ((h)) BL = 50%
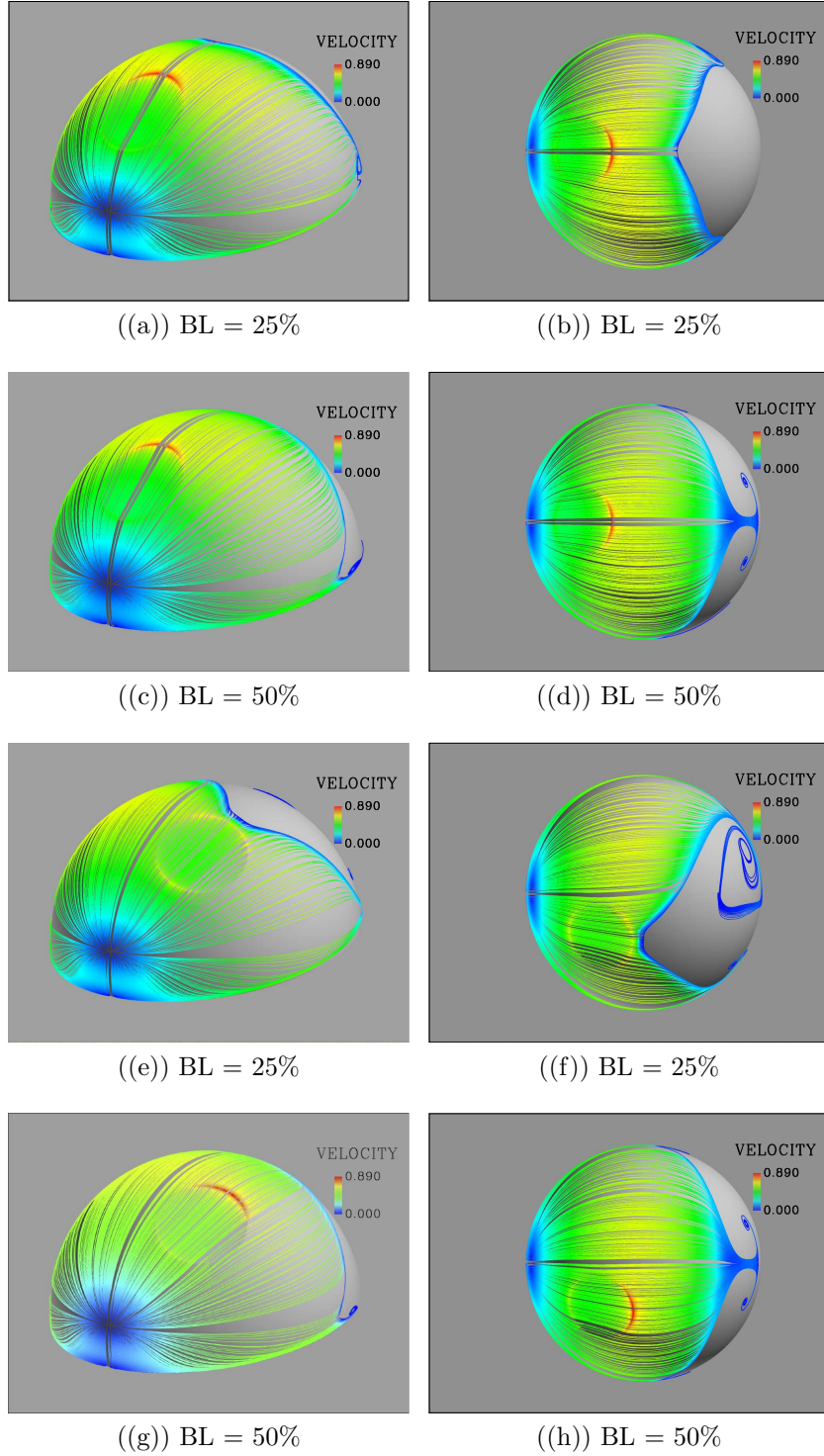
Figure 4.12:   Surface streamlines for the "low-slow" flight condition of the fully exposed turret with varying aperture orientations

separation lines further upstream while the smooth curvature of the flow delays the separation on the sides. In the numerical simulations of the low subsonic velocity, the flow does not cause a significant expansion over the turret aperture and remains attached until the wake and the flow collapses on itself creating a separation.
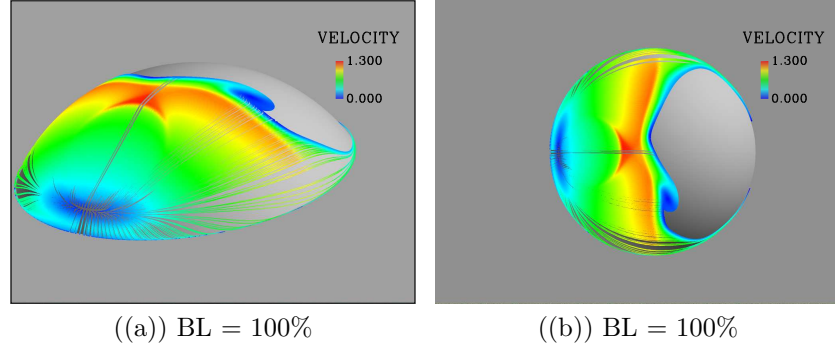

((a)) BL = 100%   ((b)) BL = 100%

Figure 4.13:   Surface streamlines for the "high-fast" flight condition of the submerged turret (symmetric)

The study of the separation line can then be expanded into the so called horn-vortices which are vortices that emanate from the surface of the turret. The horn-vortices are formed in the recirculation region of the turret where the fluid travels upstream. As the slower moving fluid is travelling upstream in the recirculation region it is repelled by the shear layer creating a vortex as it emanates from the surface. Examining Figure 4.11 of the fully exposed turret geometry, it was determined that the horn-vortices are formed further upstream because of the shear layer formation just aft of the aperture. The formation of the "horn-vortices" is present in all cases, occuring right after the shear layer. For the transonic flight condition they are formed further upstream and for the low subsonic regime, the formation occurs further downstream.

To examine the recirculation region in the wake of the cylinder, iso-surfaces of the negative u-velocity were created. This is an intermediate step in the analysis in order for the reader to visualize how large the recirculation is for each of the cases prior to the discussion on shear layers. The solution files used to visualize the recirculation region are the average of the unsteady flow for 50,000 iterations. The purpose of employing the iso-surfaces of reverse flow was to capture the separation immediately

57

off the wall as it occurs. The result is the true location of the separation region, unlike for the surface streamline which were a short distance away from the wall.

The results presented in Figure 4.14 are of the "high-fast" flight condition for the fully exposed turret symmetric and non-symmetric geometry. The observation to be made is that the separation starts to occur right at the top lip of the aperture, this is easily explained due to the expansion created by the turret geometry that transitions the flow. The air propagating along the sides of the turret remain attached further downstream. The results show that an increase in boundary layer height does keep the flow attached longer, especially around the wall and turret junction. The result is a longer, narrow recirculation region formed in the wake of the turret geometry. Consequently, the higher boundary layer cases do not create a recirculation region that tries to attach to the wall which would form higher pressure fluctuations on the turret geometry. The same trend is observed for the non-symmetric case where the increase in boundary layer allows the flow around the bottom of the turret geometry to stay attached, creating a smaller area of separation along the turret surface.

The examination of the "low-slow" flight condition of the fully exposed turret geometry, shown in Figure 4.15, presents a different recirculation region between the two boundary layer heights. For the 25% simulation, the flow separates significantly earlier compared to the 50% case which has a recirculation region that is formed along the sides between the turret and flat plate junction. The formation of the different recirculation region observed for these cases is formed by the delay in separation for the higher boundary layer case which splits the wake into two regions once it separates, whereas the low boundary layer simulation separates earlier and the flow is not able to reattach with the flat plate behind the turret, resulting in the creation of a larger interaction region.
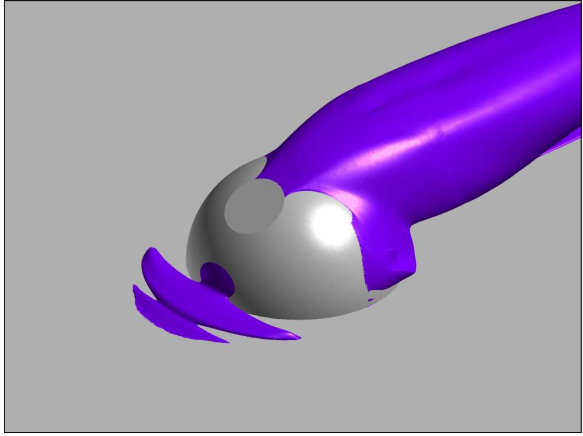
Another difference between the recirculation regions for the high and low subsonic flight conditions is the size of the wake. The "high-fast" flight condition creates a wake that is approximately 4-5 times the size of the "low-slow" case.
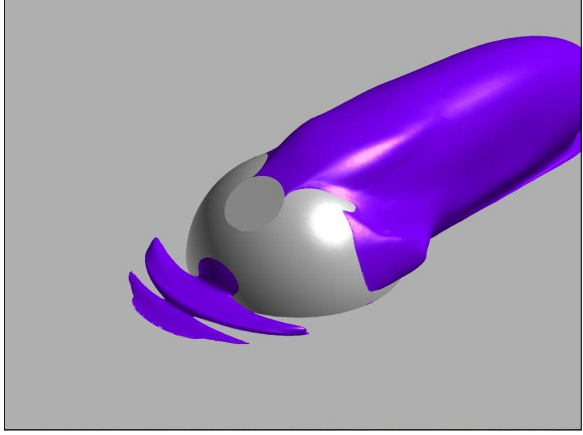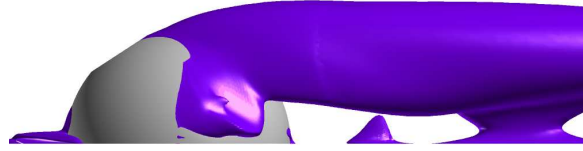
((a)) BL = 25%
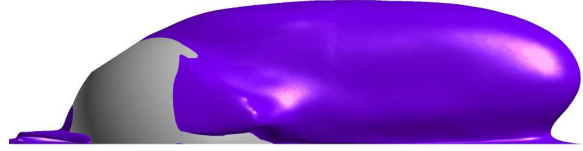
((b)) BL = 25%

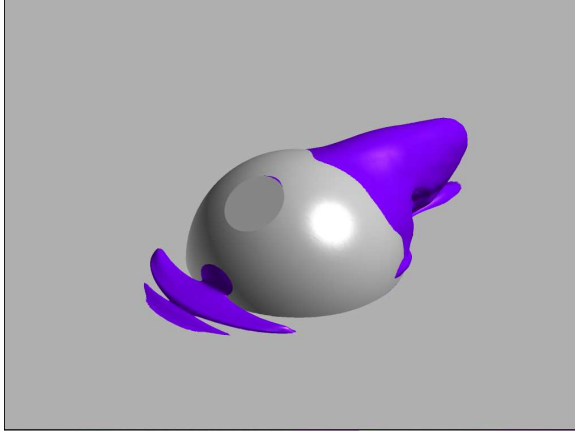((c)) BL = 50%
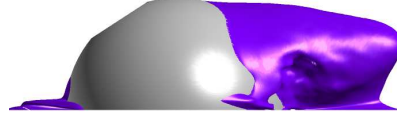

((d)) BL = 50%

Figure 4.14:   Iso-surfaces of the negative u-velocity for the "high-fast" flight condition of the exposed turret geometry

To focus on the shear layer formation over the turret geometries, flow structures were visualized by contours of Mach number along the centerline of the turret and 2.5 inches off the flat plate with surface contours of pressure. The discontinuous turret geometry created by the aperture forms a shear layer at the upper lip of the aperture and along the sides of the turret for the "high-fast" flight condition, see Figure 4.16. The surface contours of pressure agree with the contour plots Mach number to show that an oblique shock is formed around the sides of the turret and an expansion on the top. For the low subsonic flight condition the shear layer is formed downstream of the aperture due the pressure gradient, see Figure 4.17. The surface contours of
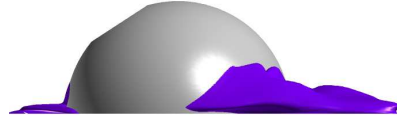
((a)) BL = 25%   ((b)) BL = 25%
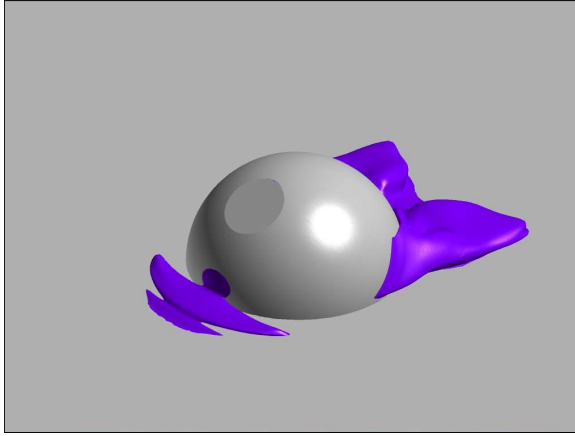
((c)) BL = 50%   ((d)) BL = 50%

Figure 4.15:   Iso-surfaces of the negative u-velocity for the "low-slow" flight condition of the exposed turret geometry

pressure reveal that there is a pressure drop along the upper lip of the aperture and in the wake of the turret geometry. This creates two shear layers where the first one upstream is fairly quickly dissipated and the second one, further downstream, separates and creates a mixing region with the wake.

Presented in Figure 4.18 are coordinate surface cuts of Mach number along the centerline and parallel to the flat plate with contours of pressure along the turret surface for the fully exposed turret geometry of symmetrical and asymmetrical aperture orientation.
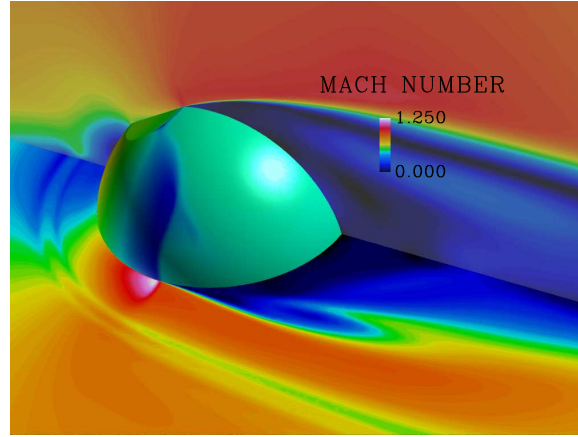
((a)) BL = 50%

Figure 4.16:   Mach number contours and surface contours of pressure for the "high-fast" flight condition of the exposed turret
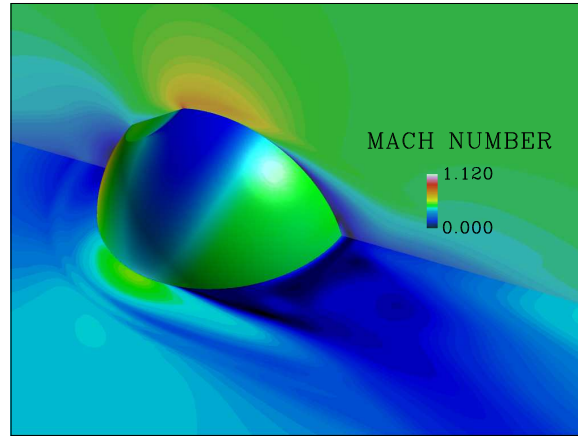
((a)) BL = 50%

Figure 4.17:   Mach number contours and surface contours of pressure for the "low-slow" flight condition of the exposed turret

By employing just the contours of the Mach number, the visualization of the flow is fairly two-dimensional, making it hard to analyze the difference in boundary layer heights and symmetric vs. non-symmetric geometries. Hence, to improve the flow visualization of the shear layer into a three-dimensional perspective, plots of the iso-surfaces of vorticity magnitude were examined. The results of the iso-vorticity magnitude for the fully exposed turret geometry with aperture orientation symmetric and non-symmetric are presented in Figure 4.19.
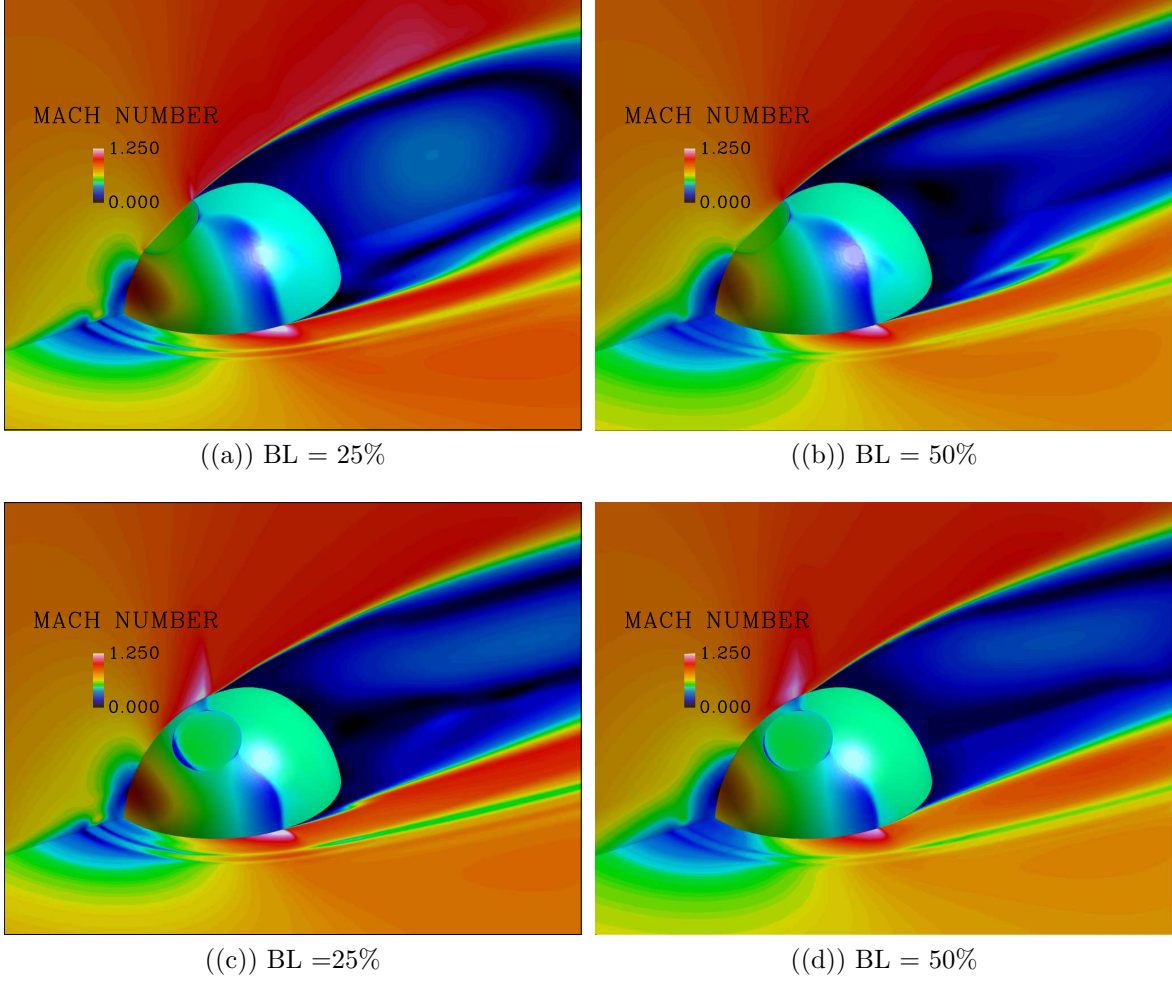
((a)) BL = 25%   ((b)) BL = 50%

((c)) BL =25%   ((d)) BL = 50%

Figure 4.18:   Mach number contours and surface contours of pressure for the "high-fast" flight condition of the exposed turret

The results discussed using surface streamlines and reverse flow plots demonstrated that an increase in boundary layer height delays the separation further downstream. The results presented using the Mach number and iso-surfaces of the vorticity magnitude also show that due to the delayed separation the shear layer is delayed. The observation to be made from the iso-surfaces of the vorticity magnitude is that the shear layer is smoother at higher boundary layers, meaning the edges between the three sections of the shear layer, created from the discontinuity of the geometry due to the flat window left, middle, and right side are not as discontinuous. The same

((a)) BL = 25%   ((b)) BL = 50%

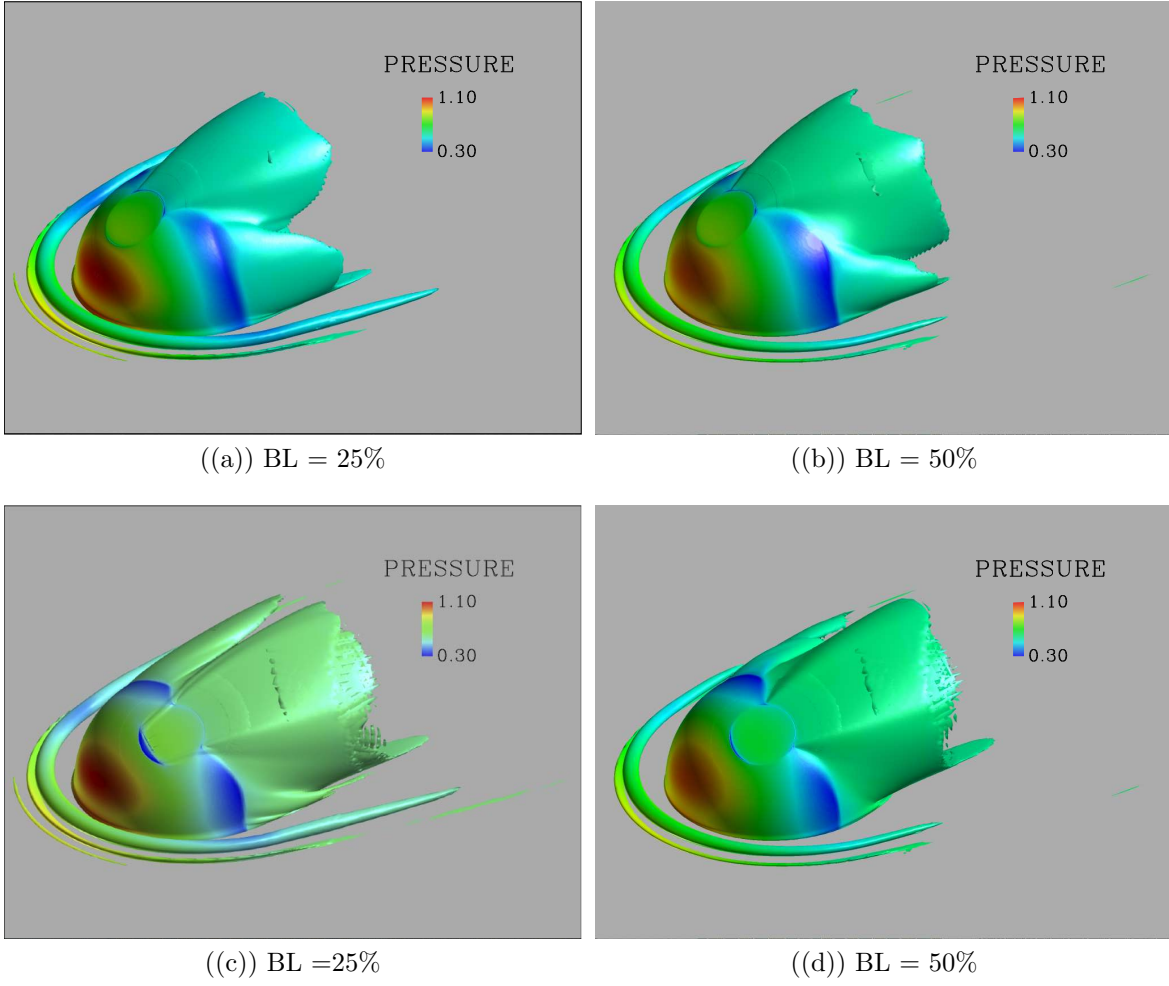((c)) BL =25%   ((d)) BL = 50%

Figure 4.19:   Iso-surfaces of the vorticity magnitude with surface contours of pressure for the "high-fast" flight condition

observation of a less discontinous shear layer is observed for the submerged turret case presented in Figure 4.20

((a)) BL = 25%

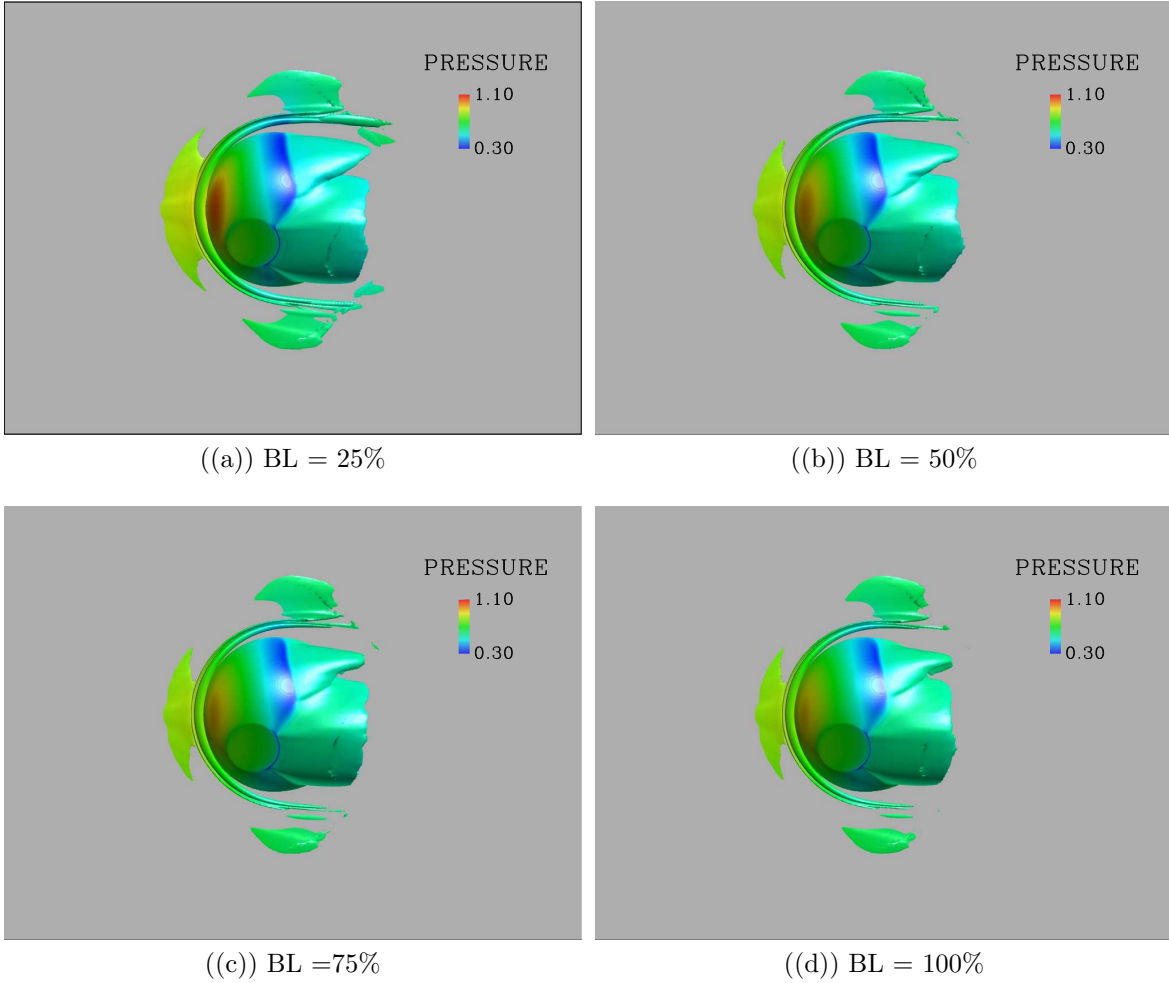((b)) BL = 50%

((c)) BL =75%

((d)) BL = 100%

Figure 4.20:   Iso-surfaces of the vorticity magnitude with surface contours of pressure for the "high-fast" flight condition for the submerged non-symmetric geometry

4.2.4 Oblique Shock and Expansion. The blunt geometry studied in this thesis at "high-fast" flight conditions is subject to an expansion forming at the upper lip of the aperture and an oblique shock occurring at the sides and following the expansion. The expansion forming at the aperture's upper lip is due to the change in curvature that propels the fluid, creating a Prandtl-Meyer expansion wave. Although there is an expansion region at the lower lip of the aperture, due to the stagnation region, interference of the horseshoe vortex, and an interaction with the boundary layer the flow is not at a high enough velocity for a shock to occur. As a result of the expansion over the top of the turret geometry, the Mach number increases and the pressure, temperature, and density decrease; following the expansion a shock occurs which is due to the increase in velocity. The phenomenon of an expansion to shock over such a short distance is referred to as a lambda (λ) shock. The disturbance is caused by the rapid increase in velocity and followed by a shock that creates flow structures that could potentially interfere with the laser beam via aero-optical jitter and the turret structure causing aero-mechanical jitter.

To visualize the formation of the lambda shock in higher detail, surface contours of the magnitude of density gradient along the centerline and 2.5 inches of the flat plate in addition to surface contours of pressure were employed. Density gradient is the variation in density over an area and clearly shows the lambda shock formed over the surface aperture, see Figure 4.21 for the "high-fast" flight condition of the symmetrical fully exposed turret geometry with an imposed boundary layer of 25%. The results of density gradient show that the density variation is highest around the aperture edges due to the expansion forming, causing a high variation in index of refraction creating an aberration on the laser beam. The solution presented in Figure 4.21 is of the average of the unsteady data, which washes out any small flow structures. The fluctuations and flow structures formed in the wake of the turret were analyzed through simulations of the transient data, which showed an oscillation in the density gradient formed by the unsteadiness of the flow. To visualize the variation of density over time, an unsteady solution was saved in increments of 250 iterations for all cases

simulated. An example of the unsteadiness and smaller flow structures observed is presented in Figure 4.22 which shows an oscillation in the expansion fan, the oblique shocks, and the surface pressure in the rear of the geometry.

For further analysis the density gradient magnitude was evaluated at various boundary layer heights and the results show a decrease in the density gradient magnitude as the boundary layer height was increased. As mentioned in the above sections and examined through several flow visualization tools, an increased boundary layer delays the separation hence reducing the magnitude of the expansion and oblique shock magnitudes. For the higher boundary layer heights it was observed that the density variations are not as strong for both the fully exposed and submerged turret geometry. Additional observations that stood out from the transient data which are not visually present in the average of the unsteady solution are the shocks forming over the shear layer. The shocks are of high unsteadiness and oscillate over time due to the shedding created by the blunt geometry.
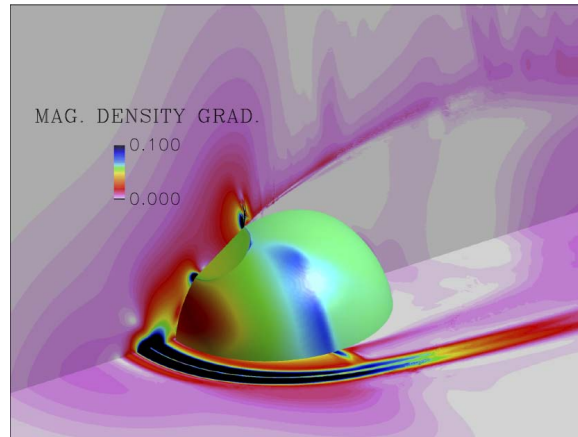
((a)) BL = 25%

Figure 4.21: Magnitude of the density gradient for the "high-fast" flight condition on the exposed turret geometry

Further analysis of the "high-fast" flight condition showed a more dominant interaction between the shear layer and the flat plate surface for the submerged geometry. The angle at which the shear layer is created in the wake of the turret is significantly closer to the flat plate for the submerged case than for the fully exposed
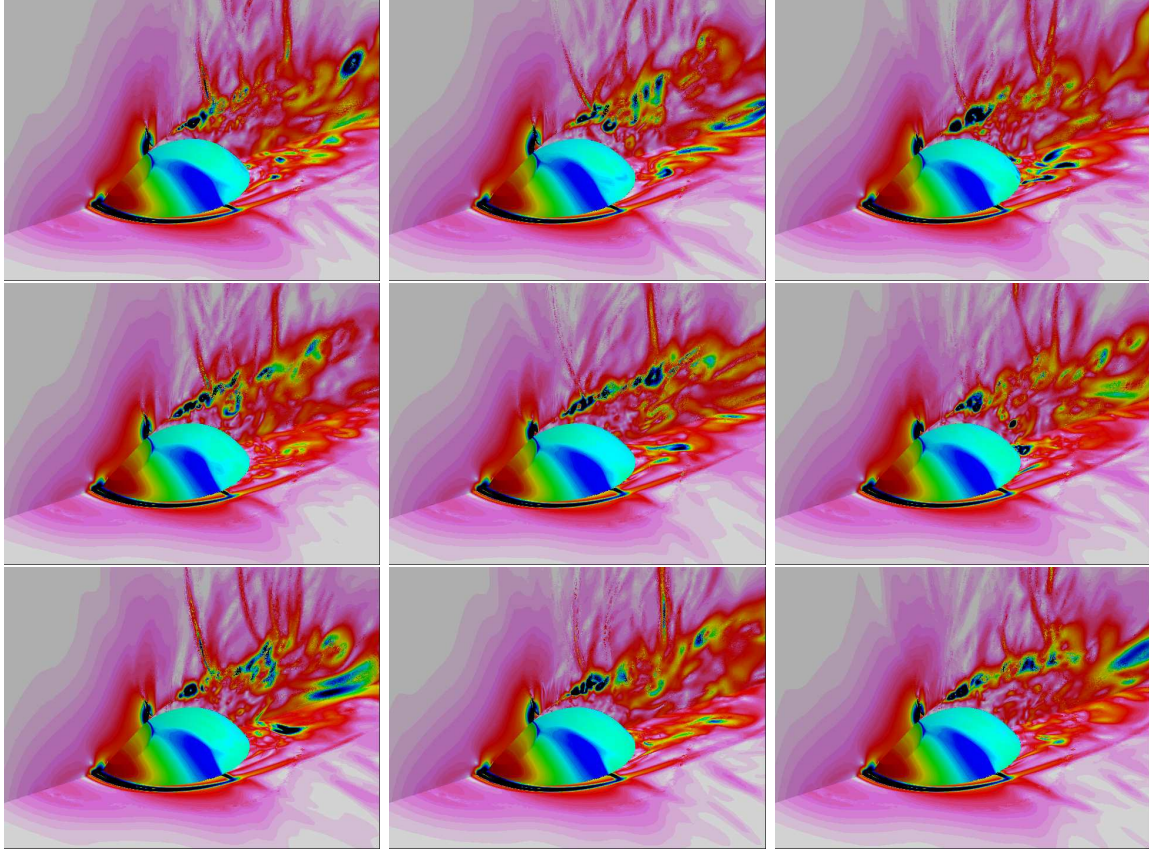
Figure 4.22:   Magnitude of the density gradient for the "high-fast" flight condition using instantaneous solutions at increments of 250 iterations on the submerged turret geometry with 50% boundary layer height

turret geometry. The result is a wake high in turbulent kinetic energy that forms an active interaction between the shear layer and the flat plate in the wake of the geometry. From the visualization of the flow structures it is assumed that the aeromechanical jitter observed by the exposed turret geometry, see Figure 4.23 is less than for the submerged turret geometries, referenced in Figure 4.22.

One of the exceptions observed via the magnitude of the density gradient is when the submerged turret geometry is at an imposed boundary layer of 100%, see Figure 4.24(d). The result shows that a high enough boundary layer can create an expansion that leads to a much stronger oblique shock than observed for the other boundary layers. The results show that an increase in boundary layer imposed from 25% to 75%, the size and magnitude of the expansion and shock formed around the geometry
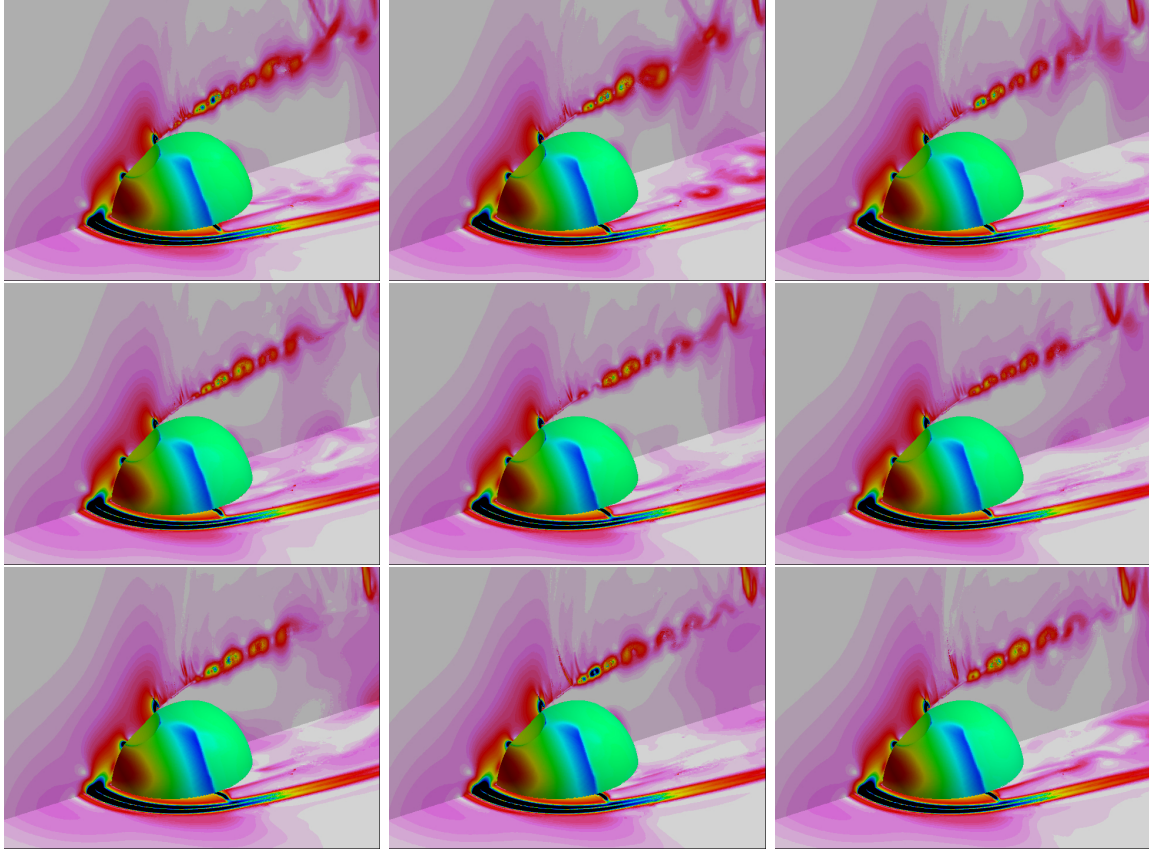
67

Figure 4.23: Magnitude of the density gradient for the "high-fast" flight condition using instantaneous solutions at increments of 250 iterations on the exposed turret geometry with boundary layer height of 25%.

decrease. For the boundary layer height of 100% imposed on the turret geometry, the numerical simulation shows a larger shock at the upper lip of the aperture. Through the examination of the surface contours, the results show a more uniform oblique shock forming around the turret for the high boundary layer simulation. However, as the boundary layer is increased, the oblique shock occurring on the sides of the geometry is decreased.
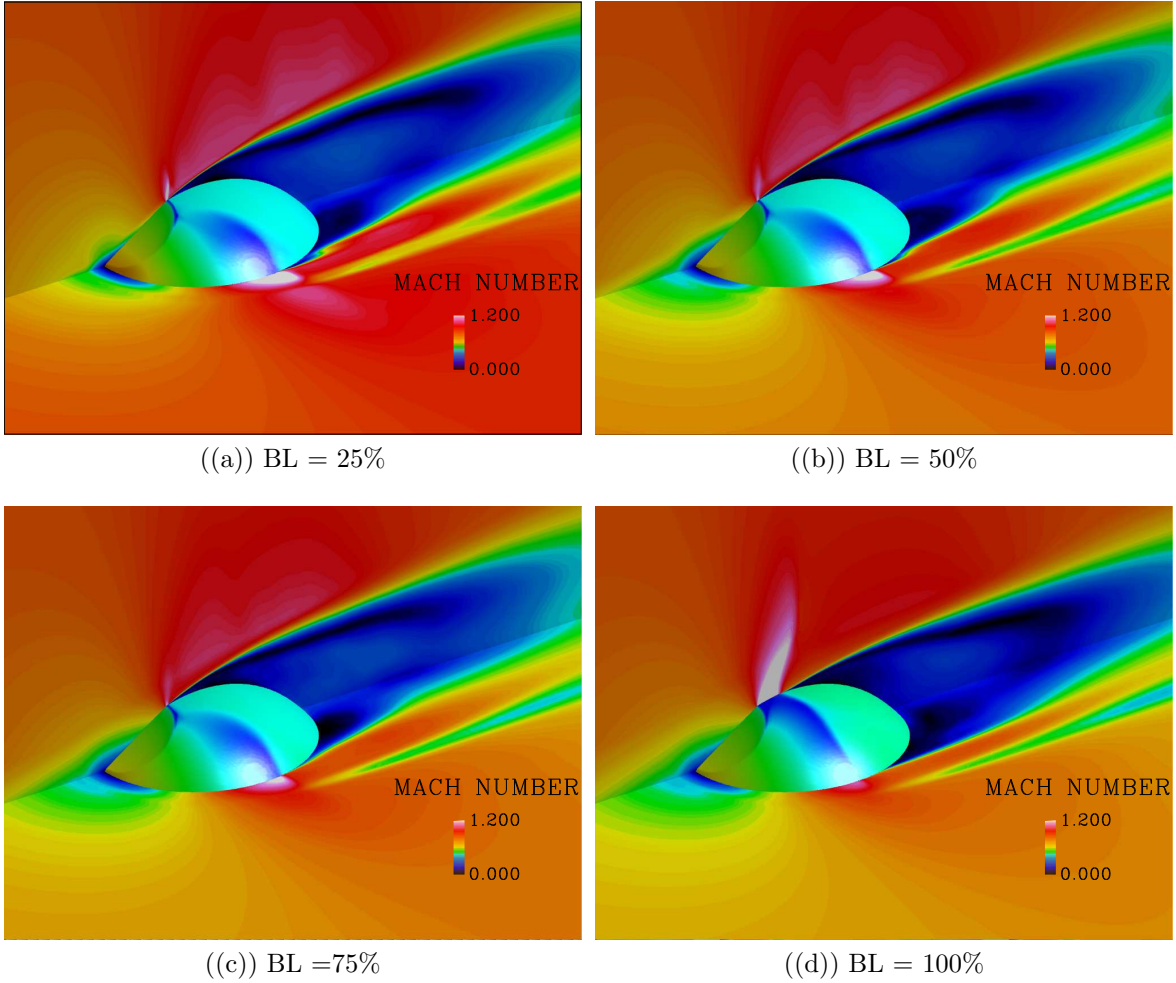
((a)) BL = 25%

((b)) BL = 50%

((c)) BL =75%

((d)) BL = 100%

Figure 4.24:   Mach number contours and surface contours of pressure for the "high-fast" flight condition of the submerged turret

4.3 Pressure Fluctuation on Surface

One of many capabilities implemented into OVERFLOW is to save the average of the pressure perturbations (P'^2) which was employed to analyze the pressure fluctuations along the surface of the turret and the flat plate. The visualization and discussion of the flow features presented in the previous sections led to some qualitative observations that were used to predict the pressure fluctuation on the geometry as an average over time and for instantaneous solutions. Although this section presents the results as qualitative data, the results provided are related to the aero-mechanical jitter and can be used as a vital tool to quantify the jitter induced with further analysis.

The results presented in Figures 4.25 and 4.26 are for the symmetrical and non-symmetrical submerged turret geometry of the "high-fast" flight condition for the submerged symmetrical turret geometry. The results confirm the observed trends discussed in the flow features section that an increase in boundary layer height decreases the pressure fluctuation on the surface of the turret and in the wake of the geometry on the flat plate. For the 100% boundary layer height simulation, as it was observed through the visualization of the other flow features, the flow stays attached until past the aperture and then expands as it reaches the highest point of the geometry in the wake. Although these results provide a higher pressure fluctuation along the centerline of the turret, the pressure fluctuation in the wake of the turret is significantly smaller. It should be noted that the turbulence model employs a RANS model in the boundary layer and an LES model in the separated regions. There are fluctuations in the front half of the turret but due to the RANS model, which averages the flow quantities out, the results appear steady. In the rear half of the turret, the flow separates and the DDES model uses the LES capability to capture the fluctuations by modeling the smaller flow structures.

The results of the "low-slow" flight condition are similar as for the "high-fast" flight condition, the delayed separation reduces the magnitude and area of the pressure
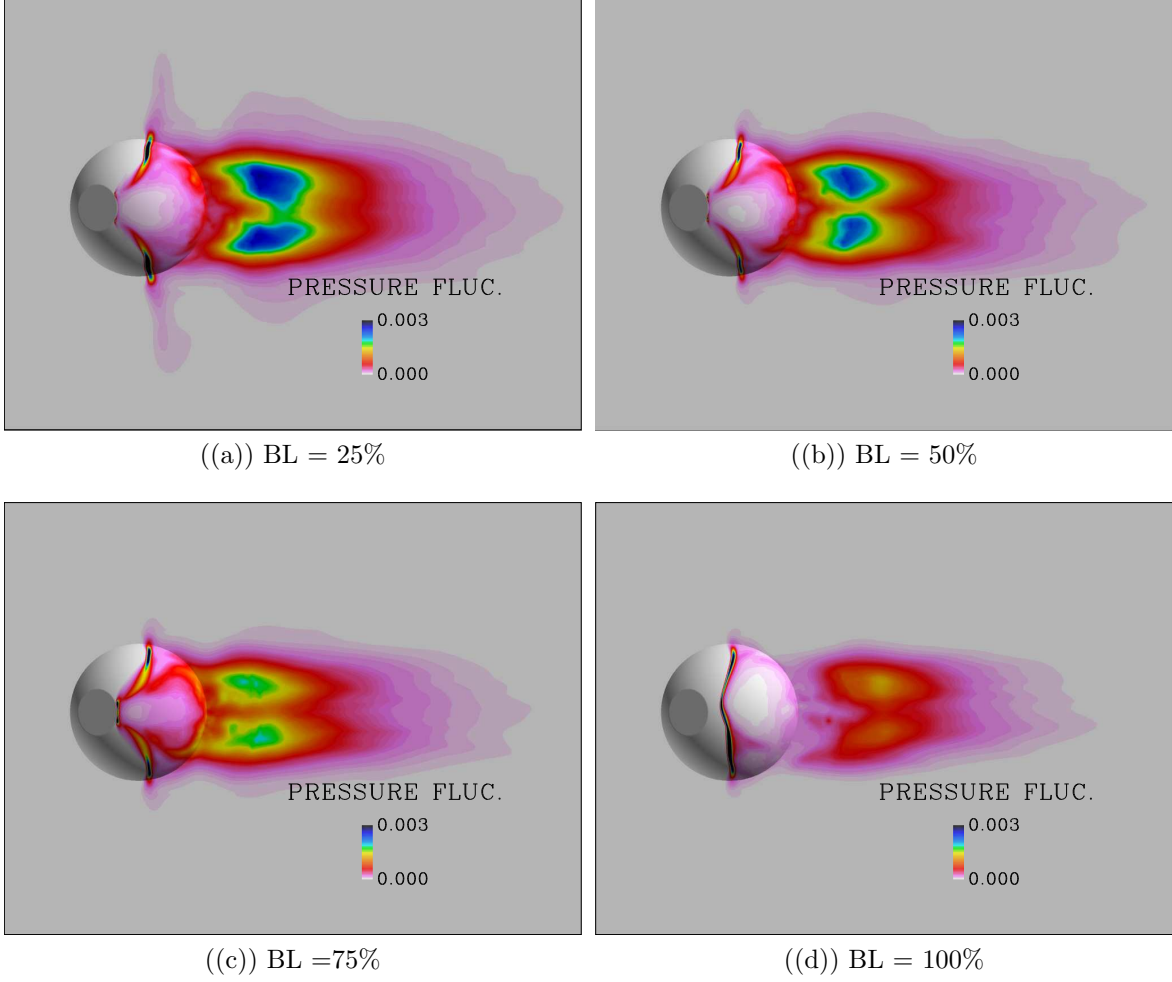
((a)) BL = 25% ((b)) BL = 50%

((c)) BL =75% ((d)) BL = 100%

Figure 4.25:   Pressure fluctuations (P'^2) on the surface of the submerged symmet-
rical turret geometry and flat plate for the "high-fast" flight condition

fluctuations in the wake of the turret., see Figure 4.27 and 4.28. Even though the
results presented in Figure 4.25 are of a symmetric geometry, the results are not
identical across the symmetry plane; the reason is that the simulation would have
to be simulated longer for the fluctuations to be presented identically on both sides.
Overall, the results presented through the pressure fluctuations show a common trend,
the increase of boundary layer would decrease the aero-mechanical jitter on the turret
geometry. The submerged geometry of 100% boundary layer height has shown in the
flow features to create a stronger oblique shock around the geometry. By analyzing
the pressure fluctuation in the numerical simulation it was observed that the pressure
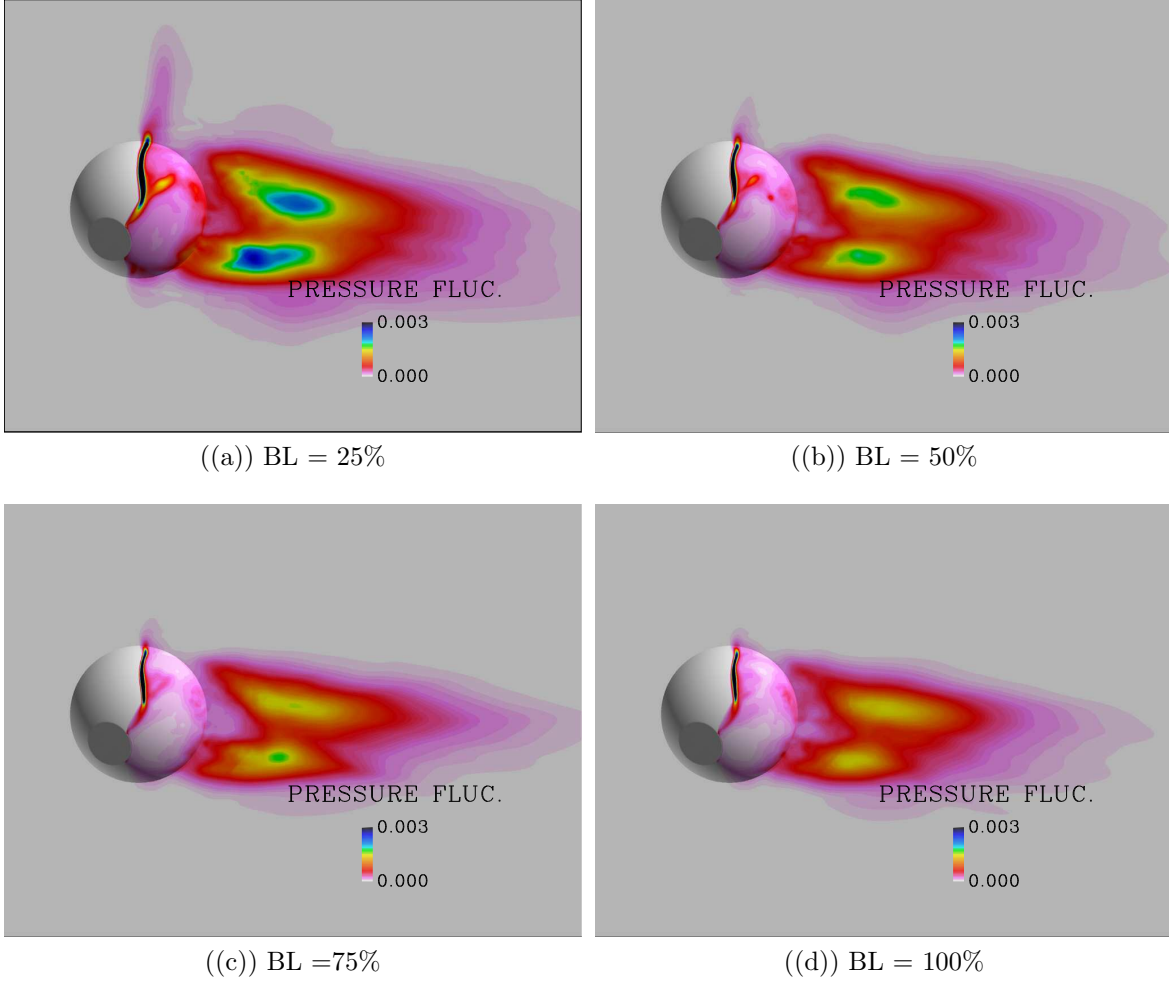
Figure 4.26:   Pressure fluctuations (P'^2) on the surface of the submerged non-symmetrical turret geometry and flat plate for the "high-fast" flight condition

fluctuation around the area of the shock is continuous and produces a significantly smaller pressure fluctuation in the rear of the turret and flat plate.

((a)) BL = 25%   ((b)) BL = 50%

((c)) BL =75%   ((d)) BL = 100%

Figure 4.27:   Pressure fluctuations (P'^2) on the surface of the submerged symmetrical turret geometry and flat plate for the "low-slow" flight condition

73

((a)) BL = 25%

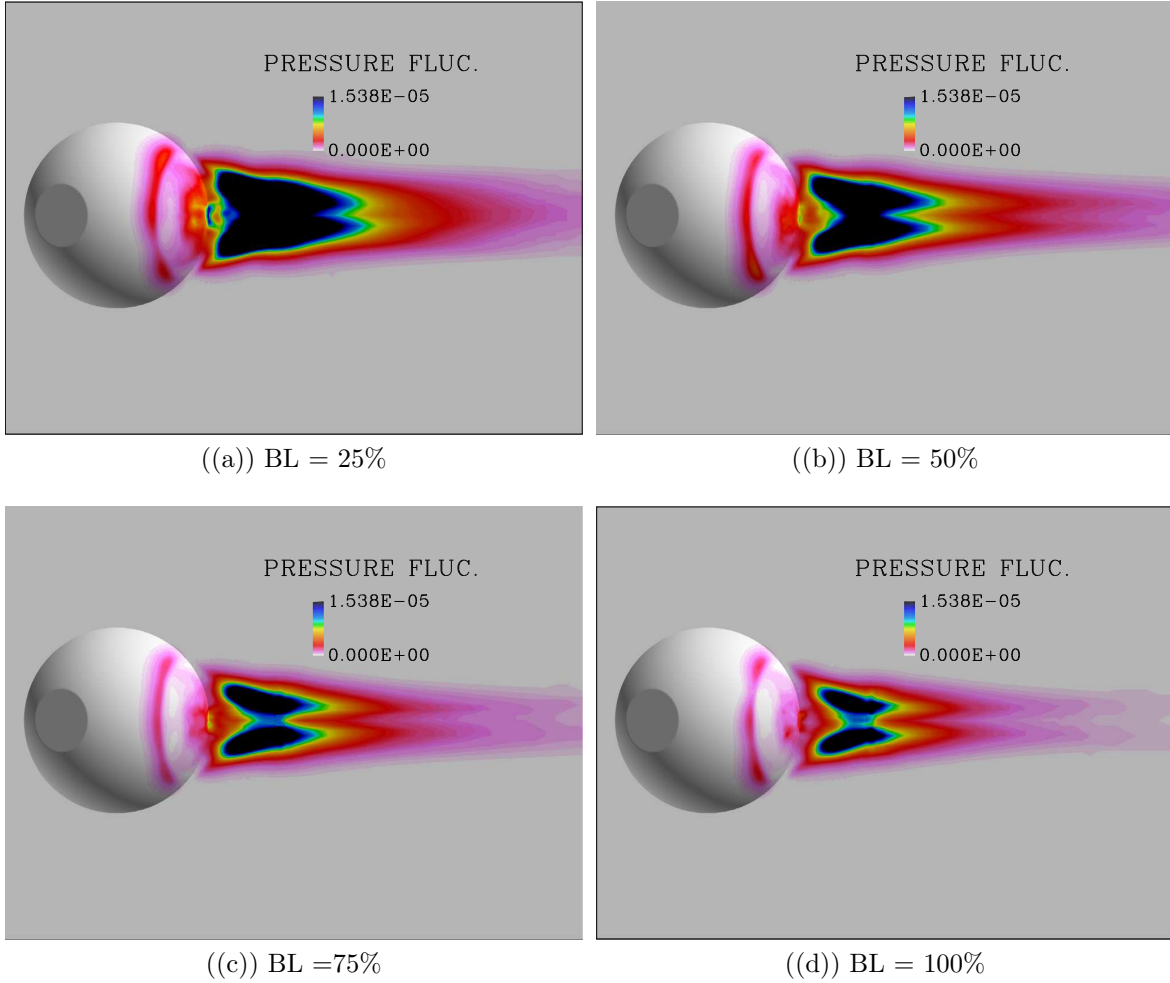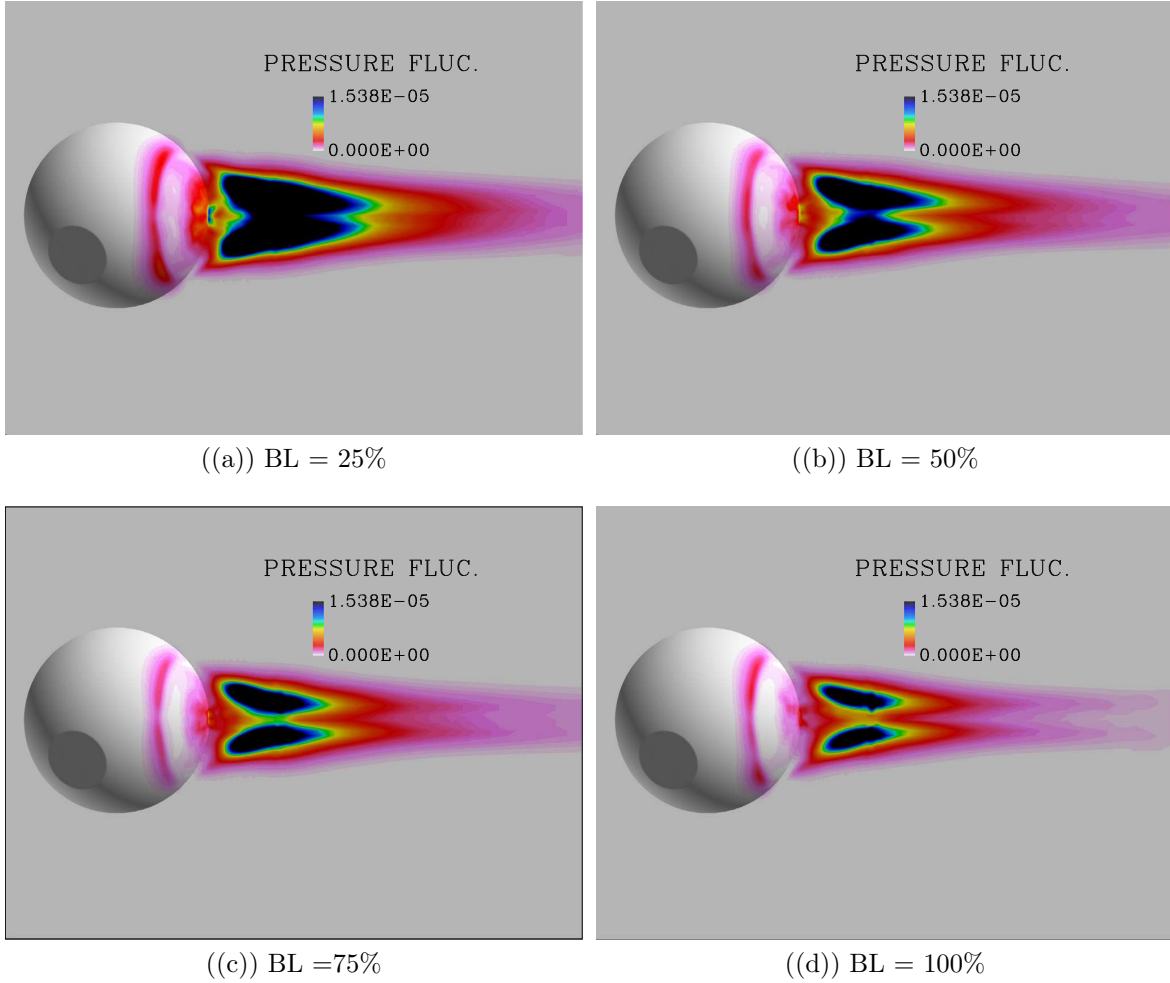((b)) BL = 50%

((c)) BL =75%

((d)) BL = 100%

Figure 4.28: Pressure fluctuations (P'^2) on the surface of the submerged non-symmetrical turret geometry and flat plate for the "low-slow" flight condition

4.4 Density Fluctuation

To further utilize the capability of plotting the contours of fluctuations, the density fluctuation along the symmetry plane of the turret aperture was plotted to analyze how the various boundary layer heights add to the aero-optical jitter. In order to compensate for the fluctuation of density in the beam path, the laser system has a correction mechanism that would adjust the laser beam to correct for variations in index of refraction. Through the use of the density fluctuations modeled, the analysis of where the most density fluctuations occur was visualized. Figure 4.29 is of the fully exposed symmetric turret geometry for the "high-fast" flight condition and Figure 4.30 is of the submerged turret geometry for the same flight condition. The results presented show that the density fluctuation near the turret aperture is the lowest and increases with distance away from the aperture. Note how the expansion at the upper aperture increases the density fluctuation which was observed via flow features in the previous sections. The region of low density fluctuation forms a three-dimensional bubble and increases in size as the boundary layer is increased. On the other hand, the results of the "low-slow" flight condition show that the density fluctuation decreases with distance away from the aperture. For both flight conditions it is observed that the increase in boundary layer height reduces the density fluctuation hence likely creating less aero-optical jitter on the laser beam. The results qualitatively observed in this section were plotted quantitatively to analyze the density fluctuations along the centerline of the beam path, see Section 4.6
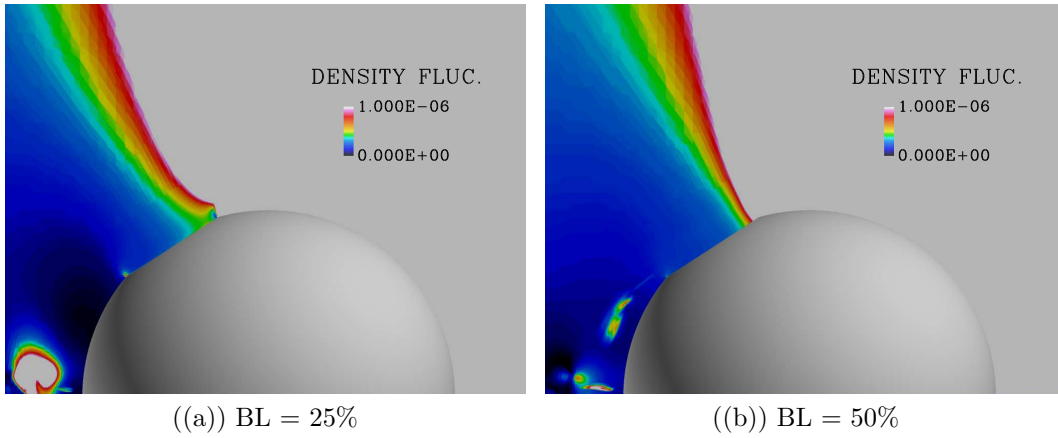
((a)) BL = 25%   ((b)) BL = 50%

Figure 4.29:   Density fluctuation (ρ'^2) on the aperture centerline of the exposed symmetrical turret geometry for the "high-fast" flight condition

((a)) BL = 25%   ((b)) BL = 50%

((c)) BL =75%   ((d)) BL = 100%
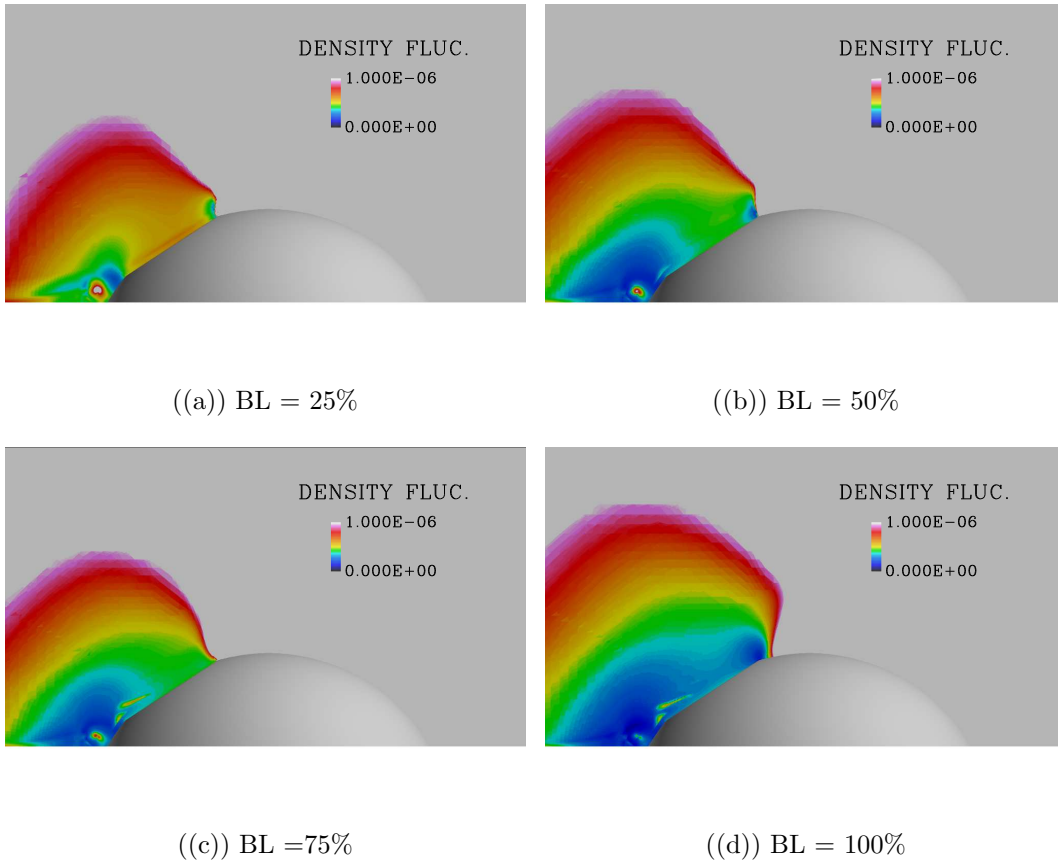
Figure 4.30:   Density fluctuation (ρ'^2) on the aperture centerline of the submerged symmetrical turret geometry for the "high-fast" flight condition

4.5   Frequencies

Visualizing pressure at several locations on the surface of the geometry, some periodicity was noticed in the solutions. To quantify the frequency of the periodicity, the discrete Fourier transform was computed to model the spectral representation of $P(t)$. The oscillation of the pressure data creates the mechanical jitter which is formed due to unsteadiness on the surface pressure. For comparison of multiple boundary layer heights, the frequencies of several cases is plotted on the same plot for comparison. The frequency computed at the centerline in the front part of the turret for the fully exposed turret geometry of the "high-fast" flight condition is shown in Figure 4.31. The results indicate that the 25% and 50% boundary layer height seem to have similar low frequency content at approximately 11 Hz but past that point the increased boundary layer has lower spikes in frequency magnitude.
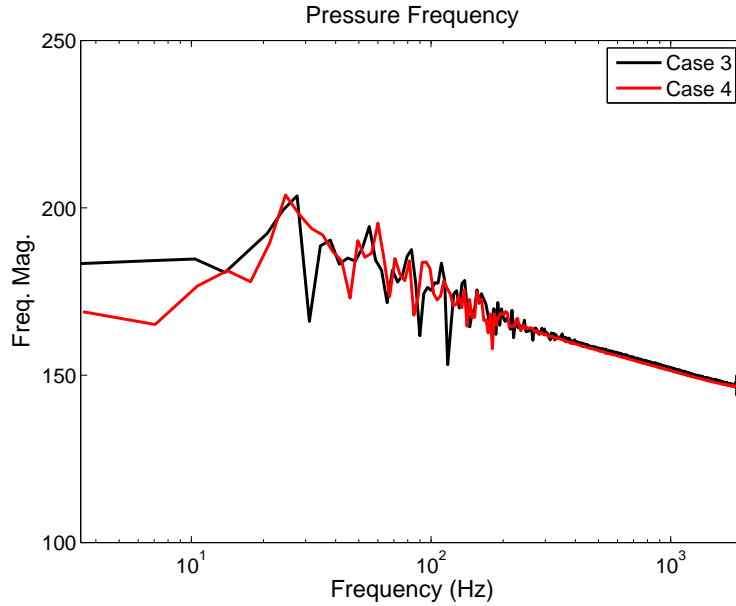

Figure 4.31:   Frequency along the centerline on the front face of the geometry at a distance of 0.14 inches off the flat plate

To further investigate the trend of higher boundary layers decreasing the frequency magnitude and producing slightly higher frequency content, the various imposed boundary layer heights on the symmetrical submerged turret geometry at "high-fast" flight conditions are presented in Figure 4.32. The results show a quantitatively

similar trend as for the fully exposed turret geometry where the frequency magnitude is decreased and the frequency content not as dominant for the lower frequencies

The analysis of the frequency content closer to the wake was examined by computing the frequencies at 90 degrees azimuthal angle to the side of the turret. The results discussed are for the symmetrical submerged turret geometry at "high-fast" flight conditions with four boundary layer heights imposed (25%, 50%, 75%, and 100%). The results shown in Figure 4.33 have a completely different trend than observed on the front section of the turret, presented in Figures 4.31 and 4.32. The trend indicates that a higher boundary layer produces higher frequency content and an increase in frequency magnitude. Also from the plots it can be observed that the the flow is more turbulent on the side of the turret than in the upstream half. Additionally, the results indicate that an increase in boundary layer height will create a higher frequency content and magnitude. The results presented for the 100% boundary layer height (case 20) show that a significant frequency content is observed at approximately 1000 Hz. The cause of unsteady fluctuations being produced on the side of the turret was qualitatively presented in the flow features section by demonstrating that a shock occurrs at that location.

Next, the frequency of the pressure was evaluated for the symmetrical submerged turret geometry at the "low-slow" flight condition with four imposed boundary layer heights. The results, presented in Figure 4.34 show that the pressure frequency content is significantly higher than for the results of the "high-fast" simulation. The peak frequency occurs at approximately 17 Hz, which is about 50% higher than the 11 Hz observed in the transonic case. An increase in boundary layer also presents a reduction in the frequency content as well as the magnitude of the frequency. The anticipated results agree with the flow features, pressure fluctuations, and density fluctuations observed in the sections discussed above. When analyzing the frequencies of pressure on the side of the turret dome at 90 degrees, shown in Figure 4.35, no correlation between boundary layer heights was observed, meaning that although the
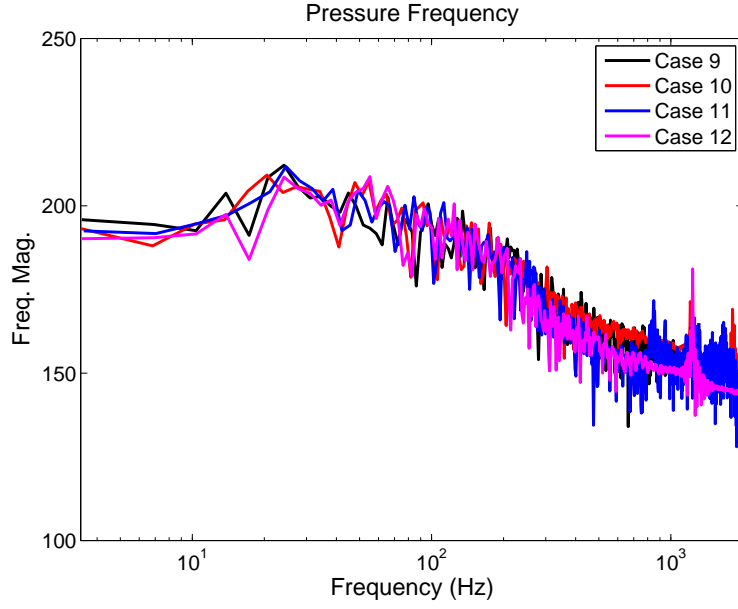
Figure 4.32: Frequency of the pressure on the centerline in the front half of the turret geometry
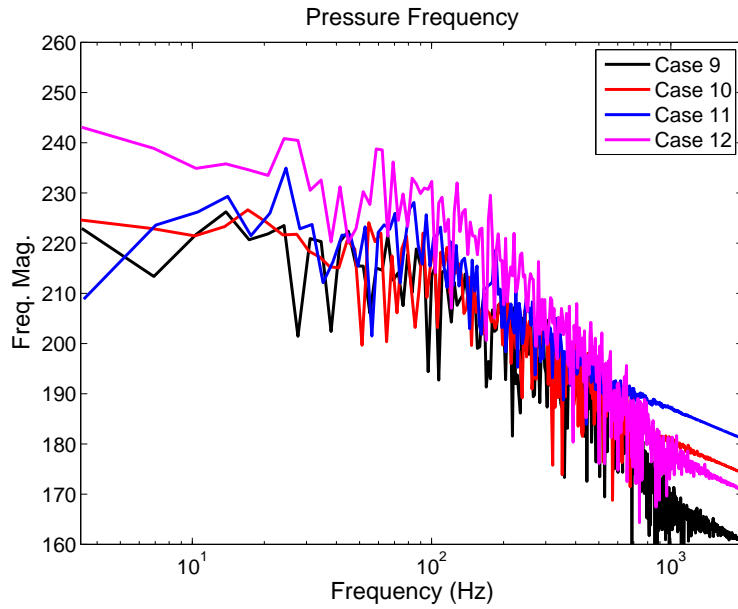

Figure 4.33: Frequency of the pressure at 90 degrees of the turret geometry

frequency is still present, an increase in boundary layer produces completely different frequencies encountered by the geometry.
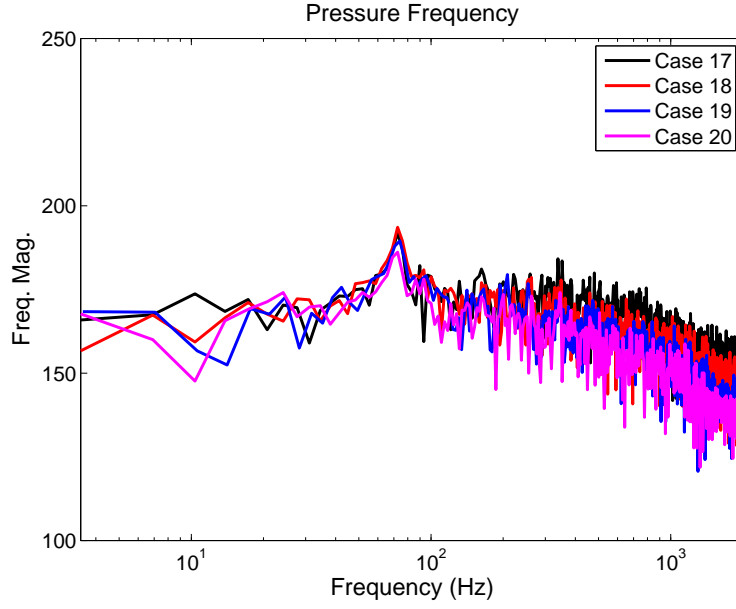
Figure 4.34:   Frequency of the pressure on the centerline in the front half of the turret geometry
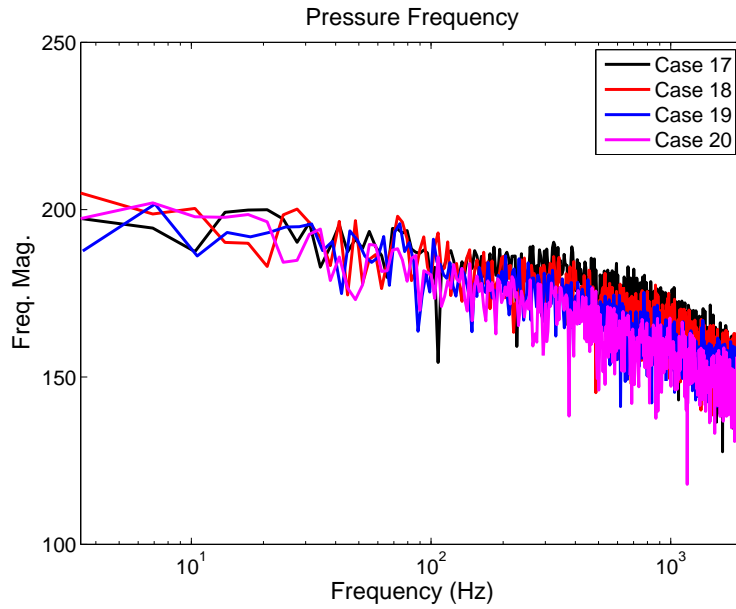

Figure 4.35:   Frequency of the pressure at 90 degrees of the turret geometry

The results of the frequency computations indicate that the low frequency content is mainly present in the front half of the turret. As the frequency is extracted towards the rear of the geometry, the high frequency content starts to increase. The

high frequency content observed towards the wake of the turret is due to the recirculation region which contains small turbulent structures. Further analysis reveald that the effect of the boundary layer has minimal effect on the frequency content in the front half of the geometry but results in a higher magnitude of the frequency as the pressure is extracted towards the wake. The comparison between the "high-fast" and "low-slow" flight conditions showed that the lower frequency content of the high subsonic flight condition spikes at 11 Hz compared to 17 Hz of the low subsonic simulation. To obtain a more accurate representation of the frequency content present in the flowfield, the simulations would need to be ran for a longer period of time. For this study the number of iterations was 50,000 which is probably insufficient time to resolve the solution.

4.6 Fluctuations

When a colliminated laser propagates through a turbulent compressible flow, the waves become aberrated and the image becomes blurred. The aberration is caused by the variations in index of refraction which depends on the density, ρ. The density fluctuations which cause the aberrations can be caused by compressible shear layers, wakes, and turbulent boundary layers. To study the density fluctuations occurring in the laser beam, the OVERFLOW simulations conducted by generating a "q.avg" file which consists of the time averaged density, momentum, total energy, and ratio of specific heat. In addition to the time averaged values the file collected the perturbation of density, velocity, and pressure (ρ', u', v,' w', P') at each grid point. The results of the density fluctuation are plotted vs. distance along the centerline normal to the aperture, see Fig 3.12. To investigate how the boundary layer height affects the density fluctuation, the cases are placed into eight groups divided by geometry type and varying boundary layer, see Fig 4.1.

The results of the density fluctuation for the "high-fast" flight condition are shown in Figure 4.36. The top two figures are of the exposed turret geometry and the bottom two plots are of the submerged turret. The results reveal that the density

fluctuations increase versus distance away from the aperture surface. The exposed turret geometry encounters a lower density fluctuation than the ten inch submerged geometry. By studying the boundary layer height and the impact it has on the density fluctuation, it is observed that the density fluctuation can be reduced when increasing the boundary layer. The boundary layer height seems to linearly decrease the density fluctuation as seen in all plots. Consequently, the smallest density fluctuation seems to occur for the fully exposed turret at a boundary layer height of 50% and azimuthal angle of 45 degrees. Next, the density fluctuations for the "low-slow" flight condition were evaluated which, unlike the results of the "high-fast" simulation, has a decrease in density variation versus distance away from the wall. The density fluctuation of the lower boundary layers imposed does seem to decay faster than the higher imposed boundary layers and the results of the submerged geometry have a density fluctuation lower by approximately two orders of magnitude. In comparison the "high-fast" flight condition, the results present similar trends, where an increase in boundary layer height can have a significant reduction in density fluctuation for some of the cases. Consequently, the laser beam would best propagate at the submerged geometry with an azimuthal angle of zero and boundary layer height of 100%. Overall the density fluctuations encountered by the low subsonic flight conditions are significantly less than for the high subsonic flight conditions. As the Mach number increases the compressibility effects start to occur which causes higher density gradients in the flow field that in return cause significantly higher density fluctuations.

The two types of jitter are aero-optical jitter and mechanical jitter, when both types of jitter occur on aircraft platforms, the laser beam quality can be reduced significantly. Aero-optical jitter is caused by density fluctuations in the line-of-sight, of the beam, as discussed above and mechanical jitter is created from unsteady pressure and velocity fluctuations that induce unsteady forcing on the geometry. The vibration excites the jitter disturbances in the optics and further adds to the aberration of the laser beam. Plots of the pressure fluctuation along the vertical and horizontal
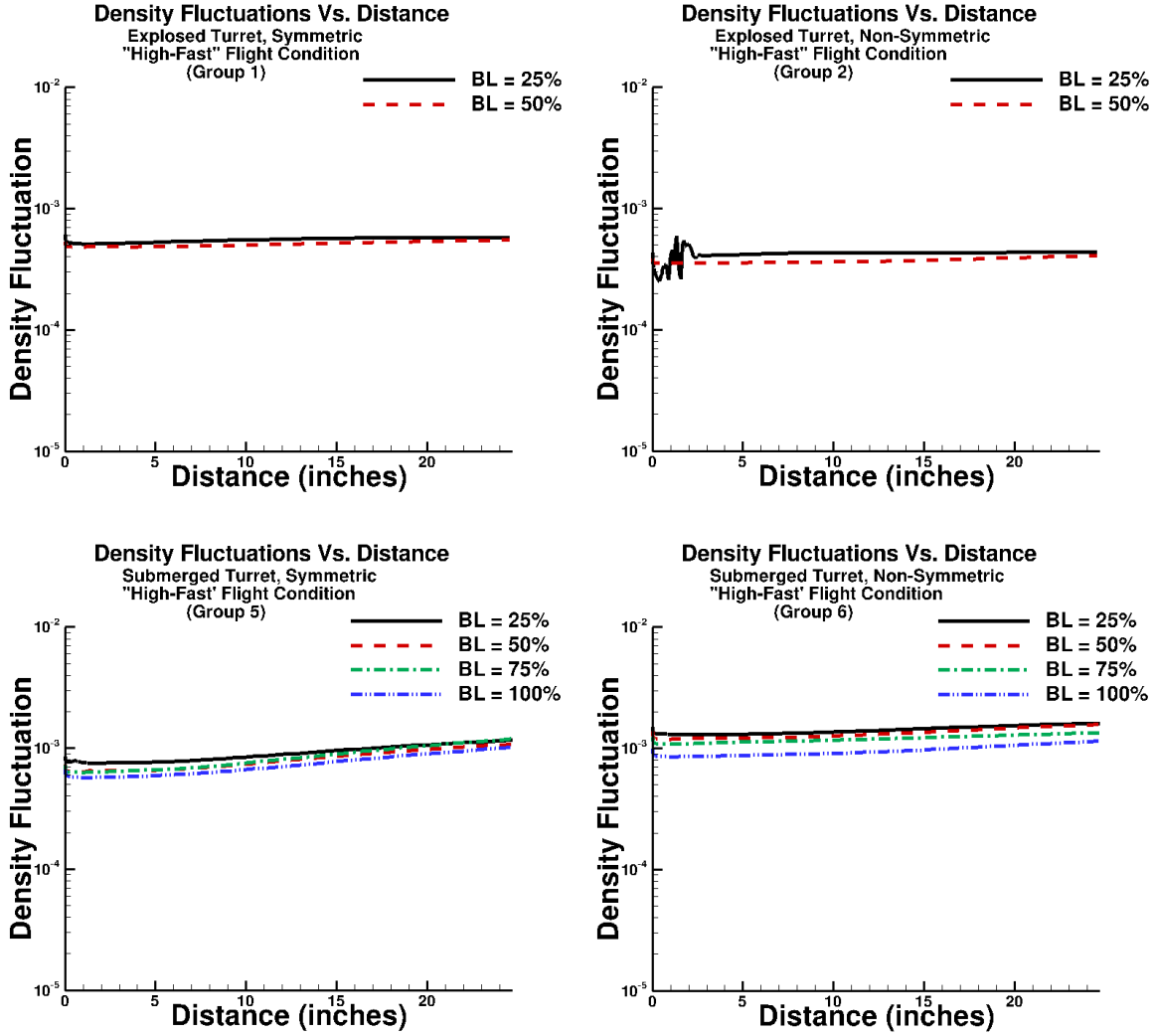
Figure 4.36:   Density fluctuation (ρ') for all "high-fast" cases

centerlines, see Figure 3.12 are examined to investigate the aero-mechanical jitter introduced due to unsteady pressure.

The results presented in Figure 4.38 are of the pressure fluctuations plotted along the horizontal centerline of the aperture for the "high-fast" flight condition with the fully exposed geometry in the top row and submerged geometry in the bottom. The left column is for the axisymmetric solution and the right column presents the non-symmetric geometry. As expected the results show spikes in pressure fluctuations along the aperture edges. This can be seen for in all plots, where the fluctuations
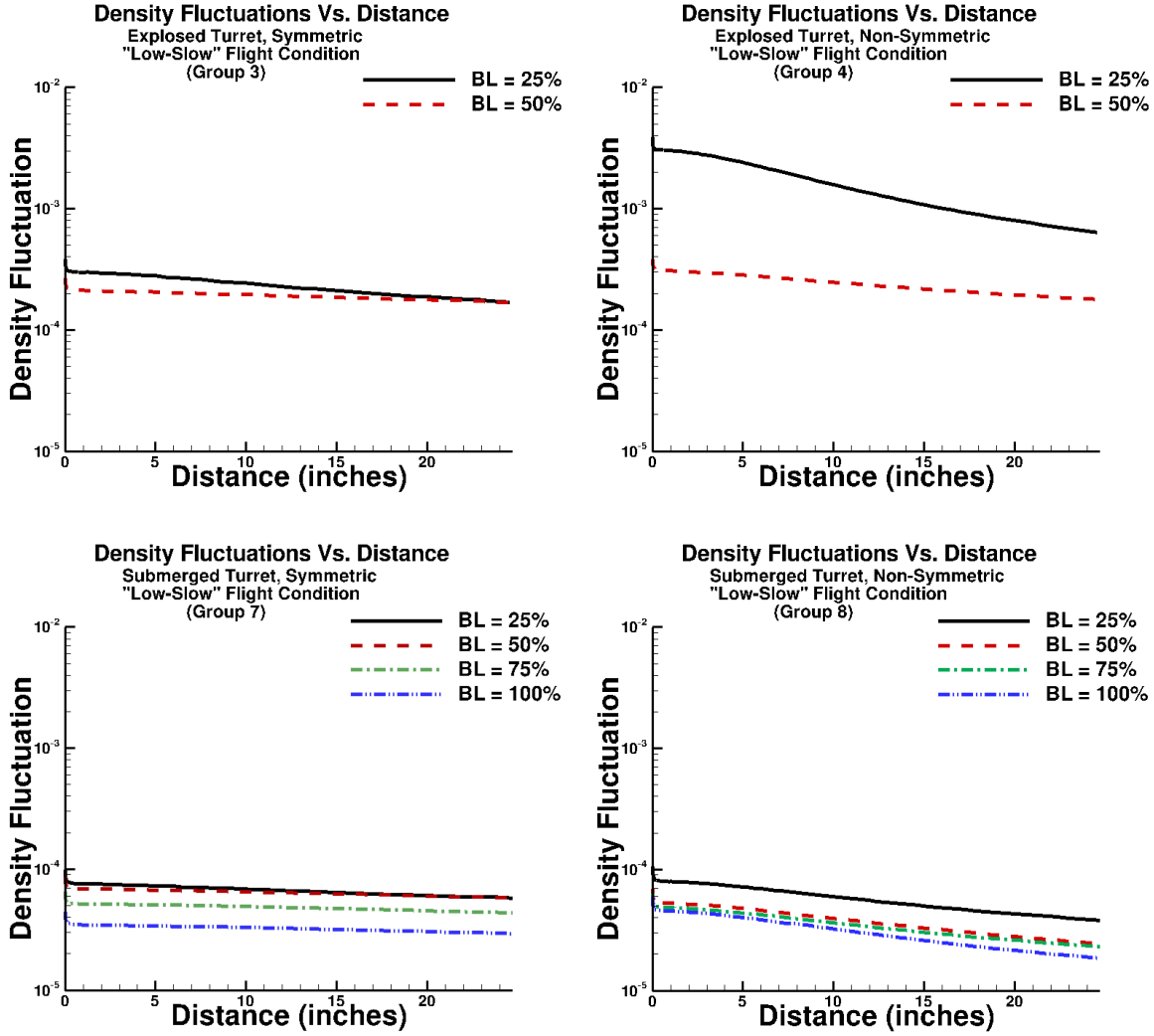
Figure 4.37: Density fluctuation (ρ') for all "low-slow" cases

along the edges are two orders of magnitude higher than along the aperture for some of the cases. The axisymmetric cases reveal that the pressure fluctuations for the fully exposed geometry spike on the left aperture side and for the submerged geometry spike on the right side which is closer to the wake. The comparison between the symmerical vs. non-symmetrical geometries reveals that for aperture at an azimuthal angle of 45 degrees, the aperture is closer to the wake of the turret and has an increase in pressure fluctuations by about an order of magnitude. Additionally, the submerged case encounters higher pressure fluctuations and would ultimately create the most aero-mechanical jitter, especially at the non-symmetrical orientation. In

Figure 4.39 the pressure fluctuations along the horizontal centerline are plotted for the low subsonic flight condition. The results show similar trends as observed for the high speed flight conditions with a pressure fluctuation increase towards the wake of the turret, significantly higher pressure fluctuations for lower boundary layers, and pressure fluctuation spikes around aperture edges. Overall the results seem to be lower by an order of magnitude than for the high speed simulations.
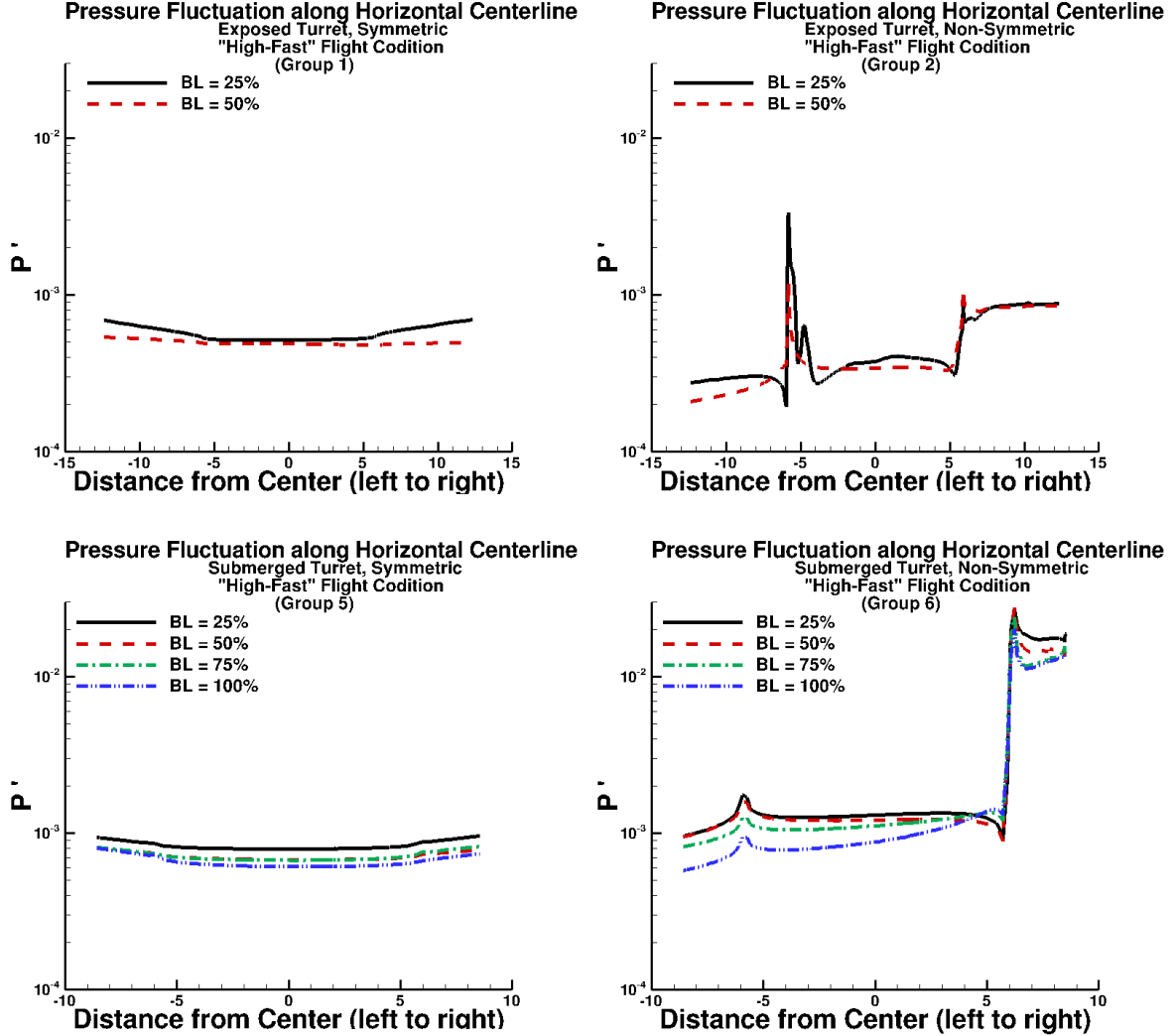

Figure 4.38:   Pressure fluctuation (P') along horizontal for all "high-fast" cases

To further analyze the pressure fluctuations occurring around the turret aperture, values of pressure fluctuations were examined along the vertical centerline of the aperture, see Fig 3.12. The results are plotted from the top of the aperture to the
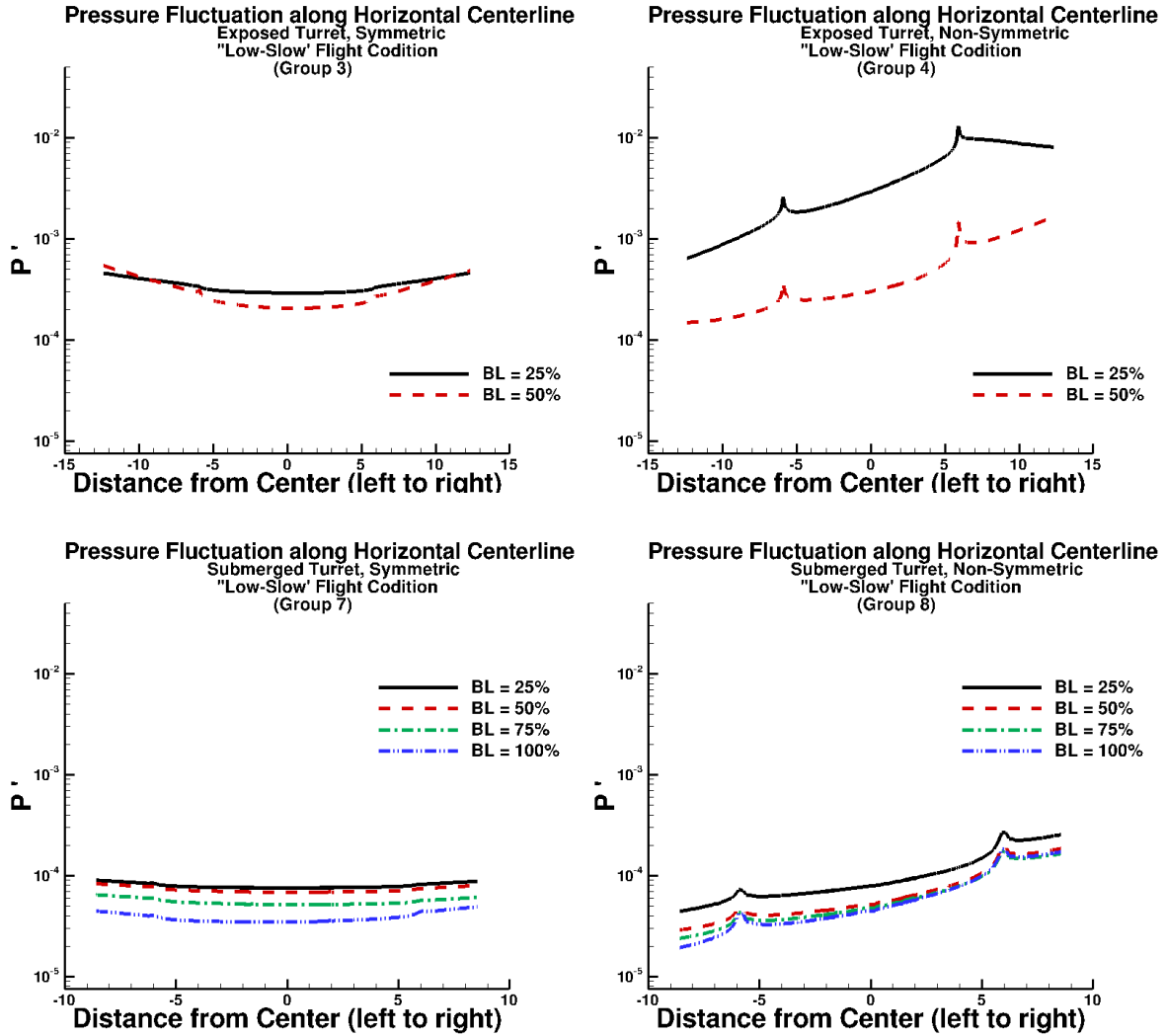
Figure 4.39:   Pressure fluctuation (P') along horizontal for all "low-slow" cases

bottom, hence the first value on x-axis is the top point slightly above the aperture. For the "high-fast" flight conditions, the results, presented in Figure 4.40 show that the pressure fluctuations drastically increases around the upper edge of the aperture. The cause is an expansion forming at that location and the creation of a shear layer that contributes to the pressure fluctuations. It can also be seen that the pressure fluctuations encountered by the submerged geometry are higher than for the exposed geometry, again this is only examining the fluctuations along the centerline of the aperture alone. Hence, the submerged geometry will be encountering more of the viscous forces creating higher pressure fluctuations. The results of the "low-slow" flight

condition show the same trends where the pressure fluctuations occur highest at the upper edge of the aperture, and then decrease as it gets to the bottom edge. The submerged geometry has a significantly lower density fluctuation than those encountered by the fully exposed geometry. Overall, the main trend to be observed between both flight conditions for all geometries is that the pressure fluctuations decrease as the boundary layer is increased, hence the lowest encountered pressure fluctuation between all the cases would be by Case 20 which is the submerged geometry, at "low-slow" flight conditions, azimuthal angle of zero degrees, and 100% boundary layer height.
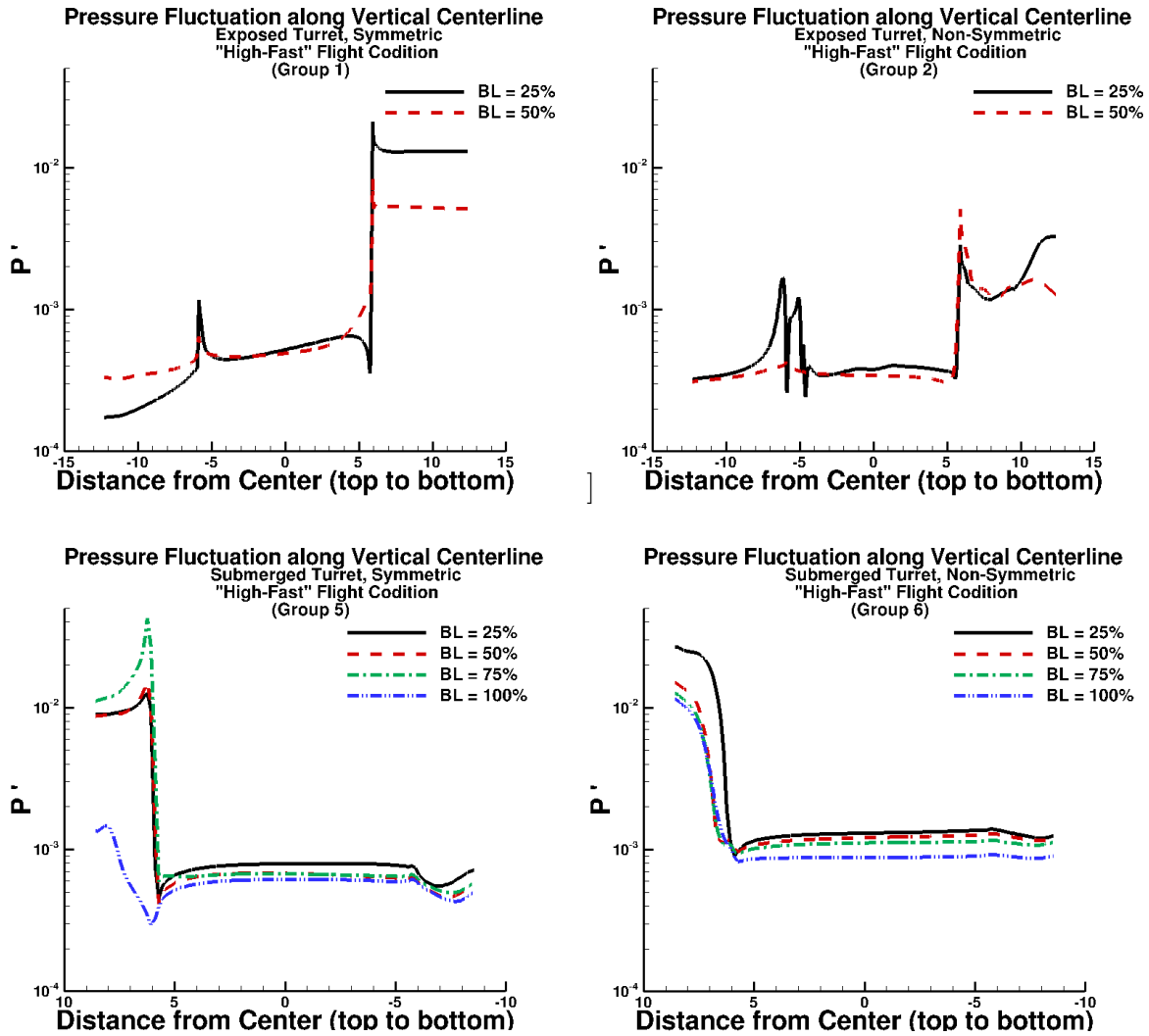
Figure 4.40: Pressure fluctuation (P') along vertical centerline for all "high-fast" cases
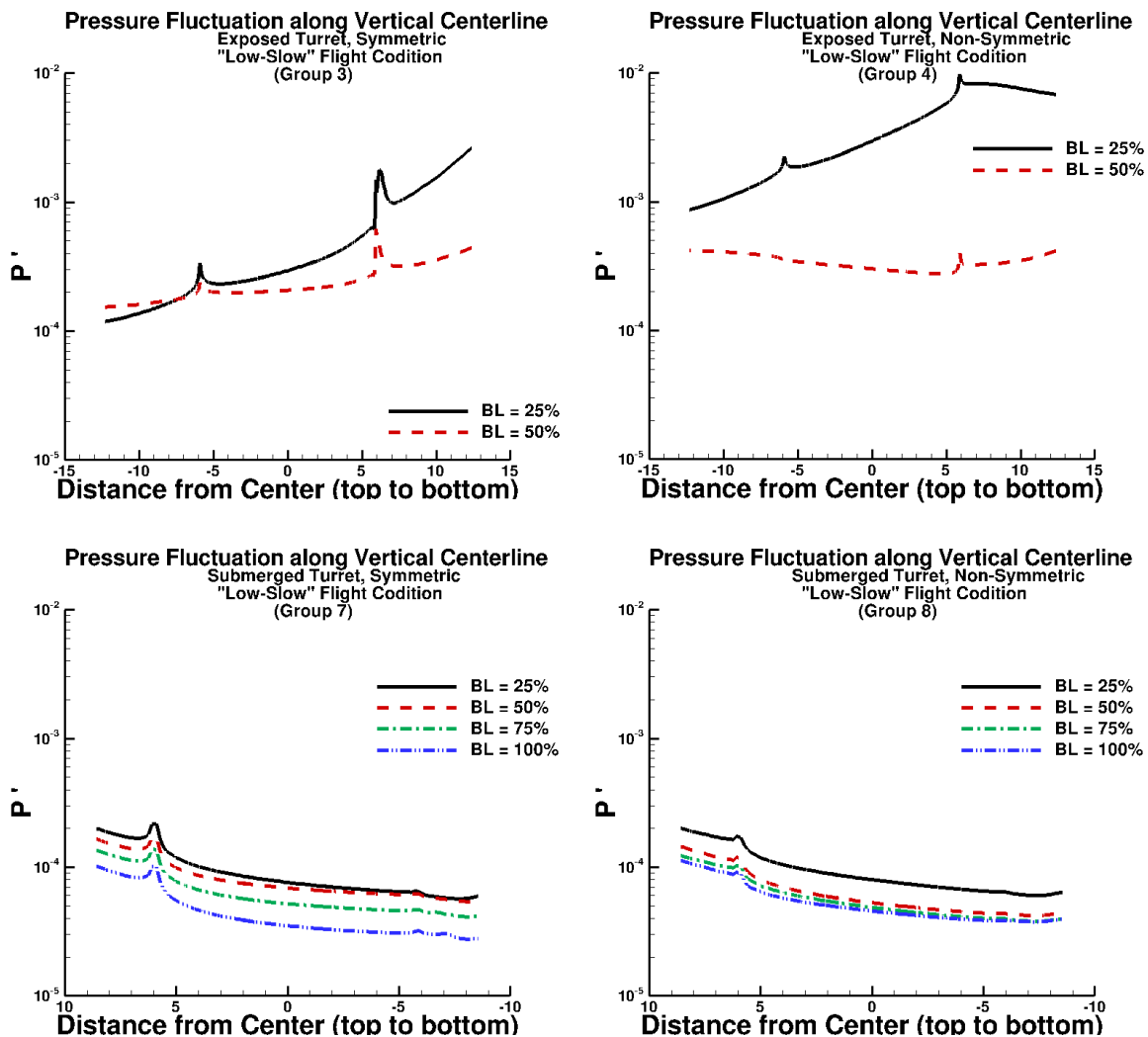
Figure 4.41: Pressure fluctuation (P') along vertical centerline for all "low-slow" cases

4.7   Force/Moment Calculations

One of many capabilities implemented into the OVERFLOW code is to compute forces and moments on a body over time. In order to apply the capability to the study performed in this thesis, the minimum, maximum, and average values of the time study for the forces and moments are plotted. The fluctuation of the net force on the turret body will lead to a fluctuation in the stresses on the body that can be correlated to the aeromechanical jitter. Although the forces induced on the geometry provide an insight to the potentially encountered jitter on the body, the investigation of the moments provide additional information as to the twist endured by the geometry. To actually obtain the real-time aero-mechanical jitter observed by the geometry, a fluid-structure analysis is needed. For the study conducted in thsi thesis the center of moments is located at the origin of the computational mesh which is at the center point of the turret circle. The forces are broken down into the x, y, and z directions and moments are expressed in it's components of moment about the x-, y-, and z-axis. The orientation of the axis for which the forces and moments are computed about are presented in Fig 4.42.
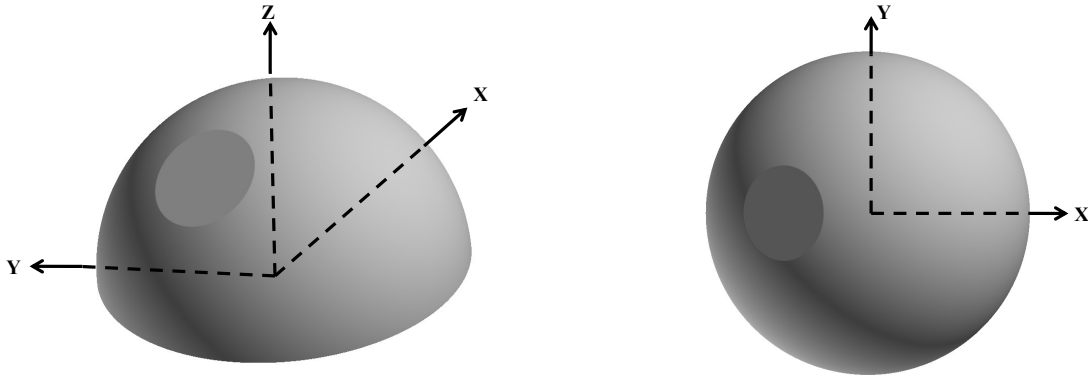
Figure 4.42:   Axis orientation for turret geometry

The forces and moments presented in this section employ identical axes for all computational simulations. The plots present the minimum and maximum values through the horizontal bars and the average value by the circle on the horizontal

line. The results are divided into the flight conditions, exposed vs. submerged turret geometries, and colored black and blue for the symmetrical and non-symmetrical geometries, respectively. The results of the x-force are presented in Figure 4.43 for both flight conditions of the submerged and fully exposed turret geometries. It should be noted that the x-force corresponds to the drag coefficient, and shows that an increase in boundary layer reduces the total of the x-force encountered for all cases. The exposed turret geometry encounters a higher drag than the submerged case but the variation between the minimum and maximum value is significantly higher. Due to the larger surface area, it is expected that the exposed turret encounters a higher drag and the reason for the submerged case to have higher fluctuation between the minimum and maximum point is due to the flow interacting with the flat plate, as presented in the flow features. For the "low-slow" flight condition the same trend is observed where an increase in boundary layer decreases the drag on the geometry which is observed to be due to the flow remaining attached further downstream. For the low speed simulations, the fluctuation between minimum and maximum point is significantly lower than observed for the "high-fast" flight condition. Overall, the total x-force on the low-speed case is lower than for the transonic case due to the shocks and expansions encountered by the transonic case lead to an earlier separation and a larger wake formed in the rear.

By analyzing the total y-force encountered by the turret geometry, also referred to as "side force", see Figure 4.44, it was observed for both flight conditions that the symmetrical case had an average side force of approximately zero, which is expected that opposite forces would cancel each other out for a symmetrical geometry. The non-symmetrical case had a positive side force due to the aperture orientation. For the "high-fast" flight conditions the side force of the fully exposed turret geometry does not vary nearly as much as for the submerged cases. Further analysis shows that the exposed turret geometry overall experienced a lower side force on average than the non-symmetric submerged geometry; this phenomenon was observed in the
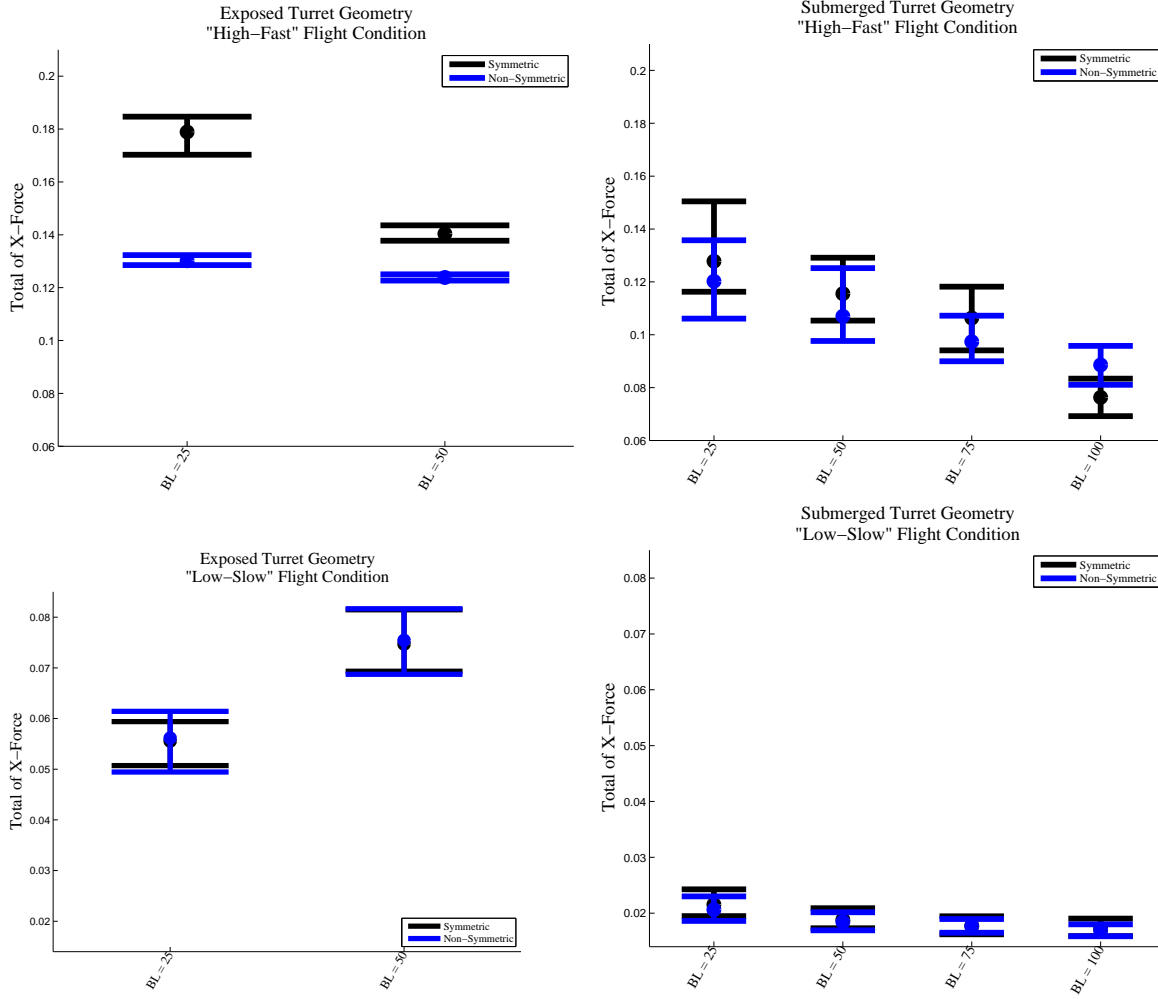
Figure 4.43:   Total forces along x-direction for all cases (drag)

flow structures where the shear layer interaction with the flat plate lead to a highly
unsteady wake.

Although the total x-force and y-force computations create conclusive evidence
to which cases provide the highest forces and fluctuations in the numerical simulations,
the analysis was taken a step further by analyzing the moments about the x-axis and
z-axis. The analysis of the moment about the x- and z-axis can provide an insight
to where the forces mainly are applied. If the forces are applied along the centerline
of the turret, the results will indicate a small moment about the x- and z-axis and if
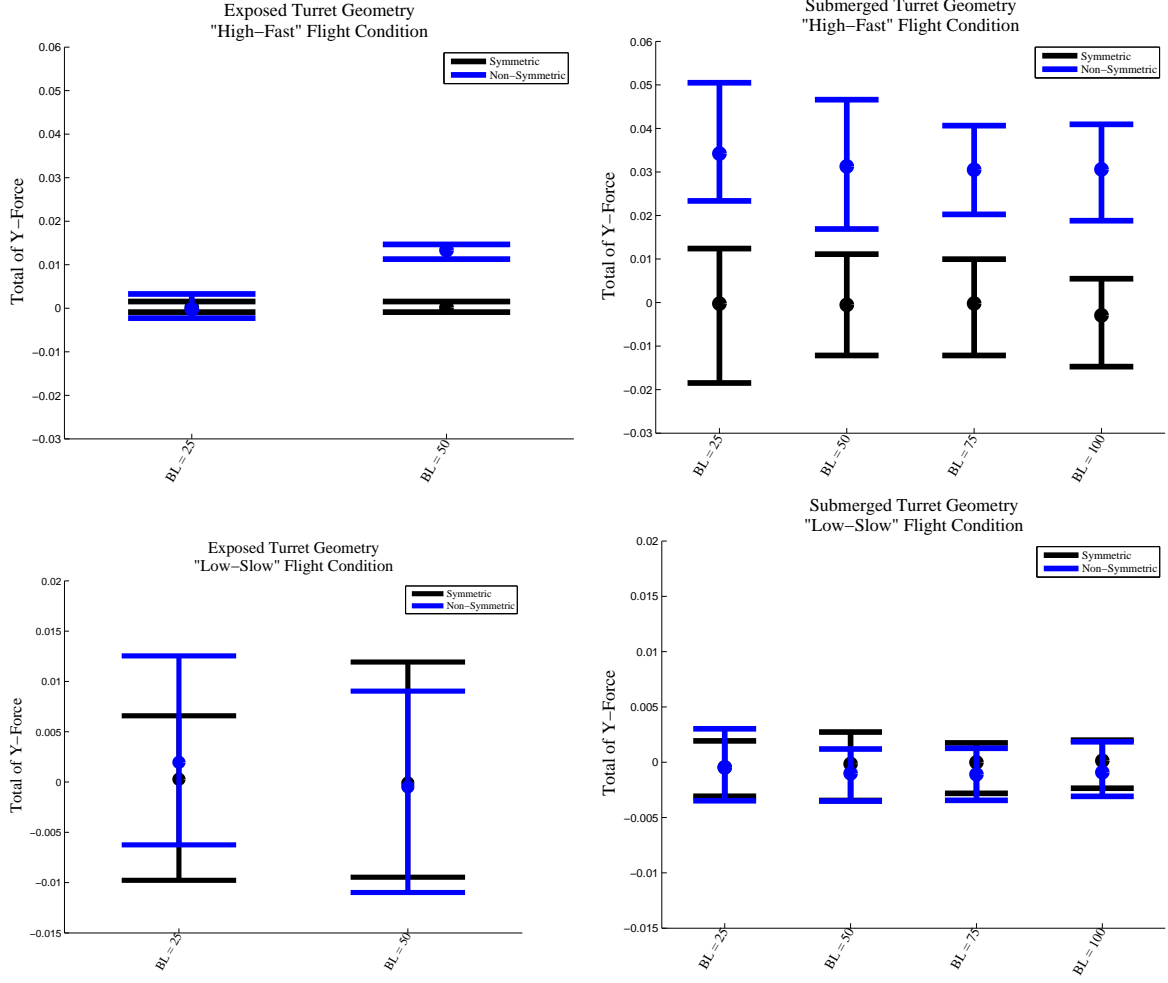
Figure 4.44:   Total forces along y-direction for all cases (side force)

the fluctuations of the forces transition from one side of the turret to the other, the moments will provide an insight.

The results presented in Figure 4.45 are of the moments about the z-axis. The results show that the non-symmetrical geometries create a non-symmetric separation region that creates a moment about the z-axis. It is also observed that an increase in boundary layer height reduces the z-moment created about the axis due to the delayed separation. Additionally, the fluctuations between the minimum and maximum values for the moment about the z-axis are the same as encountered for both symmetrical and non-symmetrical turret geometries.
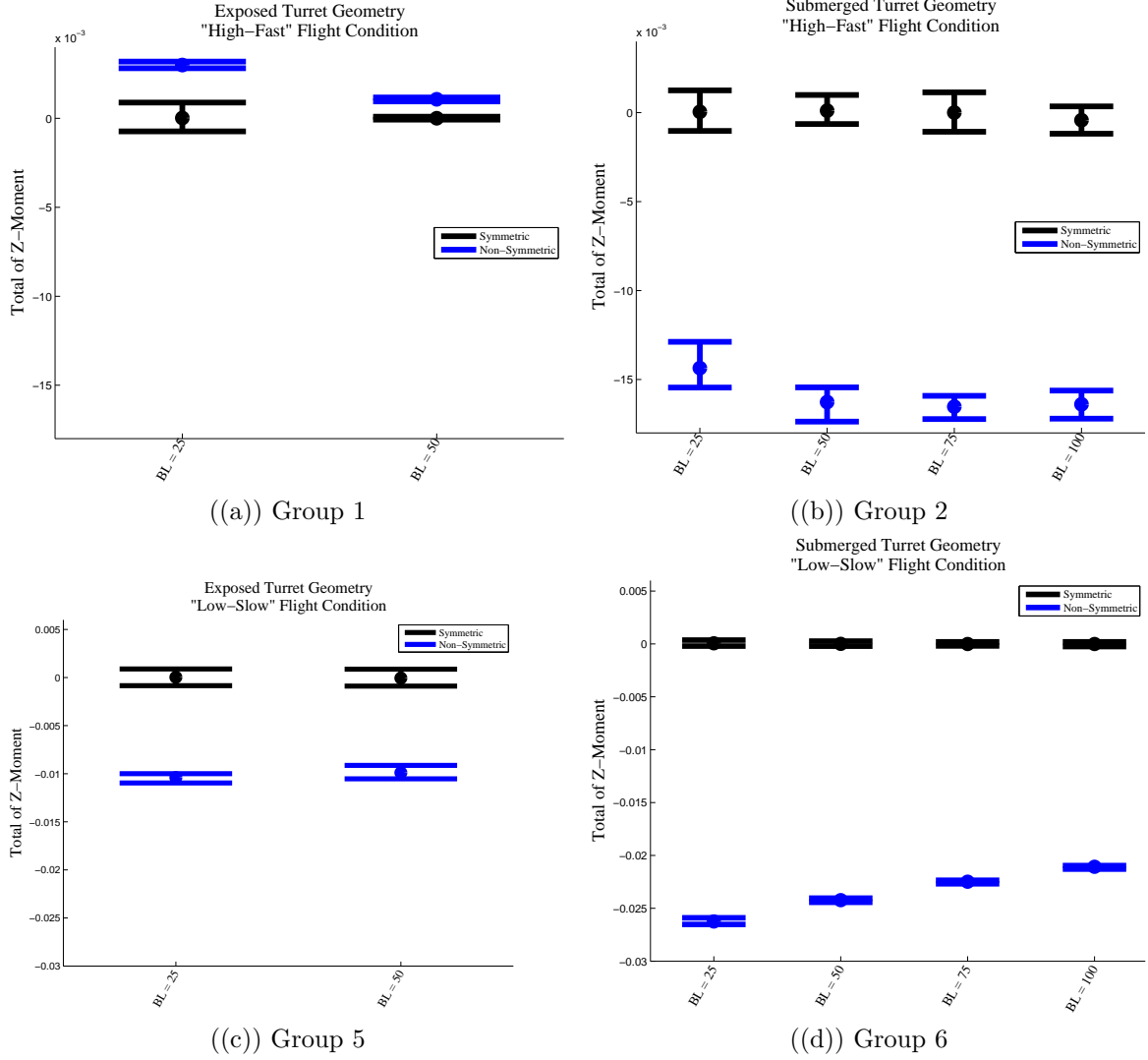
Figure 4.45: Total moments along z-direction

To further investigate the side force created by the flow over the turret aperture, the moment about the x-axis was taken to analyze the fluctuations of the total y-force. The results show that the moment about the x-axis is insignificant compared to the moment created by the submerged cases for both flight conditions. The moments were examined as an additional method used to show that the interaction between the flat plate and the turret geometry lead to a higher force fluctuations and possibly higher aero-mechanical jitter because the flow tries to reattach.
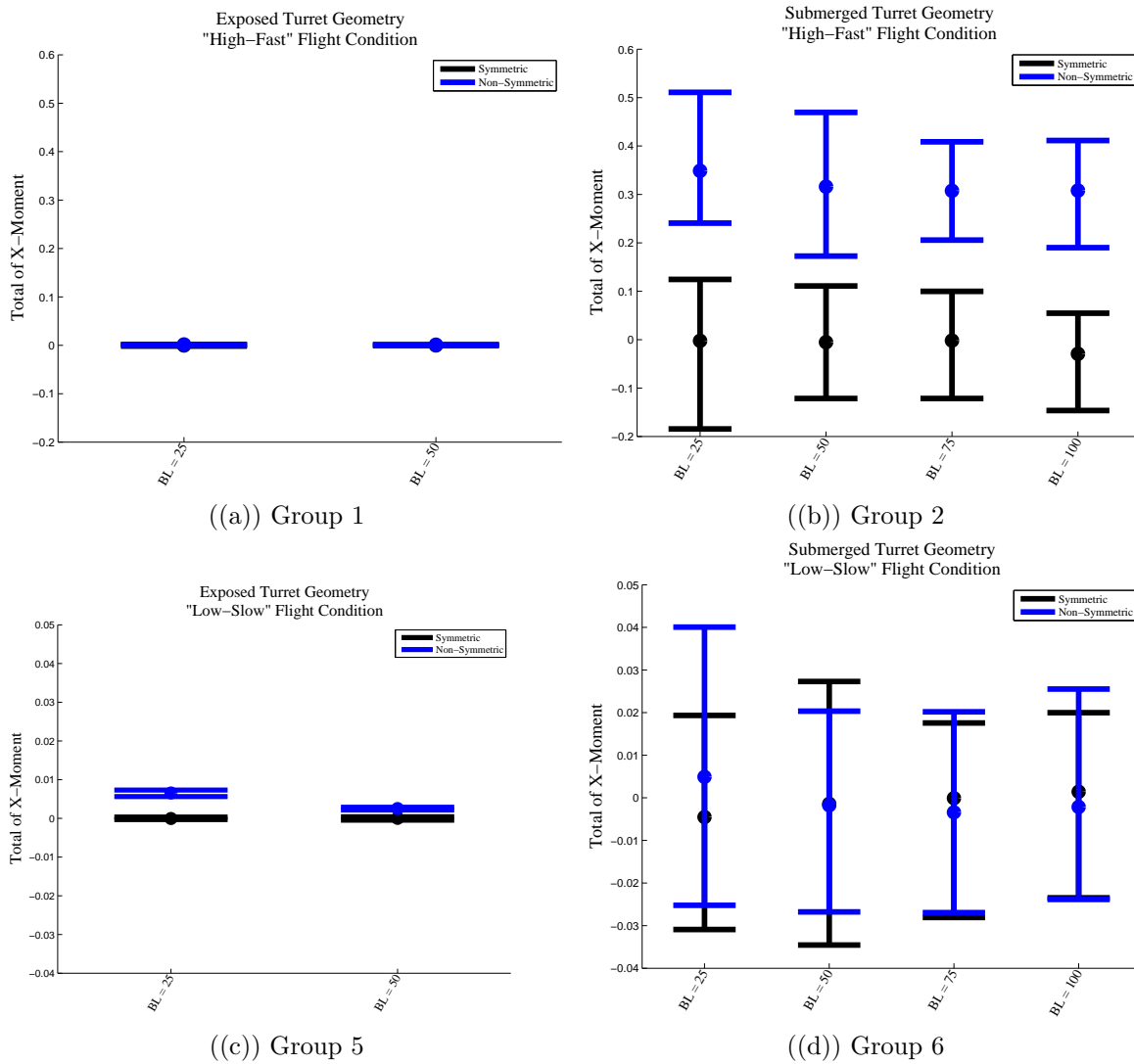
((a)) Group 1

((b)) Group 2

((c)) Group 5

((d)) Group 6

Figure 4.46:   Total moments along x-direction

4.8   Grid Convergence Study

As the grid spacing is reduced, the simulation results become more insensitive to the grid which is an important aspect to investigate. The primary method to obtain accuracy is to verify the calculation is to employ grid convergence. The computational domain used for the simulations was refined and coarsened to produce three computational meshes which consisted of 18 million (coarse), 34 million (medium), and 83 million (fine) cells. The fully exposed symmetric geometry with "high-fast" flight conditions was ran on all three grids for comparison. The results were analyzed via modeling the pressure coefficient (c_p) along the turret centerline from the front to the back as shown in Figure 4.47. The pressure coefficient plot has two significant spikes at $\theta = 40°$ and $70°$ for the bottom lip and top lip of the aperture, respectively. The significant drop in pressure expected along the edges of the aperture is due to the flow expanding as it propagates over the edge of the aperture. The results of the three computational meshes of pressure coefficient (c_p) vs. θ are presented in Figure 4.47. The results show that the three computational grids model the same pressure coefficient

The results presented show that all three grids capture the same pressure coefficient on the front half of the turret until approximately $\theta = 77°$. The three computations start to deviate where the fine mesh captures a higher pressure coefficient in the wake of the turret vs. the coarse grid with a significantly lower value of c_p. The simulations deviate from one another in the wake of the turret because that is the region of the separation. A finer grid will capture more of the flow structures than a coarse grid and hence produce a higher pressure coefficient value. Additionally, it can be observed that the fine mesh and medium refined grid model show the same trend and only slightly deviate from one another, while the coarse mesh captures a significantly lower value of c_p.

From the comparison it can be concluded that the grid convergence has not fully been reached in the wake of the turret geometry but has converged in the front

half of the turret around the aperture. Since the focus of this thesis is to analyze the aerodynamics around the laser beam, the medium refined mesh was chosen because it employs a converged grid and is computationally inexpensive compared to the fine mesh of 83 million cells.
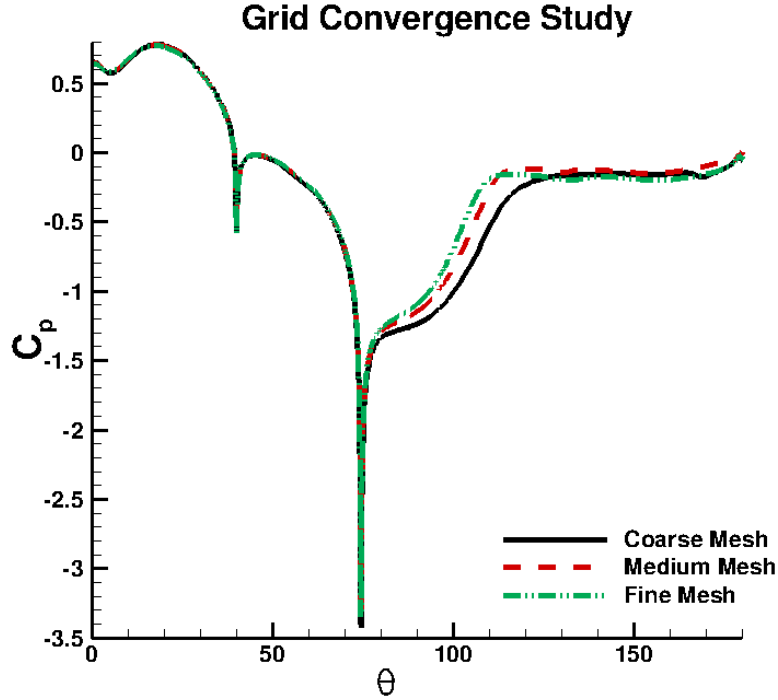

Figure 4.47:   Comparison between coarse, medium, and fine mesh for grid convergence study

4.9   Convergence

The L2 norm of the solution ∂Q is referred to as the residual of the solution and represents the change in the solution over an iteration averaged of all cells in the computational domain. The residuals are presented to show the iterative convergence of the solution, as the algorithm iterates the solution, the simulation results approach a fixed value, hence residuals drop off. For the case of unsteady flows, the iterative convergence is applied to the iterations over a time step. In the simulations conducted for this thesis, all computations were run with three Newton sub-iterations. The

residuals of all the cases were examined to ensure convergence and that the residuals have leveled off over time. The L2 residuals are displayed as its log values $(log(L2))$ to show the order of magnitude of the change in the solution. Quantitatively all solutions demonstrated the same level of convergence, the results of the each one of the geometries is presented in Figure 4.48 with grid 1 as turret o-grid, grid 2 the turret cap grid, grid 3 as the aperture grid, grid 4 being the aperture cap grid, and grid 5 the background grid of the entire computational domain.

The results show that grids 2, 3, and 4 are lower by three orders of magnitude compared to grids 1 and 5, with grid 1 being the turret o-grid and grid 5 the background grid. The two grids, interpolate the data of each other for the wake of the turret and hence have to capture unsteadiness with significant gradients. The major concern is shown in Cases 1 and 9 which are for the "high-fast" flight condition which shows that the unsteady shear layer formed over the dome of the geometry causes an increase in the residuals. Because the work is mainly concerned with the flow field in the front half of the turret, the residual increase in the wake is fairly misleading and should not result in error of the flowfield around the laser beam.
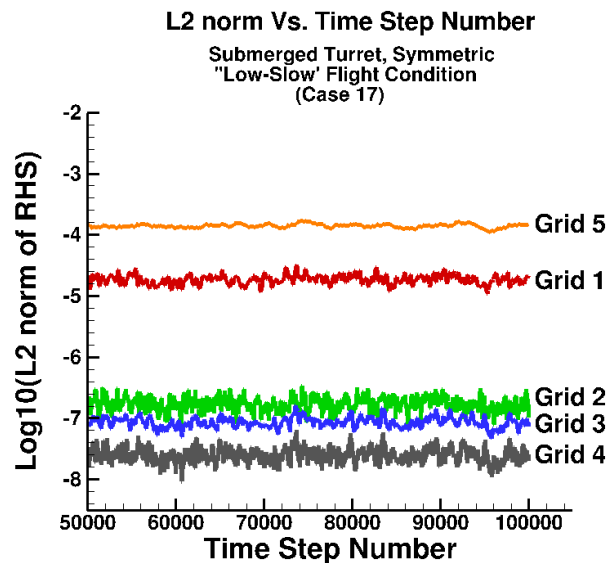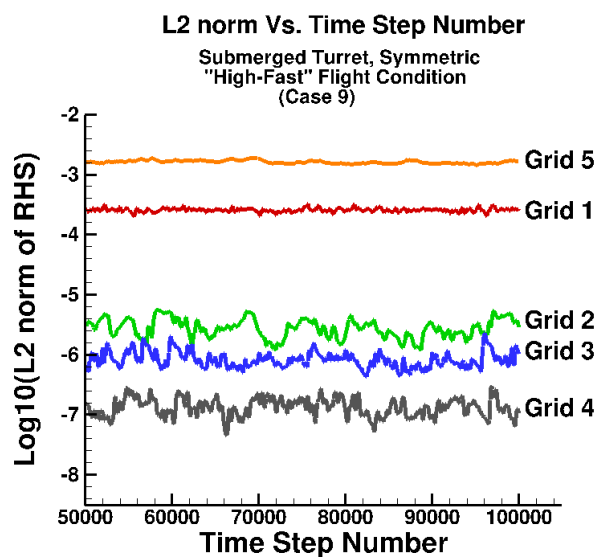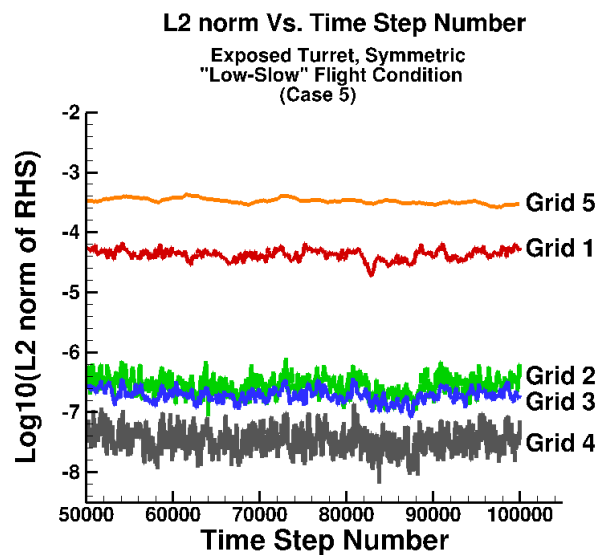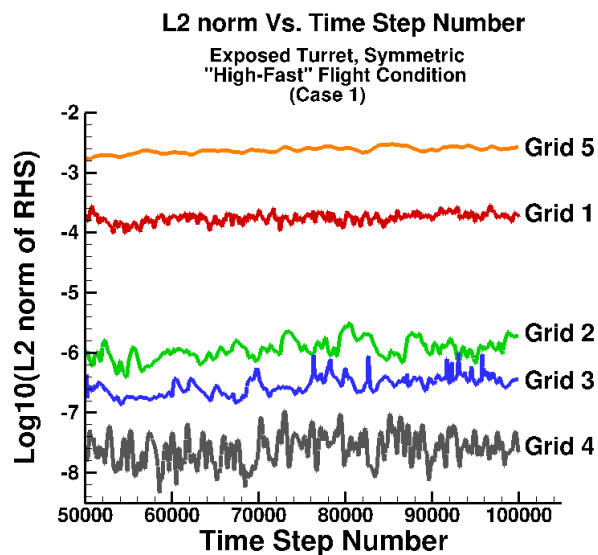
Figure 4.48:   L2 residuals for Cases 1, 5, 9, and 17.

V. Conclusions

The computational investigation was performed using the NASA developed time-marching finite volume code OVERFLOW 2.2 to analyze the effect of boundary layer height on symmetrical and non-symmetrical turret geometries. Four main configurations of the turret geometries were evaluated, hemispherical and submerged with a flat window orientation of 0° and 45° azimuthal angle. The various simulations were performed at two flight conditions referred to as "low-slow" and "high-fast". The "low-slow" flight condition corresponds to Mach number of 0.45, Reynolds number of 157,697 per inch (1.892×10^6 per foot), and an altitude of 18,000 feet. The second flight condition, referred to as "high-fast", was at Mach number of 0.85, Reynolds number of 238,376 per inch (2.86×10^6 per foot), and an altitude of 25,000 feet. The parametric study was set up to analyze the effects of the boundary layer height creating a total of 24 cases that were evaluated, (Figure 4.1).

The flow solver was set to run a total of 100,000 iterations, the data analyzed was collected from 50,000 to 100,000 iterations at a non-dimensionalized by the freestream velocity time step of 0.006. The effects of aerodynamics lead to the abberration of the laser beam through two methods, aero-optical and aero-mechanical jitter. To obtain a good representation of the flow field, fluctuations and mean quantities of the solutions were examined. To capture the effects of aero-mechanical jitter induced by the aerodynamics, fluctuations on the surface, force and moments, frequency analysis, and examination of flow features was conducted. The aero-optics induced by the various flow conditions were compared through the use of density fluctuations along the aperture center plane and through the examination of the flow features.

Qualitative analysis of the flow field revealed that the horseshoe vortex, a characteristic flow feature of that turret geometry, is not affected by the orientation of the aperture. The observation holds true for both the exposed and submerged turret geometry. Further investigation of the flowfield showed that a delay in separation occurs as the boundary layer height is increased. This trend was investigated through the use of surface streamlines with contours of velocity, iso-surfaces of vorticity magnitude,

and contours of Mach number. The results showed that an increase in boundary layer not only delays separation but can create a more unified shock formed around the turret, which is the case for the 100% boundary layer of the submerged geometry. It was also observed that due to the aperture location, the submerged turret geometry created a higher interaction between the horseshoe vortex and the laser beam. The study of flow features led to some further trends which showed that the flat window aperture creates discontinous shear layers which created a more turbulent wake. Using density gradients, Mach number, and iso-surfaces of vorticity magnitude showed that an increase in boundary layer height reduces the magnitude of the fluctuations on the turret surface and in the path of the beam. The increase in boundary layer height also creates a decrease in turbulence of the wake resulting in less aero-mechanical jitter induced on the geometry. From the flow features the results indicated that the submerged turret case had a more turbulent wake, observed through the pressure fluctuations than the exposed turret geometry. Further investigation led to the conclusion that the submerged turret geometry allows the shear layer formed over the turret top half to interact with the flat plate in the wake.

One of several capabilities integrated into OVERFLOW is to compute forces and moments on a body. The analysis employed through the study of forces and moments showed that a reduction in drag was observed for an increase in boundary layer for all simulations. The oscillations present in the drag coefficient were higher for the submerged case of the "high-fast" flight condition and lower for the submerged case of the "low-slow" flight condition. The y-force ("side force") computations over the turret body remained constant as the boundary layers were increased but the trend of the oscillation in side force recorded significantly higher values for the exposed geometry at the "high-fast" flight condition and higher for the exposed turret geometry at the "low-slow" flight condition. The results of the forces and moment calculations verify that due to the shorter distance between the shear layer and the flat plate, the fluid interacts in the wake by trying to reattach.

The aberration of the laser is affect by the variations in index of refraction in the fluid as the laser beam propagates. To investigate the density fluctuation along the beam's path, the centerline of the beam was used to compare the density fluctuations between the simulations. The results revealed that an increase in boundary layer reduces the density fluctuation for all simulations but the density fluctuation slightly increases with distance away from the aperture for the "high-fast" flight condition and reduces with distance for the "low-slow" results.

5.1 Future Work

The results and conclusion provide an insight into the aberration of the laser beam induced by the fluid at various flight conditions. To further expand the study and investigate the beam's performance, the optical path difference (OPD) should be computed and analyzed for each of the simulations conducted. By computing the optics on the laser, additional information about the beam's performance would be acquired rather than using the flow field quantities to predict the beam's quality. To study the aero-mechanical jitter induced on the beam, a finite element model is necessary to examine the effects of the pressure fluctuations on the surface and the vibrations it creates on the geometry.

Integrating the turret geometry on a full scale aircraft would provide additional information as to how the flow field about the turret interacts with the components of the aircraft. The integration of a sniper pod, used for targeting, next to the turret could potentially change the beam's performance and needs to be evaluated.

One of the issues to be investigated in the near future is to determine if the turbulence model switching between the RANS and LES computation leads to the reduction of forces and moments at higher boundary layer heights. The transition between the RANS and LES model could potentially create discrepencies in the values observed in the fluctuations.

Bibliography

1. Gordeyev, S. and Jumper, E., "Fluid Dynamics and Aero-Optics of Turrets," *Progress in Aerospace Sciences*, Vol. 46, 2010, pp. 388–400.

2. Horkovich, J., "Directed Energy Weapons: Promise Reality," AIAA Paper 2006-3753, Raytheon Missle Systems, June 2006.

3. Vukasinovic, B., Glezer, A., Gordeyev, S., Jumper, E., and Kibens, V., "Hybrid Control of a Turret Wake, Part I: Aerodynamic Effects," AIAA Paper 2010-86, Georgia Institute of Technology, January 2010.

4. Sutton, G. W., "Aero-Optical Foundations and Applications," *AIAA Journal*, Vol. 23, No. 10, 1985, pp. 1525–1537.

5. Gilbert, J. and Otten, L. J., *Aero-Optical Phenomena*, AIAA, 1982.

6. Snyder, C. H., Franke, M. E., and Masquelier, M. L., "Wind-Tunnel Tests of an Aircraft Turret Model," *Journal of Aircraft*, Vol. 37, No. 3, 2000, pp. 368–376.

7. Purhoit, S. C., Shang, J. S., and Hankey, W. L., "Effect of Suction on the Wake Structure of a Three-Dimensional Turret," AIAA Paper 1983-1738, USAF, July 1983.

8. Morgan, P. and Visbal, M., "Numerical Simulations Investigating Control of Flow Over a Turret," AIAA Paper 2009-574, Air Vehicles Directorate, WPAFB, January 2009.

9. Coulombe, S., "The Airborne Laser; Pie in the Sky or Vision of the Future Theater Missile Defense," *Aerospace Power Journal*, 1994.

10. Weik, M. H., *Fiber Optics Standard Dictionary*, Kluwer Academic Publishers, Prezzo, 1997.

11. Gordeyev, S., Cress, J., and Jumper, E., "Aero-Optical Properties of Subsonic, Turbulent Boundary Layers," *Journal of Fluid Mechanics*, Vol. Under Consideration for Journal.

12. Gladstone, J. and Dale, T., "Researches on the refraction, dispersion, and sensitiveness of liquids," *Philosophical Transaction of The Royal Society of London*, Vol. 153, 1863, pp. 317–343.

13. Merzkirch, W., *Flow Visualization*, Academic Press, 1987.

14. Tatarski, V., *Wave Propagation in Turbulent Medium*, McGraw-Hill, New York, 1961.

15. Liepmann, H. W., "Deflection and Diffusion of a Light Ray Passing Through a Boundary Layer," *Douglas Aircraft Company*.

16. Stine, H. A. and Winovich, W., "Light Diffusion Through High-Speed Turbulent Boundary Layers," AIAA Paper, Research Memorandum, May 1956.

17. Sutton, G. W., "Effects of Turbulent Fluctuations in an Optically Active Fluid Medium," AIAA Paper 1968-683, June 1968.

18. Gordeyev, S., Cress, J., and Jumper, E., "Aero-Optical Properties of Subsonic, Turbulent Boundary Layers," *Journal of Fluid Mechanics*, Vol. Under Consideration for Journal.

19. Smith, W., *Modern Optical Engineering: The Design of Optical Systems, Chap. 3*, Mcgraw-Hill, 1990.

20. Gordeyev, S. and Jumper, E., "Fluid Dynamics and Aero-Optics Enviornment Around Turrets," AIAA Paper 2009-4224, University of Notre Dame, 2009.

21. Manhart, M., "Vortex Shedding from a Hemisphere in a Turbulent Boundary Layer," *Theoretical Computational Fluid Dynamics*, Vol. 12, No. 1, 1998, pp. 1–28.

22. Toy, N., Moss, W. D., and Savory, E., "Wind tunnel studies on a dome in a turbulent boundary layer," *J. of Wind Engineering and Industrial Aerodynamics*, Vol. 11, No. 1-3, 1983, pp. 201–212.

23. Savory, E. and Toy, N., "The Flow Regime in the Turbulent Near Wake of a Hemisphere," *Experimental Fluid Dynamics*, Vol. 4, 1986, pp. 181–188.

24. Tavakol, M. M., Yaghoubi, M., and Masoudi Motlagh, M., "Air Flow Aerodynamic on a Wall-Mounted Hemisphere for Various Turbulent Boundary Layers," *Experimental Thermal and Fluid Science*, Vol. 34, No. 5, 2010, pp. 538–553.

25. Savory, E. and Toy, N., "Hemispheres and Hemisphere-Cylinders in Turbulent Boundary Layers," *Journal of Wind Engineering and Industrial Aerodynamics*, Vol. 23, 1986, pp. 345–364.

26. Savory, E. and Toy, N., "The Separated Shear Layers Associated with Hemispherical Bodies in Turbulent Boundary Layers," *Journal of Wind Engineering and Industrial Aerodynamics*, Vol. 28, No. 1-3, 1988, pp. 291–300.

27. Smits, A. and Dussauge, J.-P., *Turbulent Shear Layers in Supersonic Flow*, Springer, New York, 2006.

28. Vukasinovic, B., Glerzer, A., Gordeyev, S., Jumper, E., and Kibens, V., "Active Control and Optical Diagonostics of the Flow Over a Hemispherical Turret," AIAA Paper 2008-0598, 2008.

29. Buning, P. and Nichols, R., "User's Manual for OVERFLOW 2.1," *NASA Tech. Manual*, August 2008.

30. Thomspon, J., Soni, B., and Weatherill, N., *Handbook of Grid Generation*, CRC Press LLC, 1999.

31. Kravchenko, A. and Moin, P., "Numerical Studies of Flow Over a Circular Cylinder at $Re_D = 3900$," *Physics of Fluids*, Vol. 12, No. 2, 2000, pp. 403–417.

32. Sherer, S. and Visbal, M., "Multi-Resolution Implicit Large Eddy Simulations Using a High-Order Overset-Grid Approach," *International Journal for Numerical Methods in Fluids*, Vol. 55, No. 2, 2000, pp. 455–482.

33. Shim, Y. M., Sharma, R. N., and Richards, P. J., "Numerical Study of the Flow Over a Circular Cylinder in the Near Wake at Reynolds Number 3900," AIAA Paper 2009-4160, June 2009.

34. Kim, S.-E., "Large Eddy Simulation of Turbulent Flow Past a Circular Cylinder in Subcritical Regime," AIAA Paper 2006-1418, 2006.

35. Parnaudeau, P., Carlier, J., Heitz, D., and Lamballais, E., "Experimental and Numerical Studies of the Flow Over a Circular Cylinder at Reynolds number 3900," *Physics of Fluids*, Vol. 20, No. 8, 2008.

36. Jelic, R., Sherer, S., and Greendyke, R., "Computation of Aerodynamics Flows over Bluff Bodies Using an Overset-Grid Approach," AIAA Paper 2011-1234, Air Vehicles Directorate, WPAFB, January 2011.

37. Morgan, P. and Visbal, M., "Hybrid RANS/LES Simulations for Flow Around Two Turret Configurations," AIAA Paper 2008-550, 2008.

38. Menter, F. and Kuntz, M., "Adaptation of Eddy-Viscosity Turbulence Models to Unsteady Separated Flow Behind Vehicles," *Symposium*.

39. White, F., *Viscous Fluid Flow*, McGraw-Hill, 2006.

40. Baker, C., "The Laminar Horseshoe Vortex," *Journal of Fluid Mechanics*, Vol. 95, No. 2, 1979, pp. 347–367.

41. Eckerle, W. and Langston, L., "Horseshoe Vortex Formation Around a Cylinder," *Journal of Turbomachinery*, Vol. 109, No. 2, 1987.

42. Visbal, M., "The Laminar Horseshoe Vortex System Formed at a Cylinder/Plate Juncture," AIAA Paper 1991-1826, 1991.

REPORT DOCUMENTATION PAGE

1. REPORT DATE (DD–MM–YYYY)	2. REPORT TYPE	3. DATES COVERED (From — To)
16-06-2011	Master's Thesis	October 2009 – June 2011

4. TITLE AND SUBTITLE	5a. CONTRACT NUMBER
Study of Varying Boundary Layer Height on Turret Flow Structures	
	5b. GRANT NUMBER
	5c. PROGRAM ELEMENT NUMBER

6. AUTHOR(S)	5d. PROJECT NUMBER
Renato Jelic	
	5e. TASK NUMBER
	5f. WORK UNIT NUMBER

7. PERFORMING ORGANIZATION NAME(S) AND ADDRESS(ES)	8. PERFORMING ORGANIZATION REPORT NUMBER: AFIT/GAE/ENY/11-J01 AFIT/ENY
Air Force Institute of Technology Graduate School of Engineering and Management 2950 Hobson Way WPAFB OH 45433-7765	

9. SPONSORING / MONITORING AGENCY NAME(S) AND ADDRESS(ES)	10. SPONSOR/MONITOR'S ACRONYM(S) AFRL/RBAT
Scott E. Sherer Air Vehicles Directorate 2130 Eighth Street Wright-Patterson AFB, OH 45433-7542 Scott.Sherer@wpafb.af.mil (937) 904-4046	
	11. SPONSOR/MONITOR'S REPORT NUMBER(S)

12. DISTRIBUTION / AVAILABILITY STATEMENT
APPROVED FOR PUBLIC RELEASE; DISTRIBUTION UNLIMITED

13. SUPPLEMENTARY NOTES
This material is declared a work of the U.S. Government and is not subject to copyright protection in the United States.

14. ABSTRACT

The Air Force Institute of Technology and the Air Force Research Labs are investigating flows over turrets which are commonly encountered in directed energy integrations with air vehicles. In this work, the computational study was performed using the NASA developed time-marching finite volume code OVERFLOW 2.2 to analyze the effect of boundary layer height on symmetrical and non-symmetrical turret geometries. The effects of aerodynamics yield to the aberration of the laser beam through two methods, aero-optical and aero-mechanical jitter. The analysis of the flow features, pressure fluctuations, density fluctuations, and forces and moments on the various geometries was conducted to predict the impact on the beam quality at low subsonic and transonic speeds. The two flight conditions referred to as "low-slow" and "high-fast" where the "low-slow" flight condition was computed with Mach number of 0.45, Reynolds number of 157,697 per inch (1.892×10^6 per foot), and an altitude of 18,000 feet. The second flight condition referred to as "high-fast" was set to Mach number of 0.85, Reynolds number of 238,376 per inch (2.86×10^6 per foot), and an altitude of 25,000 feet. The parametric study set up led to 24 cases for comparison of various boundary layer heights between the submerged and exposed turret geometries. The study of flow features indicated that an increase in boundary layer delays the separation and yields to a reduction in the aero-mechanical and aero-optical jitter. For the study of aero-mechanical jitter the pressure fluctuations on the surface of the turret and the flat plate were analyzed to show that an increase in boundary layer reduces the pressure fluctuations in the wake of the geometry. Additionally, the forces and moments about the geometry were evaluated which showed that the submerged turret geometry has a higher induced fluctuation in the forces and moments than the hemispherical geometry. For the study of aero-optical jitter induced on the laser beam, density fluctuations along the centerline of the aperture were examined to show the effects of the boundary layer heights both quantitatively and qualitatively.

15. SUBJECT TERMS
Computational Fluid Dynamics

16. SECURITY CLASSIFICATION OF:			17. LIMITATION OF ABSTRACT	18. NUMBER OF PAGES	19a. NAME OF RESPONSIBLE PERSON Dr. Robert Greendyke, P.E.
a. REPORT	b. ABSTRACT	c. THIS PAGE	UU	118	19b. TELEPHONE NUMBER (Include Area Code) (937)255-3636, ext 4567
U	U	U			